On non-equilibrium dynamics in low-dimensional strongly correlated quantum systems

About the cover: Photograph of the single-lane road between Carbost and Glenbrittle on the Isle of Skye, Scotland, where the author, his father and his brother went mountainbiking for a few days in May 2018. On this usually busy single-lane road, cars tend to spontaneously form groups in order to travel from one passing place to the next. This "collective" behavior, in that cars no longer travel individually, reminded the author of the physics in the one-dimensional quantum systems, that he had worked on at the time. The signs marking the passing places also bear a resemblance with the quantum impurity models, that the author has studied to gain a deeper insight into the effects of additional intrinsic degrees of freedom in quantum impurity systems.

On non-equilibrium dynamics in low-dimensional strongly correlated quantum systems

Over niet-evenwichtsdynamiek in laag-dimensionale sterk gecorreleerde kwantumsystemen

(met een samenvatting in het Nederlands)

Proefschrift

ter verkrijging van de graad van doctor aan de Universiteit Utrecht op gezag van de rector magnificus, prof. dr. H.R.B.M. Kummeling, ingevolge het besluit van het college voor promoties in het openbaar te verdedigen op woensdag 12 juni 2019 des middags te 2.30 uur

door

Benedikt Matthias Schönauer

geboren op 12 september 1988 te Karlsruhe, Duitsland

Promotor: Prof. dr. ir. H.T.C. Stoof
Copromotor: Dr. D. Schuricht

Dedicated to my mother Andrea,

I wish she could have read this thesis.

Contents

Chapter 1

Introduction

Surely one of the first questions in any given talk on the theory of one-dimensional systems, that is asked by both un-initiated physicists and laymen alike, boils down to: *How is it reasonable to think of a material as strictly one-dimensional, when we live in a three-dimensional world and the constituent atoms of the material have a finite size as well?* We would thus like to address this question first, before then discussing the many reasons for studying one-dimensional model systems and the rich history of the field.

Probably the simplest quantum mechanical model system known to (hopefully) every physicist, is that of the particle in a box. A single particle, say an electron, that is confined to a boxed volume, is described by a wave function $|\psi\rangle$, which is a solution of the Schrödinger equation

$$E|\psi\rangle = \left(-\frac{\hbar^2\partial_x^2}{2m} - \frac{\hbar^2\partial_y^2}{2m} - \frac{\hbar^2\partial_z^2}{2m} + V(x,y,z) \right) |\psi\rangle \, , \qquad (1.1)$$

where $V(x,y,z)$ represents a potential that vanishes inside the box and becomes infinitely large ($V = +\infty$) outside the box. The solutions of this Schrödinger equation are simple sine and cosine functions of the argument $k_\alpha \alpha$ with $\alpha \in \{x,y,z\}$. The wave numbers $k_\alpha = n(\pi/L_\alpha)$ count the number of complete waves n that fit into each extent L_α of the box. The three differential equations in (1.1) are not coupled and we can therefore examine the solutions in each direction α separately. The energy associated with the wave function of wave number k_α is

$$E_n = \frac{\hbar^2 k_\alpha^2}{2m} = \frac{n^2 \hbar^2 \pi^2}{2m L_\alpha^2} \, , \qquad (1.2)$$

where we highlight that E_n is inverse proportional to the length L_α^2. We show the wave functions $|\psi_n\rangle$, that correspond to the four lowest energies E_n, in figure 1.1. It is easy to see that the energy gaps between the states grow quickly as n increases, namely as n^2. However, here we are only interested in the energy gap ΔE between
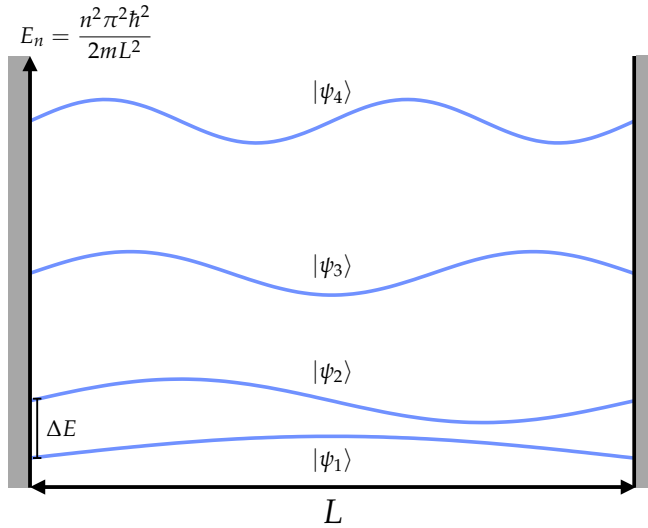
Figure 1.1: *Depiction of the low energy solutions $|\psi_n\rangle$ to the Schrödinger equation describing a particle in a one-dimensional infinite potential well. The position of the wave functions in z-direction indicates their corresponding energy E_n.*

the ground state $|\psi_1\rangle$ and the state directly above it, $|\psi_2\rangle$. If we imagine our box to be the size of an atom, which is typically $L_A = 1$ Angstrom $= 10^{-10}$ m, then this energy gap amounts to

$$\Delta E = \frac{3\hbar^2 \pi^2}{2m_e L_A^2} \simeq 100 \, \text{eV} , \tag{1.3}$$

where m_e denotes the mass of the electron. By contrast, the thermal energy at room temperature is $E_{\text{th}} = k_B T \simeq 2.7 \times 10^{-2}$ eV. So, unless randomly hit by an x-ray photon, an electron will not transition from the ground state to an excited state - certainly not for the duration of a typical experiment - and will thus remain completely unaware of these states. What constitutes a dimension, namely a degree of freedom, simply does not exist for that particular electron. In a chain of atoms, the only degree of freedom then left to the electron, is the "choice" between the quantum states corresponding to the different wave numbers k_x along the direction of the chain. For all intents and purposes, the world of the electron is one-dimensional.

So now that we have established that it is reasonable to treat a system as one-dimensional in certain circumstances, let us consider a few materials where such circumstances are realized.
A straightforward example would be artificial ultra-thin *quantum wires*, in which the electrons become confined to a region of just a few nanometers in the directions orthogonal to the wire. These regions are created in a typical hetero-structure, where

a layer of GaAs is sandwiched between two thick layers of AlGaAs. Such a hetero structure is host to a two-dimensional electron gas (2DEG) inside the GaAs layer. By framing the structure with a perpendicular layer of AlGaAs, the electron gas becomes stricly confined to the GaAs layer in every direction. A tungsten gate that is placed on top of the hetero structure subsequently brings about a potential that traps the electrons in a thin region at the edges of the GaAs layer. Using this approach, Yacoby et al. [1, 2] were able to create a quantum wire with dimensions $10\,\mu\mathrm{m} \times 25\,\mathrm{nm} \times 25\,\mathrm{nm}$ and level separation $\Delta E > 20\,\mathrm{meV}$. Measurements of the conductance in these systems reveals the characteristic features of a one-dimensional system [3].

A second example of one-dimensional physics emerging in a two-dimensional system, is in fractional quantum Hall systems, where the excitations at the edge are described by one-dimensional theories [4].

A class of superconducting organic crystals, known as Bechgaard salts, is also adequately described by a one-dimensional theory, due to their strong anisotropy [5].

Certainly the material with the most potential applications in our list of one-dimensional materials are carbon nanotubes [6]. Due to their immense strength and stiffness, they are used to increase the structural rigidity of objects ranging from the tips of atomic force microscopes to airplanes. Some even see them as the material that could one day realize a space elevator. Most important for our sake though, is the fact that these nanotubes can have diameters of less than $1\,\mathrm{nm}$, while at the same time macroscopic lengths of up to half a meter have been achieved [7], making them a somewhat ideal one-dimensional system. Scanning tunneling microscopy of metallic carbon nanotubes indeed reveals the power law tunneling density of states that is so characteristic for one-dimensional systems [8].

By themselves, these materials warrant a theoretical interest in one-dimensional systems, yet the driving force for theoretical efforts in the field lies elsewhere.

When in 1995 a group of experimentalists achieved the first Bose-Einstein condensate (BEC) using a gas of Rubidium atoms at a temperature of $T = 1.7 \times 10^{-7}\,\mathrm{K}$ [9], it showcased the enormous potential of such ultracold atomic gases to realize new states of matter.

Three years later, several theorists suggested the use of interfering laser beams to construct an optical lattice in which to place a gas of ultracold atoms. The ac Stark effect arising from the alternating electric field of the laser light induces a dipole moment in the atoms and the interaction between said dipole moment and the field confines the atoms to the valleys of the optical lattice. The atoms still retain the ability to tunnel between neighboring valleys of the lattice though. By extending the depth of the valley, the wave functions of the atoms become more localized, resulting in an increased repulsive interaction between atoms in the same valley. The ratio between interaction strength and tunneling amplitude U/J is hence easily controlled through the parameters of the lasers. Building on an idea by Feynman [10], Jaksch et al. [11, 12] proposed this experimental setup for a simulation of the quantum phase transition between a BEC and the Mott-insulating phase of the two-dimensional Bose-Hubbard model, characterized by the parameters U and J.

This precise experiment was performed in 2002 by Greiner et al. [13], where they were able to clearly identify said phase transition. The experiment marks the first application of ultracold atomic gases in optical lattices for the simulation of the behavior of strongly correlated many-body quantum systems, for which a rigorous theoretical study is not possible.

Since then, the experiments have become more and more refined. Every parameter of the simulated models can be precisely tuned, and extended to values that cannot be reached in regular materials, for example through the use of Feshbach resonances [14, 15]. Fermionic model systems have since also been realized, most notably Fermi-Hubbard models, of which the two-dimensional version is of particular importance for the study of high-T_c superconductivity, and the one-dimensional one serves as an important benchmark, as we shall see later [16–21]. In the meantime, quantum gas microscopes now allow the manipulation and tracking of invidual atoms, which offers the opportunity to create custom quantum states and to observe their time evolution in detail [22, 23]. Another exceptional feature of ultracold atomic gas experiments is their strong isolation from the environment, which makes the simulation of closed quantum systems possible. Most important - in the context of this thesis - is the ability of these experiments to rapidly adjust the parameters of the simulated systems, usually on time scales smaller than the typical time scales of the model systems. This allows for the implementation of sudden and time-dependent quantum quench protocols, the non-equilibrium dynamics in response to both of which we discuss in the thesis on hand.

Even though originally motivated by theoretical work, the power to simulate strongly correlated many-body models in a plethora of conditions, that is offered by these ultracold atom experiments, now stimulates theorists to look into previously unexplored aspects of such models, particularly their non-equilibrium behavior. A good example of this stimulus is the famous quantum Newton's cradle experiment by Kinoshita et al. [24] (see Fig. 1.2). In it, two clouds of Rubidium atoms in a one-dimensional harmonic trapping potential were shown not to relax to a thermal equilibrium. This result sparked a large body of theoretical work on the equilibration and thermalization behavior of one-dimensional systems at or close to integrability [25, 26].

The current interest in one-dimensional many-body systems may be incentivized by these exciting new experimental possibilities, but the fascination of theorists with one-dimensional systems predates the experiments by several decades.

The reasons for this fascination are manifold: The dominant role of interactions and quantum fluctuations in these systems brings about a host of new and exotic phenomena. Likewise, the Fermi liquid picture, in which quasi-particle excitations of an interacting system are essentially free electrons with mass corrections, becomes inadequate and needs to be replaced with the Luttinger liquid picture. The physics of one-dimensional systems is thus arguably not less interesting than the physics of their higher-dimensional counterparts.

And while many-body problems are inherently difficult to study in 1D, 2D, and 3D,-thus the need for quantum simulators - the restrictions, that arise from operating in a single dimension, give rise to several powerful tools that allow us to do just that.
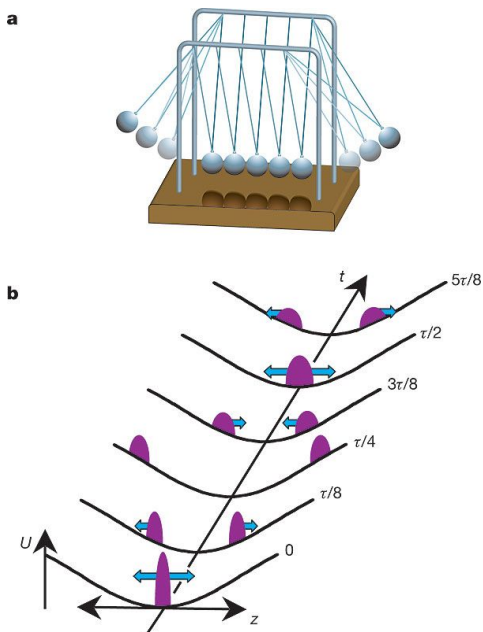
Figure 1.2: *Depiction of the classical (a) and the quantum (b) Newton's cradle. Reprinted from [24] with permission from Springer Nature.*

The first of these dates back to 1931, when Hans Bethe, while on a train ride to Rome, conceived of the Bethe ansatz, with which he was able to find the exact eigenvalues and eigenstates of the Heisenberg spin chain [27, 28]. Later, it was realized that the Heisenberg chain belongs to a class of models, known as integrable models, for which the many-body scattering matrix satisfies the Yang-Baxter equation [29]. Based on this insight, additional Bethe ansatz approaches were developed, which grant access to the exact eigenvalue spectrum of integrable systems [30].

Arguably the most important of these exactly solvable models is the Fermi-Hubbard chain [31]. It is straightforward to generate with ultracold atoms and serves as an ideal benchmark for experimental and theoretical work alike.

Better yet, our available tools are not limited to integrable models. In 1950, Shinichiro Tomonoga devised a model, that described the low-energy excitation of one-dimensional interacting fermionic theories in terms of free bosons [32]. Due to subsequent contributions by Joaquin Luttinger [33], this model is now known as Tomonaga-Luttinger model. The bosonization of fermionic theories then culminated in the 1980s, when Duncan Haldane put forward a universal description of one-dimensional fermionic quantum liquids as bosonic density fluctuations with renormalized parameters [34–36]. This Luttinger liquid description captures the exotic physical phenomena of 1D materials, such as spin-charge separation [17], where the electrons in the material separate into two or three independent particles, one of which carries the electron's charge, one its spin and one its orbital degree of freedom.

The Luttinger liquid theory is also an example of a conformal field theory (CFT). Several other important physical systems can also be described by CFTs and are thus amenable to the powerful toolset that exists for such theories in one spatial dimension [37, 38].

There are furthermore multiple numerical means by which to tackle one-dimensional many-body problems. Following the introduction of the Numerical Renormalization Group by Wilson [39] and the Density Matrix Renormalization Group by White [40], a whole slew of algorithms was developed that allow for the calculation of eigenstates, operator expectation values and correlation functions, often to machine precision, and last but not least the simulation of the time evolution of quantum states.

By now, we have hopefully convinced the reader that the new possibilities for experimental verification and the copious computational tools at hand, are ample reason to study previously unexplored facettes of one-dimensional many-body systems.

The particular facette studied in the work at hand, is the non-equilibrium dynamics, which in our case are generated by sudden and time-dependent quantum quenches. Such non-equilibrium dynamics are a particularly difficult problem, because the time evolution of the initial many-body quantum state, which is governed by the post-quench Hamiltonian, is highly non-trivial. On top of that, applying an operator to this many-body quantum state in order to calculate its expectation values, typically creates an intricate set of excitations. [41, 42]

Throughout the thesis, we furthermore contrast the results that we have obtained using exact numerical methods for two microscopic models, namely the Heisenberg and Fermi-Hubbard chains, with results derived from the Luttinger liquid theory, which, in equilibrium, describes the universal behavior of the two models.

In the second part of the thesis, we reduce the dimensionality even further and employ complementary numerical and analytical tools to examine the unusual non-equilibrium behavior of a ring-shaped quantum impurity hosting interacting spinless fermions.

Outline

The thesis is structured as follows:

- **Chapter 2** gives a brief overview of serveral numerical methods that we have employed throughout our work. It also introduces the XXZ Heisenberg chain and subsequently the Tomonaga-Luttinger model as its low-energy description.

- In **Chapter 3**, we calculate the local density of states (LDOS) of the Fermi-Hubbard chain in the Mott-insulating phase. We then examine the Fourier transform of the LDOS for features corresponding to spin-charge separation.

- **Chapter 4** is devoted to the study of time-dependent interaction quenches in the XXZ Heisenberg chain. We analyze the effect of the finite quench duration

on the light cone of correlation spreading and scrutinize the applicability of Luttinger liquid theory for systems out of equilibrium.

- In **Chapter 5**, we investigate the extended lifetimes of transient oscillations of the local currents in an interacting ring-shaped quantum impurity. We probe the system in a variety of different limits to gain an understanding of the mechanisms that prevent the local currents from relaxing to the non-equilibrium steady state.

The thesis concludes with a summary of our results in English and Dutch and a discussion of open questions and future work.

Notation   Unless otherwise specified, we employ natural units, in which $\hbar = k_B = c = 1$. As notation for the elementary charge we use e and we use e for the base of the natural logarithm.

List of Publications

The content of the subsequent chapters is linked to the following publications:

- Chapter 3 is based on
  B. Schoenauer, P. Schmitteckert, and D. Schuricht, *Observation of spin-charge separation and boundary bound states via the local density of states.* Phys. Rev. B, **95**, 205103, (2017).
  BS performed the calculations, created the plots and participated in the writing of the publication.

- Chapter 4 is based on
  B. Schoenauer and D. Schuricht, *Finite-time quantum quenches in the XXZ Heisenberg chain*, submitted to PRB, arXiv:1905.02678, (2019).
  BS performed the calculations, created the plots and participated in the writing of the publication.

- Chapter 5 is based on
  B. M. Schoenauer, N. M. Gergs, P. Schmitteckert, F. Evers, and D. Schuricht, *Long-lived circulating currents in strongly correlated nanorings*, submitted to Physical Review Letters, arXiv:1903.01721, (2019).
  BMS performed the calculations, created the plots and participated in the writing of the publication.

- Chapter 6 is based on the supplementary material of
  B. M. Schoenauer, N. M. Gergs, P. Schmitteckert, F. Evers, and D. Schuricht, *Long-lived circulating currents in strongly correlated nanorings*, submitted to Physical Review Letters, arXiv:1903.01721, (2019).

Chapter 2

2 Overview of Methods

In this chapter, we give a brief introduction to a selection of methods and models that we have used in our work or that we have compared our results to on more than one occasion[1]. It is targeted at the reader who is not yet familiar with these topics and not eager to consult a separate dedicated book in order to understand the terminology or the origin of models, that have been used in the subsequent chapters. Readers with a working knowledge of the topics should feel free to skip this chapter. In Sec. 2.1, we present two widely used algorithms for the diagonalization of sparse matrices. Sec. 2.2 introduces the singular value decomposition, a powerful tool in matrix approximation. In Sec. 2.3, we give a short introduction to the Density Matrix Renormalization Group. We discuss the truncation scheme and the infinite and finite lattice algorithms. We further explain the approach that we have used for the time evolution of quantum states. The last section gives a motivation for the use of the Tomonaga Luttinger model as a low-energy description of the XXZ Heisenberg spin chain in equilibrium.

2.1 Exact Diagonalization of Sparse Matrices

Dealing with strongly correlated systems on a lattice means, numerically speaking, dealing with extremely large Hilbert spaces and in turn extremely large matrices. Non-interacting theories can usually be mapped onto effective single particle models, for which the Hilbert space grows linearly as a function of the lattice size. For the study of strongly correlated systems, on the other hand, we need to take into account the full many-body Hilbert space and this vector space grows exponentially with the lattice size. As an example, the Hilbert space $\mathcal{H}$ of a chain of interacting, spinless fermions amounts to

$$\mathcal{H} = \mathcal{H}_1 \otimes \mathcal{H}_2 \otimes \cdots \otimes \mathcal{H}_L \,, \tag{2.1}$$

---

[1]Some of the material presented in this chapter has previously been part of: Benedikt Matthias Schönauer, *Nonlinear quantum transport in nanoscopic interacting ring structures*, Master's thesis KIT, (2015)

where $\mathcal{H}_i$ are the local Hilbert spaces, which each comprise the basis vectors $|0\rangle_i$ and $|1\rangle_i$. As such, it has dimension $D_{\mathcal{H}} = 2^L$, where L is the length of the chain in terms of lattice sites. The situation is even worse for systems with a larger local basis, such as fermions with spin. Numerical methods such as the Numerical Renormalization Group (NRG) and Density Matrix Renormalization Group (DMRG)[2] make a study of these systems feasible by constructing the Hilbert space iteratively and projecting onto subspaces most likely to contain a set of target states in the process. Nevertheless, these methods still leave us with matrices usually too large to be diagonalized in their entirety. In most cases, we are only interested in the smallest eigenstates of a given Hamiltonian and thus require a method that can obtain these states for large matrices. In the following, we will discuss two particular algorithms employed in our work, that retrieve the extremal eigenvalues of a (hermitian) matrix.

2.1.1 Krylov Subspaces

In most cases, our aim will be to find the ground state of a Hamiltonian H. This is equivalent to finding a vector v such that the Rayleigh quotient

$$r(v) = \frac{\langle v|A|v\rangle}{\langle v|v\rangle} \qquad |v\rangle \neq 0, \tag{2.2}$$

assumes its minimum value $\lambda_{\min}$, where A is the matrix representation of the Hamiltonian H. We now iteratively introduce a sequence of orthonormal vectors q_n and the corresponding projection matrix $Q_n = [q_1, \ldots, q_n]$. It is obvious that

$$m_n = \min \frac{\langle v|Q_n^T A Q_n|v\rangle}{\langle v|Q_n^T Q_n|v\rangle} \qquad |v\rangle \neq 0, \tag{2.3}$$

will eventually converge to $\lambda_{\min}$ for $n \to \dim(A)$. The objective is to find q_n such that this convergence becomes rapid and we only need to diagonalize a matrix $T = Q_n^T A Q_n$ with $\dim(T) \ll \dim(A)$. For this, we consider the gradient of the Rayleigh quotient which reads

$$\nabla r(v) = \left(\frac{2}{\langle v|v\rangle}\right)\left(A|v\rangle - r(v)|v\rangle\right). \tag{2.4}$$

Once, through diagonalization of $Q_n^T A Q_n$, we determine a vector v_n corresponding to m_n with $\nabla r(v_n) = 0$, then v_n is an eigenvector of A with eigenvalue $\lambda = m_n$. If $\nabla r(v_k) \neq 0$, then the vector pointing in the direction that results in the largest decrease of $r(v_n)$ is given by $-\nabla r(v_n)$. For example, if we pick an arbitrary vector $|q_1\rangle$, which is not already an eigenvector of A, then we know that $m_2 \leq m_1$ if

$$|q_2\rangle = \left(\frac{2}{\langle q_1|q_1\rangle}\right)\left(A|q_1\rangle - \frac{\langle q_1|A|q_1\rangle}{\langle q_1|q_1\rangle}|q_1\rangle\right). \tag{2.5}$$

---

[2]There are many related methods collectively referred to as Matrix Product State methods, for the subspaces that they project onto.

To ensure rapid convergence, it is thus instructive to add $|q_{n+1}\rangle = A|q_n\rangle$ in the next consecutive subspace, in which to diagonalize A. The problem of finding extremal eigenvalues therefore translates to constructing orthonormal bases in Krylov subspaces [67]. A Krylov subspace $\mathcal{K}_v^n(A)$ is defined by the matrix A and the starting vector v as

$$\mathcal{K}_v^n(A) = \text{span}\left\{v, Av, A^2 v, \ldots, A^{n-1} v\right\}. \tag{2.6}$$

One typically uses a random starting vector v to construct the Krylov subspace, but a good initial guess for the starting vector significantly increases the calculation speed. The advantage of Krylov subspace methods for eigenvalue problems is that they only involve matrix-vector products, which are computationally less costly than matrix-matrix products. For sparse matrices of known structure, this computational cost can be reduced even further through implicit matrix-vector products.

2.1.2 Lanczos Tridiagonalization

The Lanczos algorithm [68] is a simple, iterative method to generate extremal eigenvalues and corresponding eigenstates of sparse, hermitian matrices $A \in \mathbb{C}^{l \times l}$. The algorithm creates a sequence of Krylov subspaces, in which the original matrix A is related to a tridiagonal matrix T via a unitary similarity. The eigenvalues of this tridiagonal matrix T rapidly converge on the extremal eigenvalues of A, which includes the smallest eigenvalue, which in turn corresponds to the ground state [67, 69].

Lanczos tridiagonalization builds up a Krylov subspace $\mathcal{K}_v^n(A)$ via a recurring application of A to an initial vector v. A subsequent Gram-Schmidt orthonormalization scheme generates a basis of this subspace and produces the entries of the triadiagonal matrix T.

Algorithm (Lanczos)

(i) Starting with an arbitrary initial vector $v = |v_1\rangle$ and $\beta_1 = 0$, generate a new vector $|q_{n+1}\rangle$ from the current vector v_n by multiplying A with v_n. Subtract $\beta_n v_{n-1}$ from q_{n+1},

$$|q_{n+1}\rangle = A|v_n\rangle - \beta_n|v_{n-1}\rangle, \tag{2.7}$$

to ensure q_{n+1} is orthogonal to all vectors v_m with $m < n$.

(ii) Determine α_n as the matrix element of A for v_n as

$$\alpha_n = \langle q_{n+1}|v_n\rangle = \langle v_n|A|v_n\rangle. \tag{2.8}$$

The diagonal element $T_{n,n}$ of the tridiagonal matrix T, approximating A, is given by α_n.

(iii) Calculate q'_{n+1} , the part of q_{n+1} orthogonal to v_n, as

$$|q'_{n+1}\rangle = |q_{n+1}\rangle - \alpha_n |v_n\rangle.$$ (2.9)

(iv) Calculate the norm of q'_{n+1}

$$\beta_{n+1} = \sqrt{\langle q'_{n+1} | q'_{n+1}\rangle}.$$ (2.10)

The norm β_{n+1} will be the off-diagonal element $T_{n,n+1} = T_{n+1,n}$. Normalize q'_{n+1} and add it as the new orthonormal basis vector of the expanded Krylov subspace $\mathcal{K}_v^{n+1}(A)$ as

$$|v_{n+1}\rangle = \frac{|q'_{n+1}\rangle}{\beta_{n+1}}.$$ (2.11)

If β_{n+1} becomes smaller than a chosen cutoff, stop the algorithm at this point. Otherwise continue with (v).

(v) Increment the index $n = n+1$ and include $|v_n\rangle$ into the projection matrix $V_n = \{v_1, v_2, \ldots, v_n\}$. Then repeat the steps (i)-(iv).

As mentioned, the coefficients α_i and β_i form a tridiagonal matrix

$$T = \begin{pmatrix} \alpha_1 & \beta_2 & \cdots & \cdots & 0 \\ \beta_2 & \alpha_2 & \ddots & & \vdots \\ \vdots & \ddots & \ddots & \ddots & \vdots \\ \vdots & & \ddots & \alpha_{n-1} & \beta_n \\ 0 & \cdots & \cdots & \beta_n & \alpha_n \end{pmatrix}$$ (2.12)

where $\dim(T) \ll \dim(A)$. It can be efficiently diagonalized using algorithms for tridiagonal matrix diagonalization. The orthonormal projection matrix V_n relates T to A via

$$A \simeq V_n T V_n^\dagger.$$ (2.13)

In the original basis, the eigenvectors $|\tilde{\lambda}\rangle$ of T are hence given by

$$|\lambda\rangle = \sum_i |v_i\rangle \langle v_i | \tilde{\lambda}\rangle.$$ (2.14)

The Lanczos tridiagonalization is a fast and robust algorithm for the calculation of extremal eigenvalues and their respective eigenvectors even of large, sparse and hermitian matrices. Typically, fewer than 100 cycles are sufficient to calculate the smallest eigenvalue of a matrix up to almost machine precision.

Matrix functions   In addition to replicating the extremal spectrum of A, the tridiagonal matrix T, generated by Lanczos tridiagonalization, is also a very good approximation of A as a whole, albeit with much smaller dimensions. Lanczos tridiagonalization is therefore also a useful tool for the calculation of matrix functions via

$$f(A) \simeq V_n f(T) V_n^\dagger \,, \tag{2.15}$$

which results in a significant speed increase in the calculation of matrix functions. The matrix function that we will be most interested in calculating is the matrix exponential of the Hamiltonian, which is used for the time evolution of an initial quantum state after a quantum quench. This matrix exponential is well approximated by

$$e^{-iA\Delta t} \simeq V_n e^{-iT\Delta t} V_n^\dagger \,, \tag{2.16}$$

where the time step size Δt does not affect the quality of the approximation.

2.1.3 Davidson Eigenvalue Solver

The Davidson algorithm is an alternative method to obtain a target sector of the spectrum of a hermitian and diagonally dominant matrix A, where diagonally dominant means $A \approx D = \mathrm{diag}(A)$. The algorithm allows for the calculation of a particular eigenvalue and typically converges more quickly than the Lanczos algorithm. It is on the other hand computationally more costly than Lanczos, as it requires the calculation of matrix-matrix products. This also indicates that the Davidson algorithm does not technically construct a Krylov subspace.

Algorithm (Davidson)   For the calculation of the j-th eigenvalue of A, one starts with a suitably large subspace spanned by $i \geq j$ orthonormal basis vectors and the corresponding projection matrix

$$V_1 = \{v_1\} \,, \qquad V_i = \{v_1, \ldots, v_i\} \,. \tag{2.17}$$

(i) Project the matrix A onto the n-th subspace V_n to obtain a smaller matrix

$$\tilde{A}_n = V_n^T A V_n \,. \tag{2.18}$$

(ii) Solve the eigenvalue problem

$$\tilde{A}_n |\tilde{a}\rangle = \lambda |\tilde{a}\rangle \,, \tag{2.19}$$

and express the eigenvalues

$$|a\rangle = \sum_{i=1}^{n} |v_i\rangle \langle v_i | \tilde{a}\rangle \,, \tag{2.20}$$

in terms of the full original basis.

(iii) Calculate the residual vector

$$|r\rangle = (A - \lambda) |a\rangle, \tag{2.21}$$

and stop if $\|r\|_2 \leq c$, where c is a previously chosen cutoff. Approximate the matrix A with its diagonal part D to compute the correction vector $|\delta v_n\rangle$. The correction vector is the solution to

$$\left(D - \lambda \mathbb{1}\right) |\delta v_n\rangle = -|r\rangle. \tag{2.22}$$

(iv) Orthogonalize the correction vector against the current basis V_n via

$$|\delta v_n'\rangle = \left[\mathbb{1} - V_n V_n^T\right] |\delta v_n\rangle. \tag{2.23}$$

(v) Normalize $|\delta v_n'\rangle$ to obtain the new orthonormal basis vector

$$|v_{n+1}\rangle = \frac{|\delta v_n'\rangle}{\sqrt{\langle \delta v_n'|\delta v_n'\rangle}}. \tag{2.24}$$

(vi) Increment the index $n = n + 1$ and expand the basis $V_n = \{v_1, v_2, \ldots, v_{n-1}\}$ with the new basis vector $|v_n\rangle$. Continue by repeating steps (i)-(vi).

The Davidson eigenvalue solver does not suffer from the loss of orthogonality that plagues the Lanczos algorithm. Said loss of orthogonality can lead to artificial copies of converged eigenstates. The Davidson algorithm is therefore often preferred over the faster Lanczos algorithm for the computation of excited states [70].

2.2 Singular Value Decomposition

The fundamental ingredient of the density matrix renormalization group and matrix product state based methods in general is the singular value decomposition (SVD), which is sometimes also referred to as Schmidt-decomposition in the literature. Matrix decompositions are specific factorizations of a single matrix into a product of matrices. These matrices typically have shapes or properties particular to the matrix decomposition. In the LU-decomposition, for example, a matrix is factorized into the product of a lower triangular matrix L and an upper triangular matrix U. The SVD in turn factorizes a matrix into a product of one diagonal and two unitary matrices.

Theorem (Singular Value Decomposition)   For any matrix $A \in \mathbb{C}^{m \times n}$ with $m \geq n$, there exist unitary matrices $U \in \mathbb{C}^{m \times m}$ and $V \in \mathbb{C}^{n \times n}$ such that

$$A = U\Sigma V^\dagger = \begin{pmatrix} U_1 & U_2 \end{pmatrix} \begin{pmatrix} \Sigma_1 & 0 \\ 0 & \Sigma_2 \end{pmatrix} \begin{pmatrix} V_1^\dagger \\ V_2^\dagger \end{pmatrix}, \tag{2.25}$$

with

$$\Sigma_1 = \text{diag}\left(\sigma_1, \sigma_2, \dots, \sigma_r\right) \in \mathbb{R}^{r \times r}, \tag{2.26}$$

and

$$\Sigma_2 = \text{diag}\left(0, \dots, 0\right) \in \mathbb{R}^{(n-r) \times (n-r)}, \tag{2.27}$$

where $r \leq n$ is the rank of the matrix A. The diagonal elements of Σ_1 satisfy $\sigma_1 \geq \sigma_2 \geq \cdots \geq \sigma_r > 0$ and are referred to as singular values of A. The vectors $\mathbf{u}_i$ and $\mathbf{v}_j$ forming $U = (\mathbf{u}_1, \dots, \mathbf{u}_m)$ and $V = (\mathbf{v}_1, \dots, \mathbf{v}_n)$ are called the left and right singular vectors. For a selection of proofs of the theorem we refer the reader to [67, 69, 71, 72].

At this point, it is instructive to introduce the Frobenius norm as a measure of distance on the space of matrices. The Frobenius norm is defined as

$$\|A\|_F = \sqrt{\sum_{i=1}^{m} \sum_{j=1}^{n} \left|a_{ij}\right|^2} = \sqrt{\text{trace}\left(A^\dagger A\right)}, \tag{2.28}$$

analogous to the Euclidean norm $\|\mathbf{v}\|_2 = \sqrt{\sum_n |v_n|^2}$ for vector spaces. By employing the SVD one immediately finds that

$$A^\dagger A = V \Sigma U^\dagger U \Sigma V^\dagger = V \Sigma^2 V^\dagger, \tag{2.29}$$
$$A A^\dagger = U \Sigma V^\dagger V \Sigma U^\dagger = U \Sigma^2 U^\dagger. \tag{2.30}$$

The singular values of A are evidently the square roots of the eigenvalues of matrices $\rho_1 = A^\dagger A$ and $\rho_2 = A A^\dagger$ and the matrices U and V contain the corresponding eigenbasis. We can also use this result for the Frobenius norm of A and find

$$\|A\|_F = \sqrt{\text{trace}\left(A^\dagger A\right)} = \sqrt{\text{trace}\left(V \Sigma^2 V^\dagger\right)} = \sqrt{\text{trace}\left(\Sigma^2\right)}, \tag{2.31}$$

The Frobenius norm of A is simply given by the square root of the sum over the squared singular values of A. This insight is fundamentally important for the approximation of the matrix A by a matrix B of smaller rank $r_B < r_A$, which, as we will see, lies at the heart of the density matrix renormalization group.

Theorem (Eckart-Young-Mirsky) (73) If $r_B < r_A = \text{rank}(A)$ and

$$A_{r_B} = \sum_{i=1}^{r_B} \sigma_i \mathbf{u}_i \mathbf{v}_i^T, \tag{2.32}$$

then

$$\min_{\text{rank}(B) = r_B} \|A - B\|_F = \|A - A_{r_B}\|_F = \sum_{i=r_B+1}^{r_A} \left|\sigma_i\right|^2. \tag{2.33}$$

The matrix B with rank $r_B < r_A$, which is the closest approximation to the matrix A, is thus given by A_{r_B}.

The SVD does not only see use in matrix product state methods for many body quantum mechanics problems but has a wide range of diverse applications. It is included in a number of numerical algorithms for linear algebra problems. It is heavily used in signal and image processing as well as numerical weather prediction. It is also an important tool for big data problems such as the movie suggestion process of the online movie streaming service Netflix.
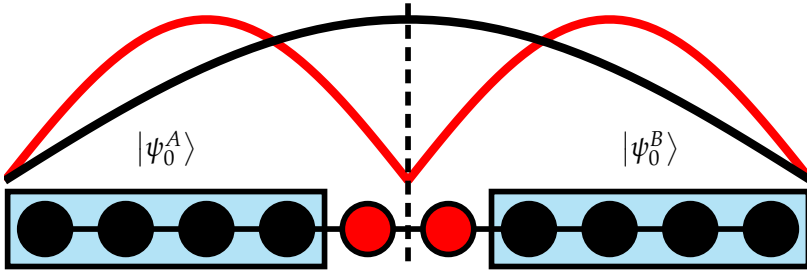
2.3 Density Matrix Renormalization Group

2.3.1 Numerical Renormalization Group

The Numerical Renormalization Group (NRG) can be regarded as the ancestor of the Density Matrix Renormalization Group and other Matrix Product State methods. It pioneered the idea of constructing the many-body Hilbert space and the matrices of the operators acting in it in an iterative process, whereby subspaces of the Hilbert space, that were deemed unlikely to contribute to the ground state, are already projected out, before increasing the size of the Hilbert space again in the next iteration step. The criterion by which subspaces are chosen to be kept or rejected is their energy expectation value. In a typical iteration step, only a fraction $1/D_i$ of the eigenbasis - the one with the lowest energy - is kept, where D_i is the size of the local basis of the system. This way, the retained many-body Hilbert space stays approximately the same size in each iteration step, allowing for the study of lattice sizes that approach the thermodynamic limit. This method was conceived by Kenneth G. Wilson [39] and successfully used to study the Kondo problem. It typically excels at computing the ground state as well as equilibrium properties of quantum impurity systems, due to the separation of energy scales that often occurs in such systems. When such a separation of energy scales is not present in the system, the truncation criterion of NRG fails to select the suitable subspaces of the Hilbert space. A straightforward example of this is the translation invariant, non-interacting tight-binding chain, where the single particle eigenstates are known to be

$$|\psi_n(x)\rangle \propto \sin\left(\frac{n\pi x}{L}\right) \qquad n = 1, \dots, L\,. \qquad (2.34)$$

Here, the low energy eigenstates of a smaller system have little overlap with the ground state of a larger system and thus do not form a suitable subspace to be kept when increasing the system size. This mismatch is illustrated in figure 2.1. To specifically identify subspaces of states that feature heavily in the ground state of larger systems, infinite lattice DMRG creates a clone system B of the current system A and then computes the ground state $|\psi_0^{A+B}\rangle$ of the combined system $A + B$. After constructing the density matrix $\rho^{A+B} = |\psi_0^{A+B}\rangle\langle\psi_0^{A+B}|$ and tracing out the clone system, the subspace of states with sufficiently large eigenvalues in the resulting reduced density matrix $\rho^A = \mathrm{tr}_B\,\rho^{A+B}$, is the subspace of $\mathcal{H}_A$ that should be kept.

Figure 2.1: *Schematic representation of the ground states $|\psi_0^{A,B}\rangle$ of two smaller non-interacting tight-binding blocks (red), and the ground state $|\psi_0^{A+B}\rangle$ of a superblock comprising the two (black). It becomes obvious that the ground states of the smaller blocks are not a suitable basis in which to describe the ground state of the superblock. Inspired by [74].*

The prominence of the reduced density matrix in the selection criterion originally motivated the name *Density Matrix Renormalization Group*, while the *Renormalization Group* moniker highlights that inspiration was drawn from NRG, as the method itself is not a renormalization group.

2.3.2 Truncation Scheme

As mentioned, the aim in DMRG is to project out subspaces of the Hilbert space $\mathcal{H}_A$ such that the (ground state) wave function in the remaining Hilbert space is as good an approximation of the original wave function as possible. This is equivalent to a minimization of

$$\left\| |\psi_0\rangle - |\psi_0^{\mathcal{S}}\rangle \right\|_2 , \tag{2.35}$$

where $|\psi_0^{\mathcal{S}}\rangle$ is the projection of $|\psi_0\rangle$ onto the retained subspace $\mathcal{S}$. In order to identify the relevant basis vectors of the system A, that have finite overlap with the wave function $|\psi_0\rangle$ in the combined Hilbert space $\mathcal{H}_A \otimes \mathcal{H}_B$, it is convenient to express $|\psi_0\rangle$ as a bipartite quantum state and hence as a matrix

$$|\psi_0\rangle = \sum_{i=1}^{D_A} \sum_{j=1}^{D_B} a_{ij} |l_i^A\rangle \otimes |l_j^B\rangle , \tag{2.36}$$

where D_A is the size of the Hilbert space $\mathcal{H}_A$ of A and D_B the size of the Hilbert space $\mathcal{H}_B$ of B and the overlap with the basis vector $|l_i^A\rangle$ of system A is given by

$$\langle l_i^A | \psi_0 \rangle = \sum_{j=1}^{D_B} a_{ij} . \tag{2.37}$$

In this matrix formulation of $|\psi_0\rangle$, the measure that one wishes to minimize becomes

$$\left\| |\psi_0\rangle - |\psi_0^{\mathcal{S}}\rangle \right\|_F , \tag{2.38}$$

where the index F denotes the Frobenius norm, which we have introduced in section 2.2. It can then be argued in mathematically rigorous fashion that the truncation scheme of DMRG coincides with the optimal method to minimize this particular norm.

DMRG and SVD

If the wave function $|\psi_0\rangle$ is given in the form of a matrix, as is the case in equation (2.36), then it is possible to perform a SVD to arrive at

$$|\psi_0\rangle = \sum_{i=1}^{D_A} \sum_{j=1}^{D_B} a_{ij} |l_i^A\rangle \otimes |l_j^B\rangle = \sum_{i=1}^{D_A} \sum_{j=1}^{D_B} \sum_{\alpha,\beta=1}^{D_N} \left[U_{i\alpha} \Sigma_{\alpha\beta} V_{\beta j}^\dagger \right] |l_i^A\rangle \otimes |l_j^B\rangle , \tag{2.39}$$

where $D_N = \min\{D_A, D_B\}$. The singular matrix $\Sigma_{\alpha\beta}$ is diagonal and the singular values satisfy $\Sigma_{\alpha\alpha} = \sigma_\alpha \geq 0$.

The Eckart-Young-Mirsky-Theorem states that the single best approximation of $|\psi_0\rangle$ by a matrix of smaller rank $r = D_{\mathcal{S}} < D_N$ is given by

$$|\psi_0^{\mathcal{S}}\rangle = \sum_{i=1}^{D_A} \sum_{j=1}^{D_B} \sum_{\alpha,\beta=1}^{D_{\mathcal{S}}} \left[U_{i\alpha} \Sigma_{\alpha\beta} V_{\beta j}^\dagger \right] |l_i^A\rangle \otimes |l_j^B\rangle , \tag{2.40}$$

and the subspace of $\mathcal{H}_A$ that contains $|\psi_0^{\mathcal{S}}\rangle$ is

$$\mathcal{S}_A = \mathrm{span}\{u_1, \ldots, u_r\} , \tag{2.41}$$

with

$$\{|u_n\rangle\} = \sum_{i=1}^{D_A} U^\dagger |l_i^A\rangle . \tag{2.42}$$

The original selection rule of keeping the subspace spanned by the vectors in $\mathcal{H}_A$, that correspond to the $D_{\mathcal{S}}$ largest eigenvalues of the reduced density matrix $\rho^A = \mathrm{tr}_B \rho^{A+B}$, is equivalent to keeping the subspace spanned by the left singular vectors corresponding to the $D_{\mathcal{S}}$ largest singular values. To show this, we express the density matrix ρ^{A+B} as

$$\rho^{A+B} = |\psi_0\rangle\langle\psi_0| = U\Sigma V^\dagger V \Sigma^T U^\dagger = U\Sigma^2 U^\dagger , \tag{2.43}$$

where $V^\dagger V = \mathbb{1}$ implicitly traces out the (clone) system B. Since U and V are unitary transformations and Σ^2 is diagonal, we establish that $\mathrm{diag}(\Sigma) = [\mathrm{diag}(\rho_A)]^{1/2}$ and that both approaches select the same subspace $\mathcal{S}_A$.

DMRG and Entanglement

As part of the DMRG algorithm, one calculates the ground state $|\psi_0\rangle$ of a composite system of $A + B$. The particles in the subsystems then share information and can no longer be described independently from particles in the other subsystem. They have become entangled. This bipartite entanglement is also encoded in the wavefunction $|\psi_0\rangle$ and the reduced density matrix $\rho^A = \text{tr}_B \rho^{A+B}$ in turn describes a mixed quantum state. In the absence of entanglement, ρ^A could also describe a pure quantum state and there would be a basis in which ρ^A contains only a single finite matrix element. The entanglement between particles in systems A and B imposes that ρ^A contains multiple nonzero eigenvalues. A measure for the entanglement is given by the Von Neumann entanglement entropy

$$S(\rho^A) = -\text{tr}\left(\rho^A \log \rho^A\right) = -\text{tr}\left(\rho^B \log \rho^B\right) = S(\rho^B). \tag{2.44}$$

The larger the entanglement entropy, the larger the amount of nonzero eigenvalues of both ρ^A and ρ^B. This implies that the subspace $\mathcal{S}_A$ needs to be chosen larger as well in order to maintain a good approximation of $|\psi_0\rangle$. An arbitrary quantum state with large bipartite entanglement necissitates subspaces of unmanageable dimensions. Yet DMRG is saved by the fact that the low-energy eigenstates of gapped Hamiltonians with local interactions[3] obey an area law for the entanglement entropy [159]. This means that the bipartite entanglement grows proportional to the surface between the systems A and B, which in one dimension usually includes only one or few links. The amount of non-negligible eigenstates of ρ^A is therefore comparatively small. Sometime after the introduction of DMRG, it was also found that states obeying an area law for the entanglement entropy can be represented as tensor network states [43–45]. This has given rise to a plethora of numerical methods that directly work with tensor network states [46, 75, 76] and DMRG has since been identified as a tool to create and optimize matrix product states[47].

2.3.3 DMRG algorithm

Infinite lattice DMRG

The infinite lattice algorithm is used in our DMRG implementation to expand the system up to the desired final size and to give an initial guess of suitable truncated Hilbert spaces. It is most useful for translation invariant systems, where small systems already contain all relevant interaction terms. In each iteration step, the algorithm adds a number of new system sites and then applies the DMRG truncation scheme to keep the dimension of the Hilbert space contained.

(i) Create an initial system A_i with n_i lattice sites and corresponding Hilbert space

$$\mathcal{H}_{A_i} = \mathcal{H}_1 \otimes \mathcal{H}_2 \otimes \cdots \otimes \mathcal{H}_{n_i}. \tag{2.45}$$

---

[3]Most physically interesting one-dimensional model systems fortunately fall into this category
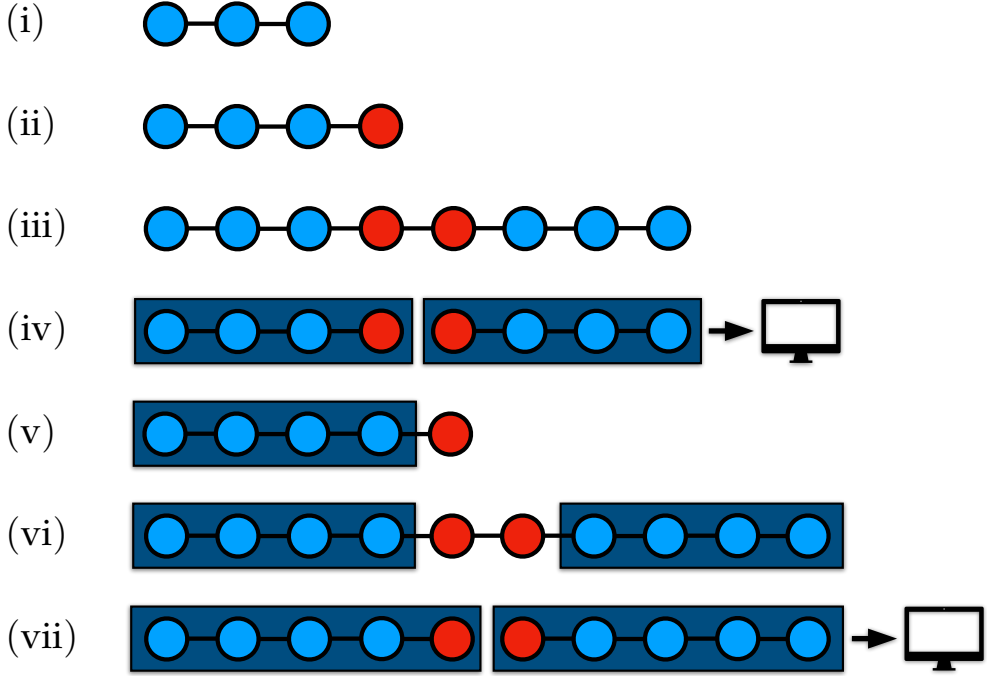
Figure 2.2: *Schematic representation of the steps of the infinite lattice algorithm in our implementation of the DMRG*

The initial size n_i should be chosen small enough that the Hamiltonian H_{A_i} in $\mathcal{H}_{A_i}$ can still be diagonalized exactly.

(ii) Add a new lattice site to the system A.

(iii) Create a clone system B from A. Form a compound block $A + B$ with Hilbert space

$$\mathcal{H}_{A+B} = \mathcal{H}_{A_i} \otimes \mathcal{H}_i \otimes \mathcal{H}_i \otimes \mathcal{H}_{A_i}, \qquad (2.46)$$

and create the Hamiltonian H_{A+B} in this Hilbert space.

(iv) Diagonalize H_{A+B} to find the ground state $|\psi_0^{A+B}\rangle$. Perform a SVD for $|\psi_0^{A+B}\rangle$ to determine the optimal truncated subspaces $\mathcal{H}_A^{\mathcal{S}}$ and $\mathcal{H}_B^{\mathcal{S}}$. Project the Hamiltonian H_{A+B} and necessary local operators onto the subspaces $\mathcal{H}_A^{\mathcal{S}}$ and $\mathcal{H}_B^{\mathcal{S}}$. Save the resulting Hamiltonians $H_A^{\mathcal{S}}$, $H_B^{\mathcal{S}}$ and operators to the disk.

(v) Add one new lattice site each to A with $\mathcal{H}_A^{\mathcal{S}}$ and B with $\mathcal{H}_B^{\mathcal{S}}$.

(vi) Form a compound block $A + B$ with Hilbert space

$$\mathcal{H}_{A+B} = \mathcal{H}_A^{\mathcal{S}} \otimes \mathcal{H}_i \otimes \mathcal{H}_i \otimes \mathcal{H}_B^{\mathcal{S}}, \tag{2.47}$$

and create the Hamiltonian H_{A+B} in this Hilbert space.

(vii) Diagonalize H_{A+B} to find the ground state $|\psi_0^{A+B}\rangle$. Perform a SVD for $|\psi_0^{A+B}\rangle$ to determine the optimal truncated subspaces $\mathcal{H}_A^{\mathcal{S}}$ and $\mathcal{H}_B^{\mathcal{S}}$. Project the Hamiltonian H_{A+B} and necessary local operators onto the subspaces $\mathcal{H}_A^{\mathcal{S}}$ and $\mathcal{H}_B^{\mathcal{S}}$. Save the resulting Hamiltonians $H_A^{\mathcal{S}}$, $H_B^{\mathcal{S}}$ and operators to the disk. Continue with step (v).

Once the compound system $A + B$ has reached the desired system size, the infinite lattice algorithm is halted. The truncated Hamiltonians $H_A^{\mathcal{S}}$ and $H_B^{\mathcal{S}}$ for left and right systems of different size are then used as the starting point for the subsequent finite lattice algorithm. An illustration of the infinite lattice algorithm is shown in figure 2.3.

Finite lattice DMRG

The finite lattice algorithm improves upon the subspaces selected by the infinite lattice algorithm through a sweeping process, in which complete local Hilbert spaces $\mathcal{H}_i$ are reintroduced again. By repeatedly reintroducing previously discarded subspaces of the Hilbert space and then truncating again, the chosen subspace of the Hilbert space converges on the optimal subspace. In terms of matrix product states, the finite lattice algorithm can be formulated as a variational wavefunction optimization [48, 76].

(i) Retrieve from the disk the Hamiltonians $H_A^{\mathcal{S}}$ and $H_B^{\mathcal{S}}$ and local operators for the system sizes $n_A = L/2 - 1$ and $n_B = L/2 - 1$.

(ii) Add one new lattice site each to A with $\mathcal{H}_A^{\mathcal{S}}$ and B with $\mathcal{H}_B^{\mathcal{S}}$. Then form a compound block $A + B$ with Hilbert space

$$\mathcal{H}_{A+B} = \mathcal{H}_A^{\mathcal{S}} \otimes \mathcal{H}_i \otimes \mathcal{H}_i \otimes \mathcal{H}_B^{\mathcal{S}}, \tag{2.48}$$

and create the Hamiltonian H_{A+B} in this Hilbert space.

(iii) Diagonalize H_{A+B} to find the ground state $|\psi_0^{A+B}\rangle$. Perform a SVD for $|\psi_0^{A+B}\rangle$ to determine the optimal truncated subspaces $\mathcal{H}_A^{\mathcal{S}}$ and $\mathcal{H}_B^{\mathcal{S}}$. Project the Hamiltonian H_{A+B} and the necessary local operators onto the subspaces $\mathcal{H}_A^{\mathcal{S}}$ and $\mathcal{H}_B^{\mathcal{S}}$. Replace the previously stored truncated Hamiltonians $H_A^{\mathcal{S}}$, $H_B^{\mathcal{S}}$ and local operators for system sizes $n_A + 1$ and $n_B + 1$ with the newly determined ones.

(iv) Set $n_A = L/2$ and $n_B = L/2 - 2$ and read the corresponding truncated Hamiltonians and operators from the disk. Then repeat steps (ii) and (iii).
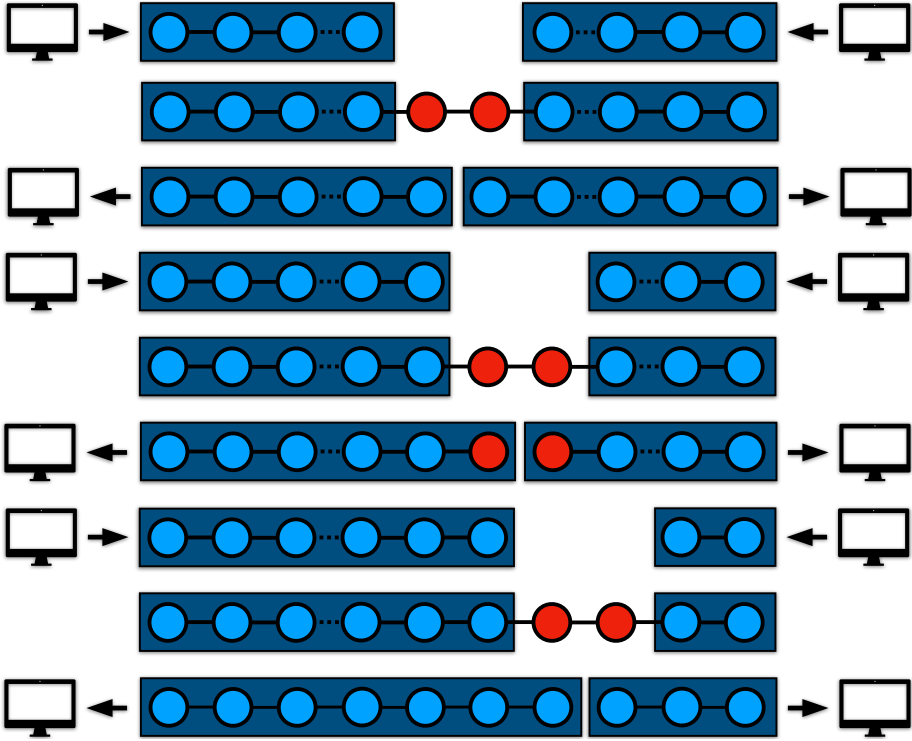
Figure 2.3: *Schematic representation of the steps of the finite lattice algorithm in our implementation of the DMRG*

(v) Continue increasing the size of A and decreasing the size of B until $n_B = n_i$. Then reverse the sweeping direction, expanding B and reducing A.

After a few sweeps, the calculated ground state energy should have converged on the actual ground state energy. The wave function $|\psi_0^{\mathcal{S}}\rangle$ is now a good approximation of the actual ground state wave function and can be used to calculate ground state expectation values.

$$\langle \hat{O} \rangle_0 = \langle \psi_0^{\mathcal{S}} | \hat{O} | \psi_0^{\mathcal{S}} \rangle, \tag{2.49}$$

where the operators $\hat{O}$ have to be added beforehand to the list of operators that are projected onto the truncated Hilbert spaces during the infinite and finite lattice algorithms.

2.3.4 Time evolution

For the work presented in this thesis, we have studied the dynamics of many-body systems after quenches. In this context, it is necessary to track the evolution of the

wave function $|\psi_0\rangle$ governed by a Hamiltonian of which $|\psi_0\rangle$ not an eigenstate. In general, this evolution will involve states that are not included in the truncated subspaces determined by the DMRG algorithm. We therefore modify the algorithm to ensure that each state visited by the time evolution is part of the truncated Hilbert space. After each diagonalization of H_{A+B} in the infinite and finite lattice algorithm, we perform a time evolution

$$|\psi\left(n\Delta t\right)\rangle = e^{-\mathrm{i}Hn\Delta t}|\psi(t=0)\rangle\,, \tag{2.50}$$

where the matrix exponential is computed via (2.16). We determine each basis vector $|l_i\rangle$ for which

$$\sum_{n=0}^{n_f} |\langle l_i|e^{-\mathrm{i}Hn\Delta t}|\psi_0\rangle| \neq 0\,, \tag{2.51}$$

or

$$\sum_{n=0}^{n_f} |\langle l_i|\hat{O}\,e^{-\mathrm{i}Hn\Delta t}|\psi_0\rangle| \neq 0\,, \tag{2.52}$$

where n_f denotes the final time step. We then create a superposition

$$|\psi_t\rangle = \frac{1}{N}\left(|\psi_0\rangle + \sum_i |l_i\rangle\right)\,, \tag{2.53}$$

where N is a normalization factor. The SVD is performed for $|\psi_t\rangle$ instead of $|\psi_0\rangle$ and the truncated subspace is thus guaranteed to include each relevant state for the time evolution. Many other DMRG implementations employ a Suzuki-Trotter decomposition [75–77] for the time evolution, particularly if they are using tensor networks to represent the wave functions.

2.4 Tomonaga Luttinger model

Before we discuss our own work on the non-equilibrium dynamics of low-dimensional, strongly correlated systems in the subsequent chapters, we would like to use this section to introduce one of the studied model systems and utilize it to illustrate the extent to which working in 1D is different from 2D or 3D. In this, we will closely follow the introductions by Giamarchi [8] as well as Bruus and Flensberg [49] and encourage the reader who wants to get a deeper insight into one-dimensional physics to delve into the book by Giamarchi. Arguably one of the most simple and most extensively studied 1D model systems is the XXZ Heisenberg chain. It was originally devised to describe the relevant physics of a chain of atoms featuring half-filled outer s-shells, where the spins of the electrons occupying the s-shell are coupled by an anisotropic exchange interaction to the electron spins in the s-shells of the atoms closest by [50–52]. Formulated in terms of a Hamiltonian the model reads

$$H_{XXZ} = J \sum_i S_i^x S_{i-1}^x + S_i^y S_{i-1}^y + \Delta S_i^z S_{i-1}^z \,, \tag{2.54}$$

where the spin operators are S_i^α are expressed in terms of Pauli matrices σ^α as $S_i^\alpha = \sigma_i^\alpha/2$, J establishes the overall energy scale, and Δ determines the anisotropy of the exchange interaction. As becomes clear in the limit $\Delta/J \to \infty$, the XXZ chain can be seen as a generalization of the famous Ising chain, the ubiquitous testbed of statistical physics. As such it is also a popular model on which to study quantum phase transitions. The model is quantum critical and thus gapless for $|\Delta|/J \leq 1$. For $|\Delta|/J > 1$ it becomes gapped and favors ferromagnetic ordering of the spins if $\Delta/J < -1$ or antiferromagnetic ordering if $\Delta/J > 1$. A special trait of the XXZ Heisenberg chain, and indeed the first characteristically 1D trait to be mentioned here, is that it is exactly solvable by means of Bethe ansatz [53]. In fact, the isotropic form of the XXZ chain, ie $\Delta/J = 1$, is the model that Hans Bethe originally solved this way [27], hence the name Bethe ansatz. For the purposes of this section, it useful to recast the Hamiltonian (2.54) of the XXZ chain into a different form. For this we introduce operators

$$\sigma_i^+ = \frac{1}{2} \left(\sigma_i^x + i\sigma_i^y \right) \,, \tag{2.55}$$

$$\sigma_i^- = \frac{1}{2} \left(\sigma_i^x - i\sigma_i^y \right) \,, \tag{2.56}$$

which respectively raise or lower the spin in z-direction on the lattice site i. In this form, the spin operators bear resemblance to fermionic creation and annihilation operators, in that $\sigma^- | \downarrow \rangle \equiv 0$ and $\sigma^+ | \uparrow \rangle \equiv 0$. The spin operators and fermion operators are indeed linked through the Jordan-Wigner transformation. The Jordan-Wigner transformation reads

$$\sigma_i^+ = e^{-i\pi \sum_{j<i} c_j^\dagger c_j} c_i^\dagger \,, \tag{2.57}$$

$$\sigma_i^- = e^{+i\pi \sum_{j<i} c_j^\dagger c_j} c_i \,, \tag{2.58}$$

$$\sigma_i^z = 2c_i^\dagger c_i - 1 \,, \tag{2.59}$$

where $c_i^\dagger$ creates a spinless fermion and c_i annihilates a spinless fermion on lattice site i. The so-called 'string' $\sim \exp(\pm i\pi \sum_{j<i} c_j^\dagger c_j)$ ensures that the spin operators satisfy the bosonic commutation relations

$$\left[\sigma_i^-, \sigma_j^+\right] = \delta_{ij}, \tag{2.60}$$

while the fermionic operators obey anticommutation relations

$$\left\{c_i, c_j^\dagger\right\} = \delta_{ij}. \tag{2.61}$$

Due to this string, the Jordan-Wigner transformation is a tool that is almost exclusively used in 1D, as it introduces long-range interactions even in highly local models in higher dimensions. When applied to the XXZ chain, we obtain

$$H = J\sum_i \frac{1}{2}\left(c_i^\dagger c_{i-1} + \text{h.c.}\right) + \Delta\left(c_i^\dagger c_i - \frac{1}{2}\right)\left(c_{i-1}^\dagger c_{i-1} - \frac{1}{2}\right) \tag{2.62}$$

$$= \sum_i -t\left(c_i^\dagger c_{i-1} + \text{h.c.}\right) + V\left(c_i^\dagger c_i - \frac{1}{2}\right)\left(c_{i-1}^\dagger c_{i-1} - \frac{1}{2}\right),$$

where for the second term we have introduced a canonical transformation $c_j \to (-1)^j c_j$, which shifts the momenta from $k \in [0, 2\pi/a]$ to $k \in [-\pi/a, \pi/a]$, where a is the lattice spacing. In the noninteracting limit $V = \Delta = 0$, this Hamiltonian is easily diagonalized by a Fourier transformation

$$c_j = \frac{1}{\sqrt{L}} \sum_k c_k e^{-ikj}, \tag{2.63}$$

resulting in

$$H = \sum_{k=-\frac{\pi}{a}}^{+\frac{\pi}{a}} \varepsilon(k) c_k^\dagger c_k, \tag{2.64}$$

with the dispersion relation

$$\varepsilon(k) = -2t\cos(k). \tag{2.65}$$

The ground state of this Hamiltonian is a filled Fermi sea, where each state with momentum $|k| \le k_F$ and $\varepsilon(k) \le 0$ is occupied by a spinless fermion. As is evident from figure 2.4, the excited states with low energies feature additional fermions and/or holes close to the Fermi points $\pm k_F$. For the purpose of describing the system at low energies[4] it thus makes sense to focus on the states in the vicinity of $\pm k_F$. This is

---

[4]Even on the hottest day ever recorded in the Netherlands ($T_{\text{NL}} \simeq 308\,\text{K}$) the low energy assumption was still very much appropriate considering that the energy scale t is typically $\sim 1\text{eV}$ while $k_B T_{\text{NL}} \simeq 2.7 \times 10^{-2}\,\text{eV}$.
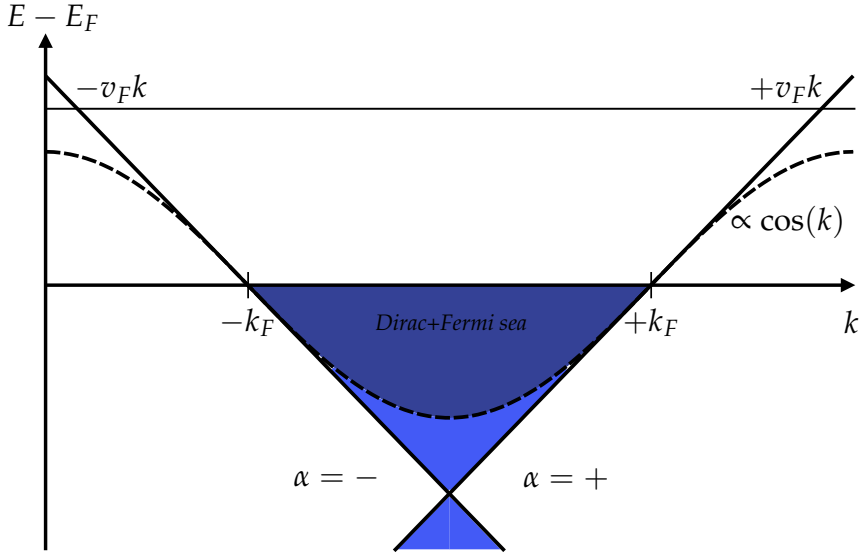
Figure 2.4: *Depiction of the dispersion relation $E(k) \propto \cos(k)$ of the tight-binding chain - or equivalently the XX Heisenberg chain - and the filled Fermi sea corresponding to its ground state at half-filling. Linearizing the model at the Fermi points $k = \pm k_F$ results in a model that contains two particle species, left-movers ($\alpha = -$) and right-movers ($\alpha = -$). The ground state is now given by a Dirac sea that extends to $E = -\infty$.*

under the assumption that the spectrum of the system is gapless, which for the XXZ chain is true for $|\Delta|/J \leq 1$. A closer look at figures 2.4 and 2.5 reveals that the dispersion relation close to $\pm k_F$ is well approximated by a straight line with the slope given by the Fermi velocity

$$v_F = \partial_k \varepsilon(k)\Big|_{k=k_F} . \tag{2.66}$$

For a linear dispersion relation, particle-hole excitations of momentum q, where a particle is excited from momentum state $|k| \leq k_F$ to momentum state $|k + q| > k_F$ and leaves behind a hole at state k, become indistinguishable excitations with a well-defined energy-momentum relation $E(q) = v_F q$. We illustrate this in figure 2.5. The linear character of the low energy excitation spectrum of gapless one-dimensional systems is captured by the Tomonaga Luttinger model. Its Hamiltonian reads

$$H_{TL} = \sum_{\alpha=\pm} \sum_{k=-\infty}^{\infty} v_F \left[(\alpha k - k_F) c_{\alpha,k}^\dagger c_{\alpha,k} \right] , \tag{2.67}$$
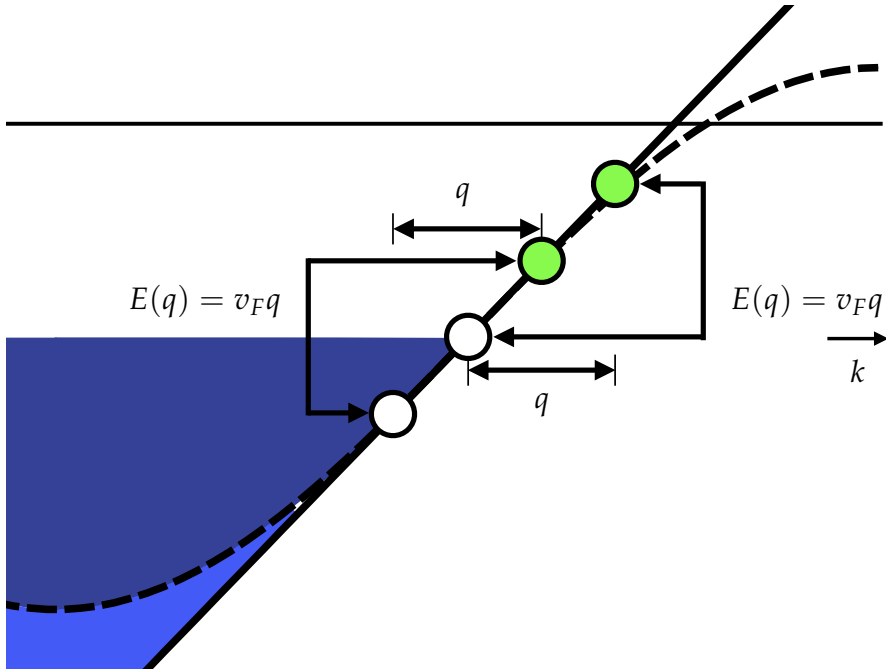
Figure 2.5: *For a linear dispersion, the particle hole excitations of equal momentum q also have the same excitation energy $E(q) = v_F q$, irrespective of the initial momentum k of the particle.*

where we have introduced two species of fermions, the so-called *left-movers* ($\alpha = -$) and *right-movers* ($\alpha = +$) and extended the momenta to $k \pm \infty$ to establish that the particle-hole excitations become completely independent of the initial momentum k of the particle. A filled Fermi sea is consequently replaced by a filled Dirac sea, where each state $-\infty < k \leq k_F$ is occupied by a fermion. In figure 2.4 we show a schematic representation of the ground state of the original model and the ground state of the Tomonaga Luttinger (TL) model. The introduction of an infinite number of occupied states $(\alpha k - k_F) < 0$ brings about the risk of infinities in the expectation values of certain operators, particularly the density operator $\rho(q)$. We will thus subsequently make use of normal ordering. In a normal ordered product : $ABCD$:, all creation operators are located to the left of the annihilation operators of the respective the vacuum state $|0\rangle$. If the normal ordered product contains only two operators A and B, it is equivalent to substracting the vacuum expectation value from the regular product of the operators as in

$$: AB := AB - \langle 0|AB|0\rangle . \tag{2.68}$$

In this normal ordering, the operator $\rho(q)$, that creates a density fluctuation in the form of a superposition of particle-hole excitations with momentum q, becomes

$$: \rho_\alpha^\dagger(q) := \begin{cases} \sum_k c_{\alpha,k+q}^\dagger c_{\alpha,k} & q \neq 0 \\ \sum_k \left(c_{\alpha,k}^\dagger c_{\alpha,k} - \langle 0 | c_{\alpha,k}^\dagger c_{\alpha,k} | 0 \rangle \right) = N_\alpha & q = 0 \end{cases} . \tag{2.69}$$

As we have seen before, these density fluctuations are well-defined excitations and can form an alternative basis with q as a good quantum number. The advantage of changing to this particular basis becomes clear when we examine the interaction term, which so far we have neglected, in momentum space. It reads

$$H_{\text{int}} = \frac{1}{2L} \sum_{k,k',q} V(q) c_{k+q}^\dagger c_{k'-q}^\dagger c_{k'} c_k , \tag{2.70}$$

where $V(q)$ is the momentum dependent interaction strength. When we express it in terms of the density fluctation operators, we arrive at

$$H_{\text{int}} = \frac{1}{2L} \sum_{q,\alpha,\alpha'} V(q) \rho_\alpha(q) \rho_{\alpha'}(-q) , \tag{2.71}$$

where we note that in momentum space $\rho^\dagger(q) = \rho(-q)$, as the particle density $\rho(x)$ is always real. We recognize that the interaction H_{int}, which had been a quartic operator before, becomes quadratic in the new basis. A translation-invariant Hamiltonian with exclusively quadratic interactions is in principle always diagonalizable [54], whereas we still lack a general way of diagonalizing Hamiltonians that feature quartic terms. The question is now whether this reduction of the interaction from a quartic to a quadratic operator in the density fluctuation basis has come at the cost of a quartic kinetic term of the Hamiltonian, in which case no simplification would have been achieved. The density fluations contain pairs of fermionic operators and thus have the characteristics of bosonic operators. We now have to show that they also obey bosonic commutation relations. For this, we express the density fluctua-

tions in terms of the original fermionic operators and find

$$
\begin{aligned}
\left[\rho_\alpha^\dagger(q), \rho_\alpha(q')\right] &= \sum_{k,k'} \left[c_{\alpha,k+q}^\dagger c_{\alpha,k}, c_{\alpha,k'-q'}^\dagger c_{k'}\right] \\
&= \sum_{k,k'} \left(c_{\alpha,k+q}^\dagger c_{\alpha,k} c_{\alpha,k'-q'}^\dagger c_{\alpha,k} - c_{\alpha,k'-q'}^\dagger c_{\alpha,k'} c_{\alpha,k+q}^\dagger c_{\alpha,k}\right) \\
&= \sum_{k,k'} \left(c_{\alpha,k+q}^\dagger [\delta_{k,k'-q'} - c_{\alpha,k'-q'}^\dagger c_{\alpha,k}]c_{\alpha,k'}\right. \\
&\qquad\left. - c_{\alpha,k'-q'}^\dagger [\delta_{k',k+q} - c_{\alpha,k+q}^\dagger c_{\alpha,k'}]c_{\alpha,k}\right) \\
&= \sum_{k'} \left(c_{\alpha,k'+q-q'}^\dagger c_{\alpha,k'} - c_{\alpha,k'-q'}^\dagger c_{\alpha,k'-q}\right) \\
&= \sum_{k'} \left(: c_{\alpha,k'+q-q'}^\dagger c_{\alpha,k'}: - : c_{\alpha,k'-q'}^\dagger c_{\alpha,k'-q}:\right) \\
&\qquad + \sum_{k'} \left(\langle 0|c_{\alpha,k'+q-q'}^\dagger c_{\alpha,k'}|0\rangle - \langle 0|c_{\alpha,k'-q'}^\dagger c_{\alpha,k'-q}|0\rangle\right) \\
&= \sum_{k'} \left(\langle 0|c_{\alpha,k'+q-q'}^\dagger c_{\alpha,k'}|0\rangle - \langle 0|c_{\alpha,k'-q'}^\dagger c_{\alpha,k'-q}|0\rangle\right) \\
&= \delta_{q,q'} \sum_{k'} \left(\langle 0|c_{\alpha,k'}^\dagger c_{\alpha,k'}|0\rangle - \langle 0|c_{\alpha,k'-q}^\dagger c_{\alpha,k'-q}|0\rangle\right) \\
&= -\alpha \delta_{q,q'} \frac{qL}{2\pi}\,.
\end{aligned}
\tag{2.72}
$$

The result of the commutator is indeed equal to that of a bosonic operator, up to a normalization factor. Regarding the density fluctuation operators $\rho^\dagger(q)$ and $\rho(q)$ as bosonic creation and annihilation operators is therefore justified. More formally, we introduce the bosonic operators

$$
b_q^\dagger = \sqrt{\frac{2\pi}{L|q|}} \sum_\alpha \theta(\alpha q)\rho_\alpha^\dagger(q)\,,
\tag{2.73}
$$

$$
b_q = \sqrt{\frac{2\pi}{L|q|}} \sum_\alpha \theta(\alpha q)\rho_\alpha(q)\,,
$$

where $\theta(x)$ is the Heaviside function and we require $q \neq 0$. To find an expression for the kinetic part H_{TL} of the Hamiltonian in terms of the bosonic operators, we

compute the commutator[5]

$$\left[H_{\text{TL}}, b_q\right] \underset{q \neq 0}{=} \sqrt{\frac{2\pi}{L|q|}} \sum_{k,k'} \left[v_F(k - k_F)c^\dagger_{+,k}c_{+,k}, c^\dagger_{+,k'-q}c_{+,k'}\right] \tag{2.74}$$

$$= \sqrt{\frac{2\pi}{L|q|}} \sum_{k,k'} v_F(k - k_F) \left(c^\dagger_{+,k}[\delta_{k,k'-q} - c^\dagger_{+,k'-q}c_{+,k}]c_{+,k'}\right.$$

$$\left. - c^\dagger_{+,k'-q}[\delta_{k',k} - c^\dagger_{+,k}c_{+,k'}]c_{+,k}\right)$$

$$= \sqrt{\frac{2\pi}{L|q|}} \sum_{k,k'} v_F(k - k_F) \left(c^\dagger_{+,k}c_{+,k'}\delta_{k,k'-q} - c^\dagger_{+,k'-q}c_{+,k}\delta_{k',k}\right)$$

$$= \sqrt{\frac{2\pi}{L|q|}} \sum_{k} v_F(k - k_F) \left(c^\dagger_{+,k}c_{+,k+q} - c^\dagger_{+,k-q}c_{+,k}\right)$$

$$= -v_F q b_q\,.$$

Up to a prefactor $v_F q$, the result of this commutator is identical to the commutator of the bosonic number operator with the bosonic annihilation operator

$$[b^\dagger_q b_q, b_q] = -b_q\,, \tag{2.75}$$

indicating that we can also express H_{TL} as

$$H_{\text{TL}} = \sum_{q \neq 0} v_F|q|b^\dagger_q b_q + \frac{\pi v_F}{L} \sum_{\alpha = \pm} N^2_\alpha\,. \tag{2.76}$$

Equation (2.76) is an exceptional result. That the interaction expressed in terms of density fluctuation is quadratic, is not all that surprising, but that the kinetic term remains quadratic in this basis of density fluctuations as well makes the Tomonaga Luttinger model as a low energy description of a multitude of 1D model systems extremely useful and is a unique feature of 1D physics. To discuss the bosonic representation of the full interacting Hamiltonian, it is useful to introduce field operators

$$\phi(x) = -\left(N_+ + N_-\right)\frac{\pi x}{L} - \frac{i\pi}{L}\sum_{q \neq 0}\frac{1}{q}\sqrt{\frac{|q|L}{2\pi}}e^{-\eta|q|/2 - iqx}\left(b^\dagger_q + b_{-q}\right)\,, \tag{2.77}$$

$$\theta(x) = \left(N_+ - N_-\right)\frac{\pi x}{L} + \frac{i\pi}{L}\sum_{q \neq 0}\frac{1}{|q|}\sqrt{\frac{|q|L}{2\pi}}e^{-\eta|q|/2 - iqx}\left(b^\dagger_q - b_{-q}\right)\,. \tag{2.78}$$

The commutator of these field operators is

$$\lim_{\eta \to 0} \lim_{L \to \infty} \left[\phi(x_1), \theta(x_2)\right] = i\frac{\pi}{2}\text{sign}(x_2 - x_1)\,, \tag{2.79}$$

---

[5]We only present the calculation of the commutator for *right-movers*. The commutator for *left-movers* follows along the same lines.
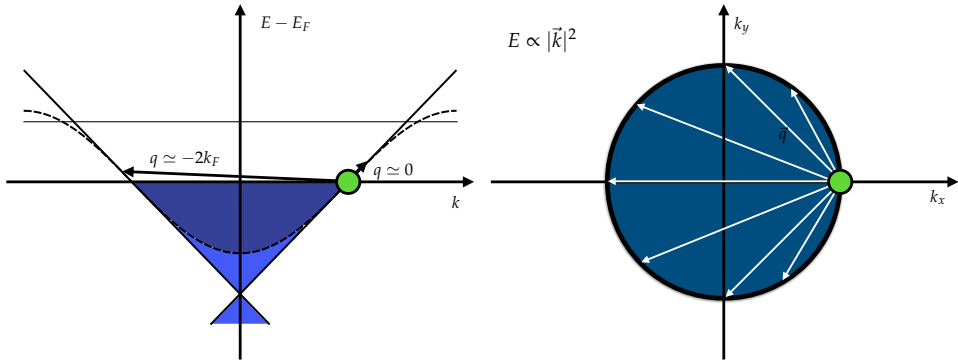
Figure 2.6: *Low energy scattering processes on top of a filled Fermi (Dirac) sea in 1D can only invole momenta $q \simeq 0$ and $q \simeq \pm 2k_F$. In 2D, low energy scattering processes can involve any momentum $\vec{q}$ that maps one momentum state $\vec{k} = (k_x, k_y)$ on the circle, which represents the Fermi surface, to another momentum state $\vec{k}' = (k'_x, k'_y)$ on this circle.*

revealing that the field $\theta(x_2)$ is not yet the conjugate momentum to the field $\phi(x_1)$. It turns out that

$$\left[\phi(x_1), \partial_x \theta(x_2)\right] = i\pi\delta(x_2 - x_1), \tag{2.80}$$

such that we can define the actual conjugate momentum to the field $\phi(x_1)$ as

$$\Pi(x) = -\frac{1}{\pi}\partial_x \theta(x). \tag{2.81}$$

In terms of the fields $\phi(x)$ and $\Pi(x)$, the Tomonaga Luttinger model manifests itself as a simple quadratic field theory, which reads

$$H_{\text{TL}} = \frac{1}{2\pi} \int dx \, v_F \left[\left(\pi\Pi(x)\right)^2 + \left(\partial_x\phi(x)\right)^2\right]. \tag{2.82}$$

Next, we will discuss the limitations that being in one dimension imposes in possible interactions between fermions in the system. From figure 2.4 it becomes apparent that excitations of energy $E(q) \simeq 0$ can only occur for momenta $q \simeq 0$ and $q \simeq \pm 2k_F$. This is because the Fermi surface in 1D consists of only two points $k = \pm k_F$, whereas in higher dimensions the Fermi surface contains a vast amount of points that can take part in a scattering process with $E(\vec{q}) \simeq 0$, as illustrated in figure 2.6. Considering that most interaction processes will occur for $q \simeq 0$ and that the interaction strength $V(q)$ is smooth in the vicinity of $q = 0$, we can fix $V(q) = V(0)$. With this in
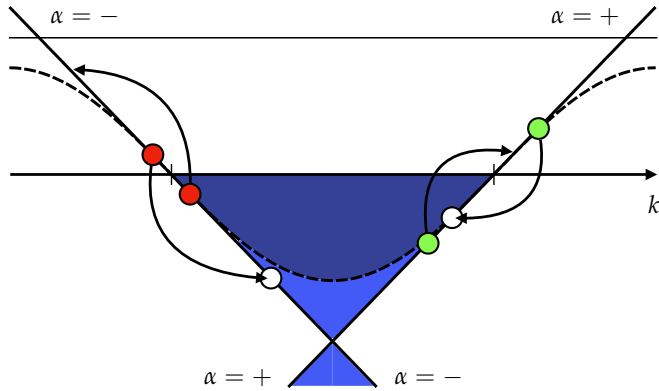
Figure 2.7: *Schematic representation of the interaction g_4, which couples left moving densities to left moving densities and right moving densities to right moving densities. The particles are drawn at larger distances from the Fermi surface to increase visibility.*
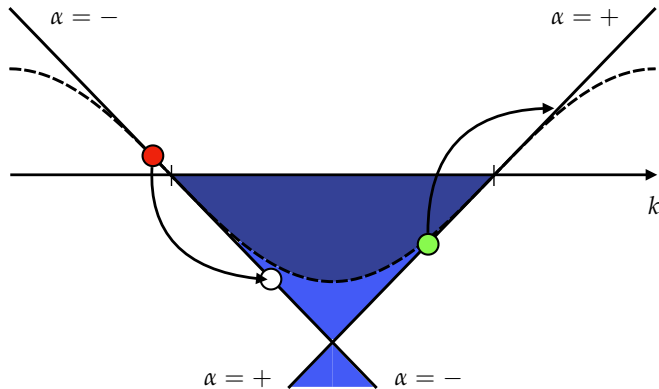
Figure 2.8: *Schematic representation of the interaction g_2, which couples left moving densities to right moving densities and vice versa. The particles are drawn at larger distances from the Fermi surface to increase visibility.*

mind, our interaction term (2.71) can be approximated by

$$H_{\text{int}} \simeq \sum_{q,\alpha,\alpha'} V(0) \rho_\alpha(q) \rho_{\alpha'}(-q) \tag{2.83}$$

$$= \sum_q g_4 \Big(\rho_+(q)\rho_+(-q) + \rho_-(q)\rho_-(-q) \Big)$$

$$+ g_2 \Big(\rho_+(q)\rho_-(-q) + \rho_-(q)\rho_+(-q) \Big), \tag{2.84}$$

where g_4 denotes the part of the interaction $V(0)$, that couples density fluctuations of the same fermion species and g_2 is the part of the interaction, that couples density fluctuations of opposite fermion species. A sketch of the interaction g_4 for left-movers and right-movers is shown in fig. 2.7 albeit with particles located far from the Fermi surface to enhance visibility. In the same manner, we illustrate the interaction g_2, which couples left-moving and right-moving density fluctuations in fig. 2.8. Expressed in terms of the field operators the interaction g_4 reads

$$\frac{g_4}{2} \sum_\alpha \rho_\alpha(q)\rho_\alpha(-q) = \frac{g_4}{(2\pi)^2} \Big[(\partial_x \phi(x))^2 + (\pi\Pi(x))^2 \Big], \tag{2.85}$$

and the interaction g_2 becomes

$$g_2 \Big(\rho_+(q)\rho_-(-q) \Big) = \frac{g_2}{(2\pi)^2} \Big[(\partial_x \phi(x))^2 - (\pi\Pi(x))^2 \Big]. \tag{2.86}$$

Adding the interaction term in this form to H_{TL} yields

$$H = \frac{\tilde{v}}{2\pi} \int dx \, \left[K(\pi\Pi(x))^2 + \frac{1}{K}(\partial_x\phi(x))^2 \right], \tag{2.87}$$

with

$$\tilde{v} = v_F \sqrt{ \left(1 - \frac{g_4}{2\pi v_F} \right)^2 - \left(\frac{g_2}{2\pi v_F} \right)^2 }, \tag{2.88}$$

and

$$K = \sqrt{ \frac{1 + \frac{g_4}{2\pi v_F} - \frac{g_2}{2\pi v_F}}{1 + \frac{g_4}{2\pi v_F} + \frac{g_2}{2\pi v_F}} }. \tag{2.89}$$

Equations (2.87) to (2.89) are the central result of this section. They reflect, that in one dimension, the low energy properties of a system of interacting spinless fermions are universally described by a noninteracting bosonic theory. The quasiparticle excitations of this theory are not dressed fermions, as in the Fermi liquid theory, which describes interacting fermion systems in higher dimensions, but density fluctuations with a rescaled velocity $\tilde{v} \neq v_F$. This picture is referred to as *Luttinger liquid*. The

microscopic details of the original model are encoded in the values $\tilde{v}$ and K, which are called the *Luttinger parameters*. For fermions with spin, the calculations become more tedious, which is why we will not present them here but refer the reader to the book by Giamarchi and the review article by Schoeller and von Delft [8, 78]. The essential result is the appearance of a second species of density fluctuations, namely a spin-density fluctuation. The rescaled velocity v_s of this *spinon* excitation is in general different from the rescaled velocity v_c of the *holon*, the quasiparticle excitation of the charge density fluctations. This leads to the famous phenomenon of spin-charge separation that we will touch upon in the following chapter.

Chapter 3

3 Observation of spin-charge separation via the LDOS

In this chapter, we numerically calculate the local density of states (LDOS) of a one-dimensional Mott insulator with open boundaries, which is modelled microscopically by a (extended) Hubbard chain at half filling. In the Fourier transform of the LDOS we identify several dispersing features corresponding to propagating charge and spin degrees of freedom, thus providing a visualisation of the spin-charge separation in the system.

This chapter is organised as follows: In Sec. 5.2 we present the microscopic models to be analysed and discuss the basic setup. In Sec. 3.3 we give a brief summary of the numerical method we employ to calculate the single-particle Green function. Our results for the LDOS of the Mott insulators with open boundary conditions are discussed in Sec. 3.4. In Sec. 3.5 we study the effect of a boundary potential on the LDOS, in particular we analyse the properties of the boundary bound state existing for sufficiently strong boundary potentials. In Sec. 3.6 we summarise our results.

3.1 Introduction

One-dimensional systems remain a fascinating field in condensed-matter physics since they constitute prime examples for the breakdown of Fermi-liquid theory, which has to be replaced by the Luttinger-liquid paradigm [8]. Arguably the most dramatic consequence of this is the absence of electron-like quasiparticles, manifesting itself in the separation of spin and charge degrees of freedom visible for example in angle-resolved photoemission [55, 80, 81], transport [82–84], scanning tunneling spectroscopy [85] or resonant inelastic X-ray scattering [86] experiments as well as analytical [87–90] and numerical studies of several one-dimensional models [91–100].

The spectral properties of one-dimensional electron systems have been intensively investigated in the past. These works considered the gapless Luttinger liquid [8, 79, 101–105], gapped systems like Mott insulators or charge-density wave states,

[107, 108, 154] Luttinger liquids with impurities [109–117], corrections to the Luttinger model due to non-linear dispersions [118, 119] or the momentum dependence of the two-particle interaction [155], as well as additional phonon degrees of freedom [121–125]. These investigations uncovered universal power-law behaviour at low energies as well as deviations thereof, spin-charge separation visible in the propagation modes, and signatures of these features in various experimental probes. Recently the measurement of the local density of states (LDOS) has also been discussed in the context of ultra-cold atomic gases [126].

In this article we consider another situation, namely the microscopic study of the boundary effects on one-dimensional Mott insulators. Specifically we numerically study the LDOS of one-dimensional Hubbard models with open, ie, hard-wall, boundary conditions, where the system is at half filling and thus in its Mott phase. A previous field-theoretical analysis [129, 156] has shown that the Fourier transform of the LDOS[157] exhibits clear signatures of propagating spin and charge degrees of freedom, thus providing a way to detect spin-charge separation. Furthermore, an additional boundary potential may lead to the formation of a boundary bound state, which manifests itself as a non-dispersing feature in the LDOS. The aim of our work is to calculate the Fourier transform of the LDOS directly in the microscopic lattice model using a multi-target [144, 179] variant of the density matrix renormalisation group (DMRG) method [40] employing an expansion in Chebyshev polynomials. We find our numerical results to be fully consistent with the analytical predictions both qualitatively, ie, concerning the number of dispersion modes and their basic properties, as well as quantitatively with respect to the numerical values of the effective parameters like the Mott gap and spin and charge velocities as compared to the exact results obtained from the Bethe ansatz [31]. Thus our work provides a microscopic calculation of the Fourier transform of the LDOS in a gapped, strongly correlated electron system, showing spin-charge separation as well as the formation of a boundary bound state.

3.2 Model

In this work we analyse the LDOS of the one-dimensional Hubbard model [31] at half filling. The Hamiltonian is given by

$$H = -t \sum_{\sigma,j=0}^{L-2} \left(c_{j,\sigma}^\dagger c_{j+1,\sigma} + c_{j+1,\sigma}^\dagger c_{j,\sigma} \right) \tag{3.1}$$

$$+ U \sum_{j=0}^{L-1} \left(n_{j,\uparrow} - \frac{1}{2} \right) \left(n_{j,\downarrow} - \frac{1}{2} \right),$$

where $c_{j,\sigma}$ and $c_{j,\sigma}^\dagger$ denote the annihilation and creation operators for electrons with spin $\sigma = \uparrow, \downarrow$ at lattice site j and $n_{j,\sigma} = c_{j,\sigma}^\dagger c_{j,\sigma}$ the corresponding density operators. The parameters t and $U > 0$ describe the hopping and repulsive on-site interaction

respectively. Furthermore we consider a chain with L sites and open boundary conditions. Since the system is assumed to be at half filling, the Fermi momentum is given by $k_\mathrm{F} = \pi/2$.

As is well known,[8, 31] in the Hubbard model at half filling, ie, when there are L electrons in the system, the repulsive interaction opens a gap in the charge sector and the system becomes a Mott insulator. Using bosonisation the low-energy behaviour of the system is described by the massive Thirring model;[132] the LDOS of which in the presence of boundaries has been analysed in Refs. [129, 156]. The main objective of our article is the comparison of the LDOS of the Hubbard model (3.1) with the field-theoretical results obtained in the Thirring model. Hereby the effective parameters in the field theory, ie, the mass gap and velocities, can be obtained from the exact Bethe-ansatz solution of the Hubbard model. This allows us to choose the microscopic parameters such that the expected features of the Fourier transformed LDOS can be easily resolved in the numerical results.

In addition to the standard Hubbard model (3.1) we also consider its extension including a nearest-neighbour interaction V, ie, the Hamiltonian is given by[133]

$$H_\mathrm{ext} = H + V \sum_{j=0}^{L-2} \left(n_j - 1 \right) \left(n_{j+1} - 1 \right)$$
(3.2)

where $n_j = n_{j,\uparrow} + n_{j,\downarrow}$ is the total electron density. The low-energy regime of the extended Hubbard model (3.2) is still described [132] by the massive Thirring model. However, since (3.2) is no longer integrable, the explicit relation between the microscopic parameters t, U and V and the field-theory ones is not known. Thus the investigation of the phase diagram of the extended Hubbard model at half filling had to be performed by numerical means.[134–138] Using these results we choose the microscopic parameters such that the system is well inside the Mott-insulating phase with an energy gap $\Delta \approx \mathcal{O}(t)$ so that we are able to clearly resolve the interesting features in our numerical results.

3.3 Green function

In order to determine the LDOS we calculate the retarded Green function in frequency space using an expansion of the occurring resolvent in Chebyshev polynomials [144]. An alternative numerical approach consists in the expansion of the Lehmann representation of the spectral function in Chebyshev polynomials, the kernel polynomial method (KPM), see Refs. [139–142]. In contrast we specifically evaluate the complete (real and imaginary part) Green functions

$$G^\mathrm{R}(\omega, x) = G^+(\omega, x) - G^-(\omega, x)$$
(3.3)

with

$$G^+(\omega, x) = \langle\Psi_0|c_{j,\sigma}\frac{1}{E_0 - H + \omega + i\eta}c_{j,\sigma}^\dagger|\Psi_0\rangle, \tag{3.4}$$

$$G^-(\omega, x) = \langle\Psi_0|c_{j,\sigma}^\dagger\frac{1}{E_0 - H - \omega - i\eta}c_{j,\sigma}|\Psi_0\rangle. \tag{3.5}$$

Here $|\Psi_0\rangle$ denotes the ground state of the system with energy E_0. Note that since we are interested in the LDOS we have already taken the electron creation and annihilation operators to be at the same site $x = ja_0$ with a_0 denoting the lattice spacing. Furthermore, since the systems we consider possess spin-rotation invariance we have suppressed the formal spin dependence of the Green functions.

In Eqs. (3.4) and (3.5) we have included the convergence factor η, which in the continuum limit should be taken as $\eta \to 0^+$. In the numerical evaluations it has to be larger than the finite level splitting brought about by the finite system size. At the same time η has to be smaller than any physically relevant energy scale in order to resolve the relevant features of the spectrum. To attain a small value of η we employ a Chebyshev polynomial expansion approach for the resolvents in (3.4) and (3.5). More details on this approach can be found in Refs. [143, 144].

The applied Chebyshev expansion is based on the representation of the functions

$$f^\pm(\omega, z) = \frac{1}{\pm\omega - z} \tag{3.6}$$

in terms of Chebyshev polynomials

$$f^\pm(\omega, z) = \sum_{n=0}^\infty \alpha_n^\pm(\omega)T_n(z), \quad -1 \le z \le 1. \tag{3.7}$$

The expansion coefficients are given by

$$\begin{aligned}
\alpha_n^\pm(\omega) &= \frac{2}{\pi(1 + \delta_{n,0})} \int_{-1}^1 dz \frac{T_n(z)}{\sqrt{1 - z^2}} \frac{1}{\pm\omega - z} \\
&= \frac{2 - \delta_{n,0}}{(\pm\omega)^{n+1}\left(1 + \sqrt{\omega^2}\frac{\sqrt{\omega^2-1}}{\omega^2}\right)^n \sqrt{1 - \omega^{-2}}},
\end{aligned} \tag{3.8}$$

where $\alpha_n^\pm(\omega) \equiv \alpha_n^\pm(\omega + i\eta)$ is a function of the artificial broadening η which would theoretically allow arbitrarily small η. The Chebyshev polynomials $T_n(z)$ are defined by their recursion relation

$$T_0(z) = 1, \tag{3.9}$$

$$T_1(z) = z, \tag{3.10}$$

$$T_{n+1}(z) = 2zT_n(z) - T_{n-1}(z), \quad n \ge 2, \tag{3.11}$$

and fulfil

$$\int_{-1}^1 \frac{dz}{\sqrt{1 - z^2}} T_n(z)T_m(z) = \frac{\pi}{2}\delta_{n,m}(1 + \delta_{n,0}) \tag{3.12}$$

as well as

$$T_{2n}(z) = 2T_n(z)^2 - T_0(z), \tag{3.13}$$

$$T_{2n-1}(z) = 2T_{n-1}(z)\, T_n(z) - T_1(z). \tag{3.14}$$

In order to apply the expansion (3.7), which is only valid for $|z| \leq 1$, to the resolvents appearing in the Green functions, we first have to rescale the energies. To this end we run initial DMRG calculations to determine the ground-state energy E_0 as well as the smallest and the largest energies of the system with $L \pm 1$ electrons. This allows us to find the scaling factor a and shift b such that the operator

$$a(H - E_0) - b \tag{3.15}$$

has a spectrum between -1 and 1 in the sectors with $L \pm 1$ particles. Then the Green function (3.4) can be expressed as

$$G^+(\omega, x) = a \sum_{n=0}^{\infty} \alpha_n^+ [a(\omega + i\eta) - b]\, \mu_n^+(x), \tag{3.16}$$

where the Chebyshev moments

$$\mu_n^+(x) = \langle \Psi_0 | c_{j,\sigma}\, T_n[a(H - E_0) - b]\, c_{j,\sigma}^\dagger | \Psi_0 \rangle \tag{3.17}$$

(recall $x = j a_0$) can be evaluated recursively via

$$\mu_n^+(x) = \langle \Psi_0 | c_\sigma(x) | \Phi_n^+ \rangle \tag{3.18}$$

with the recursion relations

$$|\Phi_0^+\rangle = c_\sigma^\dagger(x)|\Psi_0\rangle, \tag{3.19}$$

$$|\Phi_1^+\rangle = [a(H - E_0) - b]|\Phi_0^+\rangle, \tag{3.20}$$

$$|\Phi_{n+1}^+\rangle = 2[a(H - E_0) - b]|\Phi_n^+\rangle - |\Phi_{n-1}^+\rangle. \tag{3.21}$$

Similarly, for the Green function (3.5) we obtain the expansion

$$G^-(\omega, x) = a \sum_{n=0}^{\infty} \alpha_n^- [a(\omega + i\eta) + b]\, \mu_n^-(x), \tag{3.22}$$

where

$$\mu_n^-(x) = \langle \Psi_0 | c_{j,\sigma}^\dagger\, T_n[a(H - E_0) - b]\, c_{j,\sigma} | \Psi_0 \rangle. \tag{3.23}$$

In the numerical evaluations the sums appearing in (3.16) and (3.22) are truncated at $N/2$. The moments $\mu_n^\pm$ are calculated iteratively from (3.19)–(3.21) using DMRG. During the DMRG finite-lattice sweeps we determine each state $|\Phi_0^\pm\rangle, \ldots, |\Phi_{N/2}^\pm\rangle$ and include it into a modified density matrix. By performing a singular-value decomposition of this modified density matrix we ensure that all the states $|\Phi_0^\pm\rangle, \ldots, |\Phi_{N/2}^\pm\rangle$ are part of the Hilbert space after the DMRG truncation. The moments for $n =$

$N/2 + 1, \ldots, N$ are then obtained employing (3.13) and (3.14) as $\mu_{2n}^{\pm} = 2\langle \Phi_n^{\pm} | \Phi_n^{\pm} \rangle - \langle \Phi_0^{\pm} | \Phi_0^{\pm} \rangle$ and $\mu_{2n-1}^{\pm} = 2\langle \Phi_{n-1}^{\pm} | \Phi_n^{\pm} \rangle - \langle \Phi_0^{\pm} | \Phi_1^{\pm} \rangle$.

Finally, we note that the Chebyshev moments $\mu_n^{\pm}$ are typically strongly oscillating with respect to the index n. Therefore, the final results oscillate slightly when changing the value of N. On the other hand, we find small oscillating parts in the spectral function if we choose N too small. Both effects can be avoided by implementing a smoothing window for the last N_S moments. Throughout this article we use a $\cos^2$-filter for the last $N_S = N/5$ moments. This way one can obtain a good approximation for the spectral function using a smaller number of moments N. Previously it was observed[144] that the number of required Chebyshev moments sufficient to approximate the Green function is inversely proportional to the width of the spectrum a and the desired artificial broadening η, ie, $N \simeq (a\eta)^{-1}$. Throughout this work we use $N \geq 1000$ Chebyshev moments for the series expansion of the Green function. Furthermore, η is chosen such that the resulting curves become smooth and artificial features are suppressed (see Fig. 3.2 for an example).

We note that while the Chebyshev expansion is efficient in getting the complete frequency range of the Green function, a correction vector based method[135, 145–148, 183] would enable a better frequency resolution. However, in contrast to impurity problems, where one can increase the energy resolution via energy dependent discretisation schemes,[143, 148] here one can increase the inherent discretisation only by increasing the system size. In addition to solving the LDOS for all lattice sites one would have to perform a run for each desired frequency.

3.4 LDOS

The LDOS is obtained from the retarded Green function (3.3) in the usual way. As was noted by Kivelson et al.[157] in the study of Luttinger liquids with boundaries, it is useful to consider the Fourier transform of the LDOS, as physical properties like the dispersions of propagating quasiparticles can be more easily identified. Since we consider a finite chain of length L we analyse

$$N(\omega, Q) = -\frac{1}{\pi} \sqrt{\frac{2}{L+1}} \sum_{j=0}^{L-1} \operatorname{Im} G^{R}(\omega, x) \, \sin[Q(j+1)], \qquad (3.24)$$

where the momenta Q take the values $Q = \pi k/(L+1), k = 1, \ldots, L$. We note that the LDOS is directly related to the tunneling current measured in scanning tunneling microscopy experiments, thus its Fourier transform (3.24) is experimentally accessible. In the following we focus on the LDOS for positive energies; the LDOS for negative energies can be analysed analogously.

The LDOS of the low-energy effective field theory of the Hubbard models (3.1) and (3.2) has been analysed[1] in Refs. [129, 156]. In the field-theoretical description

---

[1]We note that the Refs. [129, 156] consider the case of a charge-density wave state where the gap appears in the spin sector. The results for the Mott insulator considered in our article are obtained by simply interchanging spin and charge sectors in Refs. [156].

the momentum regimes $Q \approx 0$ and $Q \approx \pm 2k_F = \pi$ are treated separately. For small momenta $Q \approx 0$ the main features of the Fourier transform (3.24) are a strong divergence at $Q = 0$ as well as a propagating excitation in the gapped charge sector above the Mott gap. In contrast, the behaviour at momenta $Q \approx 2k_F$ shows a divergence at $Q = 2k_F$, a propagating excitation in the charge sector as well as a linearly dispersing excitation in the gapless spin sector. Furthermore there exists a critical momentum above which a second linearly dispersing mode becomes visible. In addition, it was shown that certain boundary conditions lead to the formation of boundary bound states which manifest themselves as non-propagating features in the LDOS.

The main aim of our article is the calculation of the Fourier transform of the LDOS (3.24) in the microscopic models (3.1) and (3.2) and its comparison to the field-theoretical predictions.[129, 156] We start with the standard Hubbard chain (3.1) before considering the extended version (3.2). In Sec. 3.5 we then analyse the effect of additional boundary potentials which give rise to the existence of boundary bound states.

3.4.1 Standard Hubbard model

We first consider the Fourier transform of the LDOS (3.24) in the standard Hubbard model (3.1). The results in the vicinity of $Q = 0$ and $Q = 2k_F = \pi$ are shown in Figs. 3.1 and 3.3 respectively, where we have chosen a repulsive interaction of $U = 4.5\,t$ corresponding to the dimensionless Hubbard parameter $u = U/(4t) = 1.125$ and $L = 90$ lattice sites. Throughout our article we use the hopping parameter $t = 1$ as our unit of energy.

As is well known, the Hubbard model (3.1) is exactly solvable by Bethe ansatz. [31] In particular, the velocities of the spin and charge excitations v_s and v_c as well as the Mott gap Δ can be determined analytically; the results in the thermodynamic limit read

$$\Delta = -2 + 2u + 2 \int_0^\infty \frac{d\omega}{\omega} \frac{J_1(\omega)e^{-u\omega}}{\cosh(u\omega)}, \tag{3.25}$$

$$v_c = \frac{2}{1 - \xi_{0,0}(u)} \sqrt{u - 1 + \xi_{-1,1}(u)} \sqrt{1 - \xi_{1,1}(u)}, \tag{3.26}$$

$$v_s = \frac{2I_1\left(\frac{\pi}{2u}\right)}{I_0\left(\frac{\pi}{2u}\right)}, \tag{3.27}$$

$$\xi_{m,n}(u) = 2 \int_0^\infty \frac{d\omega\, \omega^m J_n(\omega)}{1 + \exp(2\omega u)}, \tag{3.28}$$

where $J_n(z)$ and $I_n(z)$ denote the Bessel functions and modified Bessel functions of the first kind respectively. Our chosen parameters for the microscopic system correspond to $v_c > v_s$.

In Fig. 3.1 we plot $N(\omega, Q)$ in the vicinity of small momenta $Q \approx 0$. The LDOS is dominated by a strong peak at $Q = \pi/91$. For this the spectral weight inside the gap
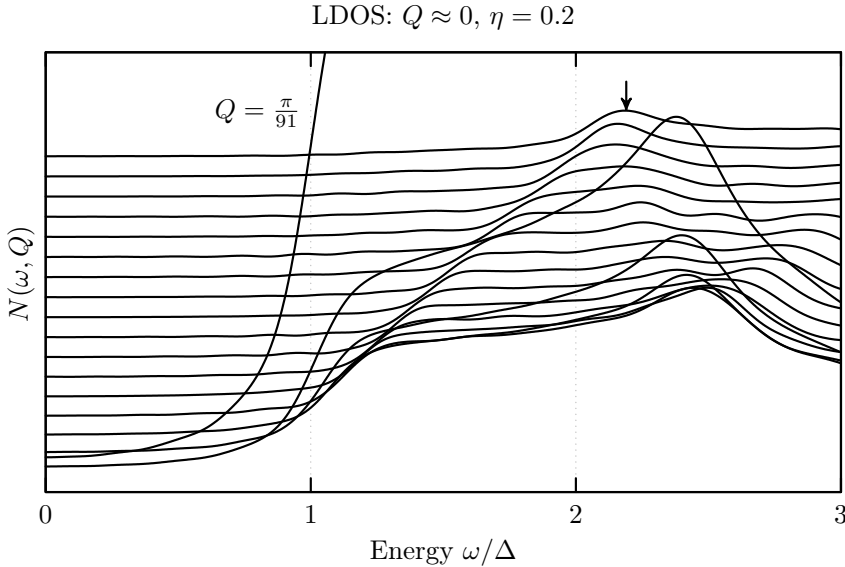
Figure 3.1: *Fourier transform of the LDOS $N(\omega, Q)$ for interaction $u = U/4 = 1.125$ (recall $t = 1$), $L = 90$ lattice sites, broadening $\eta = 0.2$ and momenta $Q = \pi/91, 2\pi/91, \ldots, 18\pi/91$ (from bottom to top). The curves are constant Q-scans that have been offset along the y-axis by a constant with respect to one another. $N(\omega, Q)$ is dominated by a strong peak at $Q = \pi/91 \approx 0$ which is only partially displayed in the figure in order to improve visibility for the other cuts (see also Fig. 3.2). We clearly observe the Mott gap Δ as well as a dispersing feature indicated by the arrow. This feature corresponds to propagating charge excitations, it follows the dispersion relation $E_c(Q)$ given in (3.29) with $v_c \simeq 2.67$ obtained from (3.26).*

is a result of the finite broadening η as shown in Fig. 3.2. Thus all features appear at energies $\omega \geq \Delta$, clearly showing that the system is in a gapped phase. The observed energy gap Δ agrees perfectly with the value $\Delta(u = 1.125) \simeq 0.83$ obtained from the Bethe ansatz (3.25) in the thermodynamic limit. This suggests that the length of our chain is long enough to avoid significant finite-size effects in our results.

The Fourier transform of the LDOS for small momenta is dominated by a global maximum at $Q = \pi/91 \approx 0$. This peak is attributed to a spin-density wave pinned at the boundary, it is also well visible in the field-theoretical results.[129, 156] At low energies above the energy gap we further observe a dispersing feature indicated by the arrow. This again agrees well with the results from the field theory that predict a
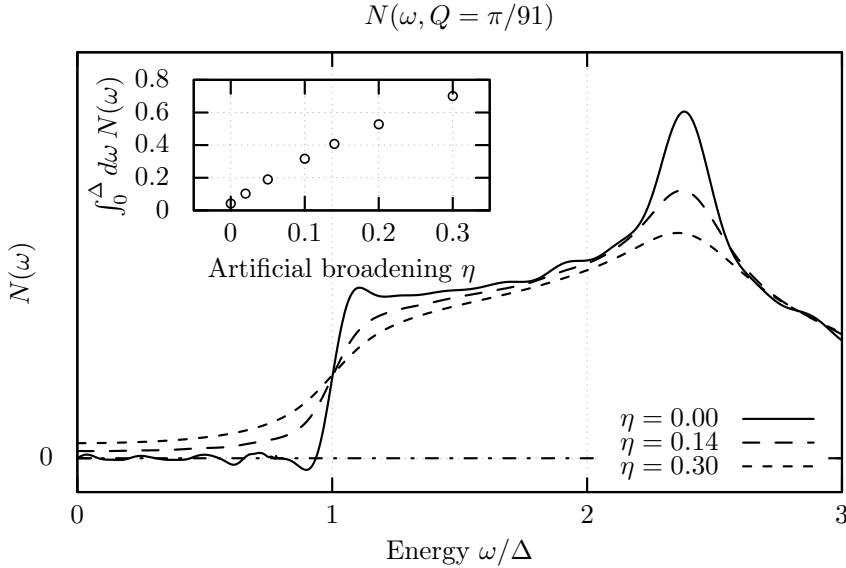
Figure 3.2: *LDOS $N(\omega, Q)$ at $Q = \pi/91$ and for different broadenings η. All other parameters are as in Fig. 3.1. We observe that the jump at $\omega = \Delta$ becomes sharper for $\eta \to 0$, however, artificial oscillations due to the Gibbs phenomenon increase. Inset: Integrated spectral weight inside the gap as a function of the broadening η.*

gapped, dispersing charge excitation with dispersion relation

$$E_c(q) = \sqrt{\left(\frac{v_c q}{2}\right)^2 + \Delta^2},\tag{3.29}$$

where $q = Q$ and v_c is the velocity of the charge excitations. The Bethe-ansatz solution (3.26) gives the value $v_c(u = 1.125) \simeq 2.67$, which is in excellent agreement with the velocity observed in the plot. The physical origin of this dispersing feature is the decay of the electronic excitation into gapped charge and gapless spin excitations. In the process giving rise to (3.29) the external momentum q is taken by the charge excitation propagating through the system and eventually getting reflected at the boundary, while the spin excitation does not propagate and thus possesses zero momentum. The appearance of $v_c/2$ in (3.29) originates from the fact that the charge excitation has to propagate to the boundary and back, thus covering the distance $2x$.

In addition, in Fig. 3.1 we observe a second feature at higher energy $\omega = \Delta_2 \simeq 2.4\,\Delta$. This feature seemingly follows the dispersion relation (3.29) albeit with the gap value replaced by Δ_2. While the first dispersing feature can be identified with the propagation of a single excitation in the massive charge sector of the field the-
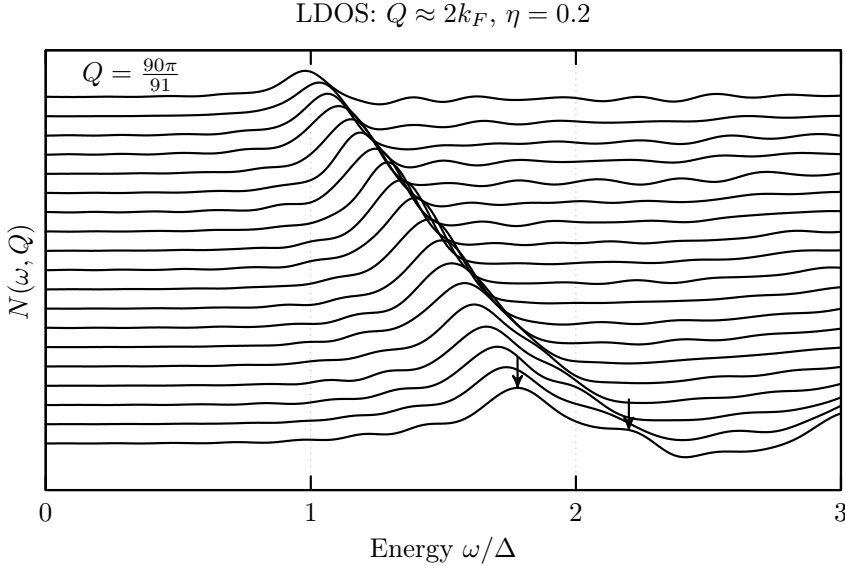
Figure 3.3: *$N(\omega, 2k_F - q)$ for momenta in the vicinity of $Q = 2k_F = \pi$ with $q = 2k_F - Q = \pi/91, 2\pi/91, \ldots, 19\pi/L$ (from top to bottom). All other parameters are as in Fig. 3.1. The curves are constant q-scans that have been offset along the y-axis by a constant with respect to one another. We observe two dispersing features (indicated by the arrows) at $E_c(q)$ and $E_s(q)$ originating from propagating charge and spin excitations respectively.*

ory, this second feature cannot be accounted for in the field theory. In particular, higher-order processes containing more than one excitation in the charge sector are found to be strongly suppressed and do not possess any non-trivial features. Thus we conclude that the field theory cannot explain the dispersing feature observed in Fig. 3.1 at $\omega \sim 2.4 \Delta$. Furthermore, the field theory makes predictions about the power-law decay of $N(\omega, Q)$ at $Q = 0$ which, however, cannot be resolved in our numerical data. For the observation of such features we would require a significantly higher resolution, both in energy and momentum. This can in turn only be achieved by turning to a significantly larger system size and a higher amount of calculated Chebyshev moments.

We now turn our attention to momenta in the vicinity of $Q = 2k_F = \pi$. We first note that features in this momentum regime originate from umklapp processes coupling left- and right-moving modes which are absent in translationally invariant systems and thus constitute a particularly clean way to investigate the boundary effects. In Fig. 3.3 we again observe the existence of the Mott gap as well as two
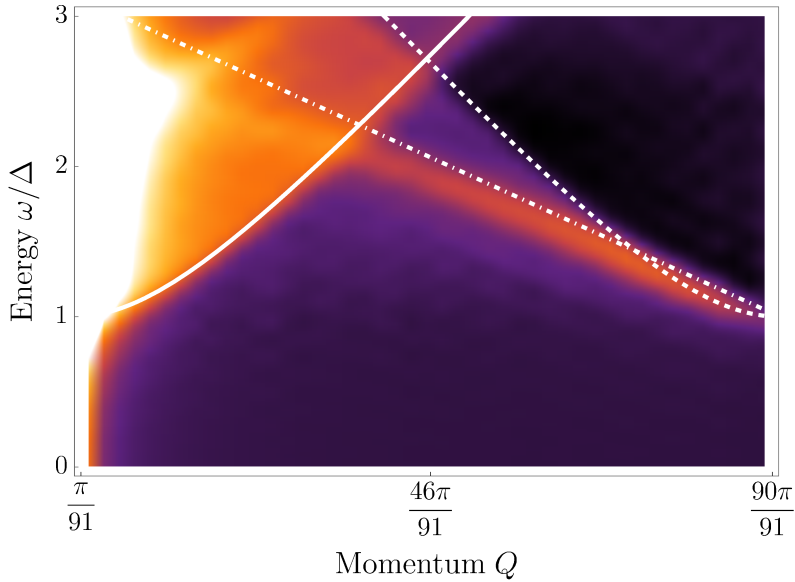
Figure 3.4: *Contour plot of the LDOS $N(\omega, Q)$ for the parameters of Fig. 3.1. The dominant, white peak at $Q \approx 0$ is due to the spin-density wave pinned at the boundary. The solid and dashed lines indicate the holon dispersion (3.29) around $Q = 0$ and $Q = 2k_F$ respectively, the dashed-dotted line represents the spinon dispersion (3.30) around $Q = 2k_F$. The parameters Δ, v_c and v_s used in the plot were obtained from the Bethe ansatz for the bulk system (3.25)–(3.27), ie, there is no free fitting parameter.*

dispersing features at $E_c(q)$ as defined in (3.29) and

$$E_s(q) = \frac{v_s|q|}{2} + \Delta, \tag{3.30}$$

both indicated by the arrows. The spin velocity observed in the plot is in excellent agreement with the Bethe-ansatz result (3.27) giving $v_s(u = 1.125) \simeq 1.14$. While the feature adhering to (3.29) is again due to a propagating charge excitation, the feature following (3.30) originates from the propagation of spin excitations with the charge excitation possessing zero momentum. Furthermore, we note that in contrast to the field-theoretical prediction we observe only one linearly dispersing mode. In order to understand this we recall that the two linearly dispersing modes are energetically separated by[129, 156] $\Delta[1 - \sqrt{1 - (v_s/v_c)^2}] \approx 0.1\Delta \approx 0.08$, where in the last step we have put in the parameters used in Fig. 3.3. Assuming that we need about four points to clearly distinguish the two maxima, we were to require an energy resolution of $\Delta\omega \sim 0.02$. On the other hand, our resolution in energy is limited by finite-size effects to about $\sim 2\pi/L$, implying that for the treatable system sizes the two
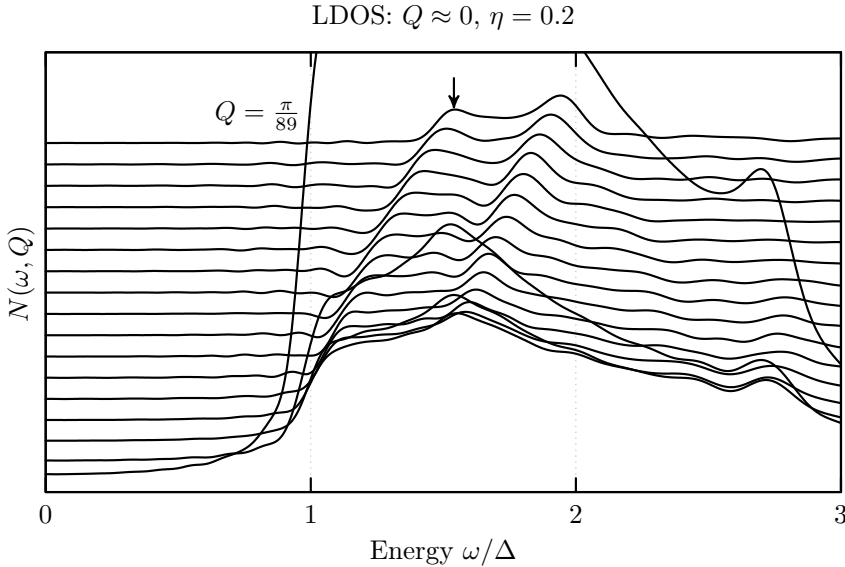
Figure 3.5: $N(\omega, Q)$ *for an extended Hubbard model with interaction $U = 8$, $V = 3$, $L = 88$, $\eta = 0.2$ and momenta $Q = \pi/89, 2\pi/89, \ldots, 17\pi/89$ (from bottom to top). The results are qualitatively similar to the ones for the standard Hubbard model shown in Fig. 3.1, ie, we observe a Mott gap Δ, a dispersing feature following* (3.29) *(indicated by the arrow) and another one at higher energies.*

linearly dispersing features cannot be separated. However, in order to resolve the peak splitting, running a correction vector based approach for large systems would be the method of choice.

To summarise our results, in Fig. 3.4 we show a contour plot of the LDOS. For comparison we plot the holon dispersion (3.29) around $Q = 0$ and $Q = 2k_F$ as well as the spinon dispersion (3.30) around $Q = 2k_F$, for which we used the parameters Δ, v_c and v_s obtained from the Bethe ansatz for the bulk system. In particular, we stress that there is no fitting parameter. In conclusion, our results are in very good agreement with the features of the LDOS predicted by the field-theoretical investigations.

3.4.2 Extended Hubbard model at half-filling

We have performed the analysis presented in the previous section for the extended Hubbard model (3.2) at half-filling and $L = 88$ lattice sites. Since the extended Hubbard model is not integrable, there exist no analytical results for the parameters Δ, v_c and v_s. Still, the field theory is expected to qualitatively describe the behaviour of the system in the low-energy limit. We note in passing that the next-nearest-neighbour
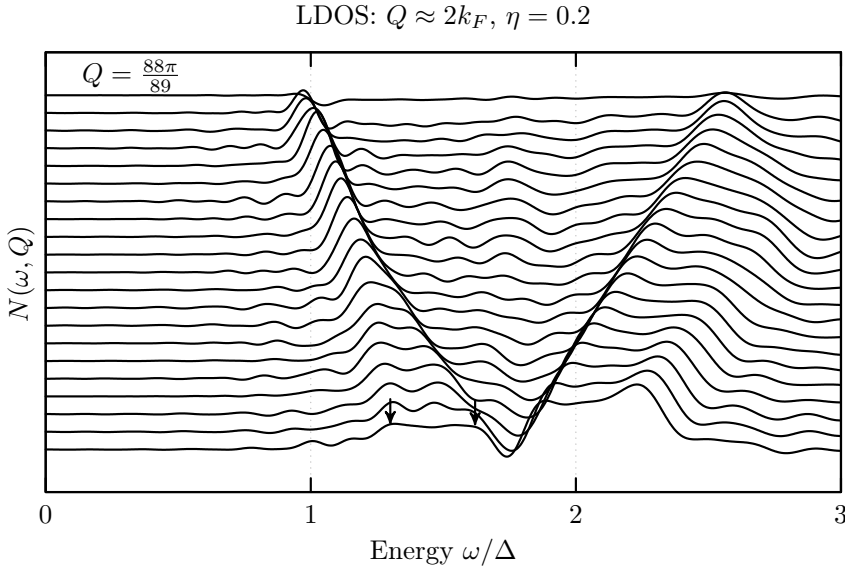
Figure 3.6: $N(\omega, 2k_F - q)$ *for an extended Hubbard model in the vicinity of $Q = 2k_F$ with $q = 2k_F - Q = \pi/89, 2\pi/89, \ldots, 21\pi/89$ (from top to bottom). All other parameters are as in Fig. 3.5. Similar to the standard Hubbard model, at low energies we observe two dispersing features at (3.29) and (3.30) respectively.*

interaction V can be used to tune the prefactor[150] $g_{1\perp} = U - 2V$ of the marginal operator perturbing the spin sector of the field theory, hence in principle allowing a systematic study of its effects. However, qualitative features, like the dispersions on which we focus here, will not be affected by the presence of the marginal operator, thus we will not analyse the dependence on V.

The LDOS for momenta in the vicinity of $Q = 0$ and $Q = 2k_F$ is shown in Figs. 3.5 and 3.6 respectively. In both plots we have renormalised the energy scale by the gap $\Delta \approx 2.1$ obtained from the data at $Q \approx 0$. At low energies the dispersing features are qualitatively identical to the ones seen for the standard Hubbard model, namely a propagating charge mode for $Q \approx 0$ and both a propagating charge and spin mode around $Q = 2k_F$. The only difference is that the charge and spin velocities take the values $v_c \simeq 1.8\Delta \simeq 3.8$ and $v_s \simeq 0.35\Delta \simeq 0.7$ respectively, which were determined by comparison with the quasiparticle dispersions (3.29) and (3.30). The energy gap Δ and charge velocity v_c for the two different momentum regimes agree well. We thus conclude that the low-energy sector is well described by the field theory. Furthermore, for small momenta we again observe a second charge mode which now seems to have the gap $\Delta_2 \simeq 1.5\,\Delta$.
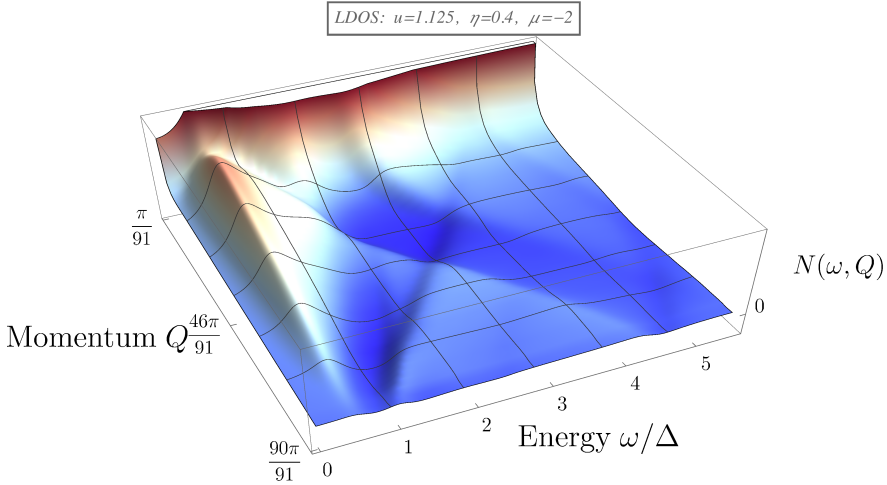
Figure 3.7: $N(\omega, Q)$ *for interaction* $u = 1.125$, *boundary potential* $\mu = -2$, $L = 90$ *lattice sites and broadening* $\eta = 0.4$. *Besides the peak at* $Q = 0$ *and the dispersing modes at* $\omega \geq \Delta$ *we observe a non-dispersing feature inside the energy gap at* $\omega = E_{bbs} \approx \Delta/2$ *which originates from the boundary bound state.*

3.5 Effect of a boundary potential

Having analysed the LDOS in the presence of open boundary conditions, we now turn to the investigation of the effect of a boundary chemical potential. Specifically we consider the Hubbard model (3.1) with a boundary potential at site $j = 0$,

$$H_{\mathrm{bp}} = H + \mu \sum_\sigma n_{j=0,\sigma}. \qquad (3.31)$$

Using bosonisation such a boundary potential is translated into non-trivial boundary conditions for the bosonic degrees of freedom. In particular, certain boundary conditions give rise to the existence of boundary bound states in the gapped charge sector[151–153] which manifest themselves[129, 156] in the LDOS as non-propagating features inside the Mott gap. The spectrum of the Hubbard chain with boundary potential (3.31) has been investigated by Bedürftig and Frahm[127] using the Bethe-ansatz solution. In particular it was found that a boundary bound state corresponding to a charge bound at the first site exists for $\mu < -1$. For even smaller boundary potentials, $\mu < -2u - \sqrt{1 + 4u^2}$, two electrons in a spin singlet get bound to the surface.

The Fourier transform of the LDOS in the presence of a boundary chemical poten-
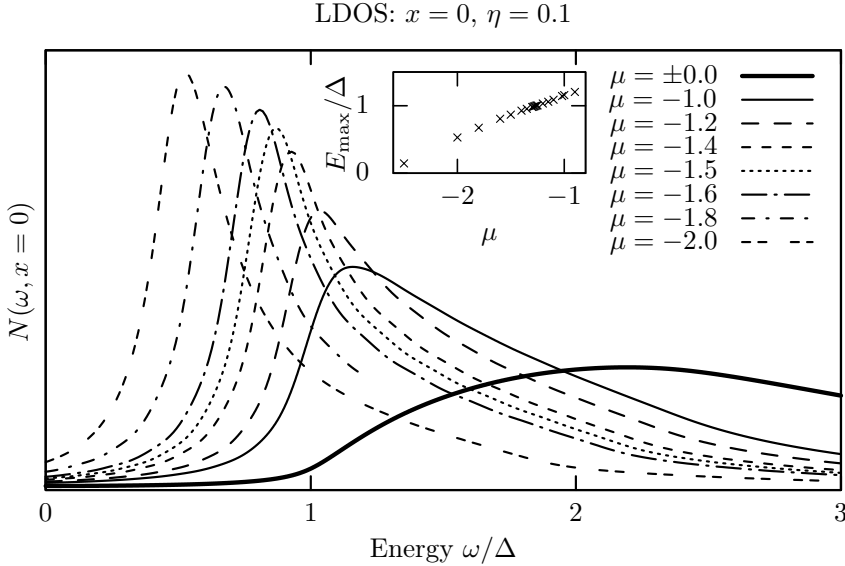
Figure 3.8: *LDOS at the boundary, $N(\omega, x = 0)$, for various values of μ and broadening $\eta = 0.1$. All other parameters are as in Fig. 3.7. In the absence of a boundary potential (thick line) there is barely any spectral weight inside the energy gap. For $\mu < -1$ the spectral density inside the gap grows continuously but its maximum is still located above the gap. For $\mu \leq -1.4$ the maximum is located inside the Mott gap, providing a clear manifestation of the boundary bound state. Inset: Position E_{max} of the maximum of $N(\omega, x = 0)$ as a function of the boundary potential μ. We observe that a potential $\mu \leq -1.27$ is needed for $E_{max} < \Delta$.*

tial is shown in Fig. 3.7. Besides the peak at $Q = 0$ due to the pinned charge-density wave and several dispersing modes above the Mott gap, we observe a clear, non-dispersing maximum inside the gap at $\omega = E_{bbs} \approx \Delta/2$, which is a manifestation of the boundary bound state in the LDOS. In the following we analyse this contribution in more detail by considering the LDOS $N(\omega, x) = -1/\pi \, \text{Im} \, G^R(\omega, x)$ close to the boundary.

First we analyse the LDOS at the boundary site, $N(\omega, x = 0)$, which is shown in Fig. 3.8 for several values of the boundary potential μ using an artificial broadening $\eta = 0.1$. One can clearly see that the maximum of the LDOS is shifted towards lower energies for decreasing μ. For $\mu \leq -1$ we find a considerable spectral density inside the Mott gap Δ; for $\mu \lesssim -1.27$ the maximum of the LDOS is located inside the energy gap as well. From this we deduce that for $\mu \lesssim -1.27$ there exists a clear boundary bound state contribution to the LDOS. We attribute the deviation to the critical value $\mu = -1$ obtained from the Bethe ansatz[127] to the finite system-size as well as the artificial broadening η introduced in our numerical calculations. This is supported
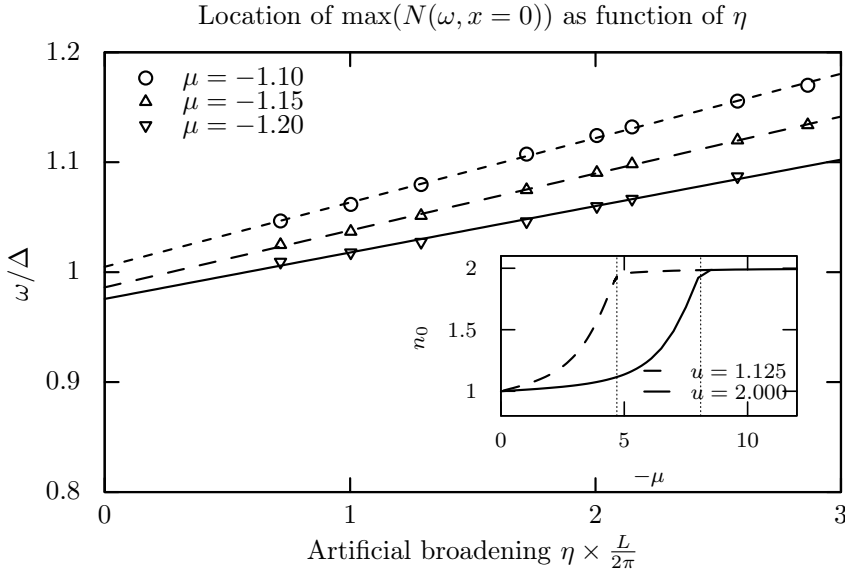
Figure 3.9: *Maximum of $N(\omega, x = 0)$ as a function of the artificial broadening η for $u = 1.125$ and $L = 90$. Extrapolating to $\eta = 0$ (indicated by lines) we find that that the energy of the maximum lies within the Mott gap for $\mu \lesssim -1.15$. Inset: Electron density n_0 at the boundary showing very good agreement with the Bethe-ansatz result.[127] The dotted vertical lines indicate the positions $\mu = -2u - \sqrt{1 + 4u^2}$ at which two electrons get bound to the boundary.*

by the dependence of the energy of the maximum in the LDOS on the broadening presented in Fig. 3.9, which shows that the energy of the maximum indeed decreases with decreasing η. Extrapolating the results to $\eta = 0$ and keeping in mind the finite system size as well as the fact that for $\mu \to -1^-$ the contributions from the boundary bound state and the standard continuum at $\omega \geq \Delta$ start to significantly overlap, we conclude that our results are consistent with the Bethe-ansatz solution. This is further supported by the electron density at the boundary shown in the inset of Fig. 3.9.

Finally we consider the space dependence of the LDOS when going away from the boundary. As is shown in Fig. 3.10, lowering the boundary potential leads to an increase of the LDOS at the boundary, consistent with the formation of a boundary bound state localised at $j = 0$. However, the system size and energy resolution is not sufficient to unveil an exponential space dependence of the LDOS as predicted by the field-theory analysis,[129, 156] ie, $N(\omega, x) \propto \exp[-2x\sqrt{\Delta^2 - E_{\mathrm{bbs}}^2}/v_{\mathrm{c}}]$.
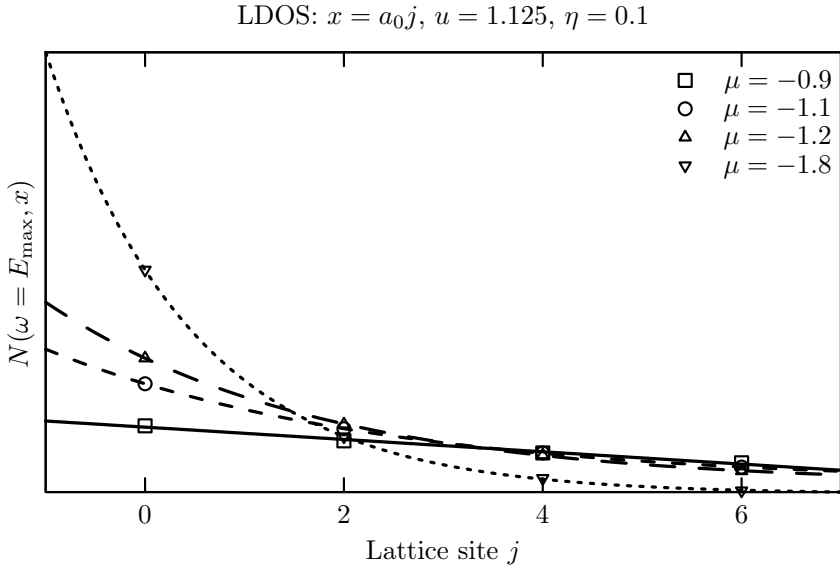
Figure 3.10: *Maximal value of the LDOS, $N(\omega = E_{max}, ja_0)$, as a function of the distance to the boundary for $u = 1.125$, $\eta = 0.1$ and $L = 90$. For decreasing μ we observe that the spectral weight gets more and more localised at the boundary.*

3.6 Conclusion

In this work we have performed a numerical study of the LDOS of one-dimensional Mott insulators with an open boundary. As microscopic realisations of the Mott insulator we have studied the (extended) Hubbard model at half filling. The results for the Fourier transform of the LDOS revealed the existence of the Mott gap as well as several gapped and gapless dispersing modes. These qualitative features were in perfect agreement with the results of field-theoretical calculations[129, 156] of the LDOS in the Mott insulator. Furthermore, we extracted quantitative values for the gap and velocities, which, in the case of the integrable Hubbard chain, were found to be in excellent agreement with the exact results.[31] Besides open boundary conditions we have also considered the effect of a boundary potential. For sufficiently strong potentials this results in the formation of a boundary bound state, which manifests itself in the LDOS as a non-dispersing feature inside the Mott gap. In summary, our results show that spin-charge separation and the formation of boundary bound states can be clearly observed in the Fourier transform of the LDOS amenable to numerical simulations or scanning tunneling spectroscopy experiments even for rather short systems.

Chapter 4

4 Finite-time Quenches in the XXZ Heisenberg Chain

In this chapter, we discuss the modification to the light cone of correlation spreading in the XXZ Heisenberg chain after interaction quenches of finite duration τ in comparison to sudden quenches.[1] For this, we perform the time evolution of the XXZ chain for short and intermediate times after the quench using time-dependent DMRG and compute the equal-time spin-spin correlation functions.

The chapter is organized as follows: In Sec. 4.2, we introduce the microscopic model, our numerical method and the details of the quench protocol. Sec. 4.3 discusses previous analytic results for the correlation functions after a quench in the Tomonaga-Luttinger model. In Sec. 4.4, we present our numerical results for the correlation functions and contrast them with the analytic expressions for the Tomonaga-Luttinger model.

4.1 Introduction

In the past twenty years the control of experimentalists over ultracold atomic systems in optical lattices has reached a degree, at which the realization of sudden quantum quench protocols has become feasible [18, 22, 23, 160]. In such a quench protocol, a quantum system is prepared in an initial state, often the ground state of an initial Hamiltonian H_0, while the time evolution for all times $t > 0$ is is carried out under another Hamiltonian H, for which the initial quantum state is not an eigenstate [161]. The overlaps between the initial quantum state and the eigenstates of H are, in general, rather non-trivial, which in turn causes a complex transient behavior of observables in response to the quench.

The aforementioned exciting new experimental possibilities have lead to a large body of theoretical work on the quench dynamics in a variety of systems, partic-

---

[1]Additional results, beyond the ones presented in this chapter, can be found in: B. Schoenauer and D. Schuricht, *Finite-time quantum quenches in the XXZ Heisenberg chain*, arXiv:1905:02678

ularly one-dimensional systems, where multiple powerful numerical and analytical tools are available as benchmark [56–58, 162–164].

In this work, we address the quench dynamics of the XXZ Heisenberg chain [27, 28]. It represents the most simple model of interacting spins and has been realized experimentally with ultracold atomic gases in optical lattices [59] and circular Rydberg atoms [60]. Previous theoretical work on the non-equilibrium dynamics of the XXZ Heisenberg chain has mostly focused on the properties of the non-equilibrium stationary state at long times after the quench. [61, 62, 165–167]. By virtue of the integrability of the XXZ Heisenberg chain, it is assumed that the expectation values in its stationary state after a quench can be calculated from a generalized Gibbs ensemble as opposed to the thermal Gibbs ensemble.

Unlike the majority of previous work, which has mainly employed sudden quantum quench protocols [161, 165, 170], we here consider more general quenches of finite duration τ, during which the interaction in the system is modified. Alongside the finite quench duration τ appears an additional energy scale $\sim \tau^{-1}$ in the system, which is directly related to the quench protocol and therefore tunable. As such, it can be chosen to be of similar size as other energy scales of the system, including the band width, excitation gaps or relaxation rates. The interplay of the additional energy scale with the established ones may then bring about emergent quantum states beyond the ones accessible through sudden quench protocols.

In the only previous analysis of finite time quenches in interacting microscopic models, Pollmann et al. [168] simulated a linear ramp of the anisotropic interaction of the XXZ Heisenberg chain and compared the resulting values for system heating and spin fluctuations to results from a linear quench of the Tomonaga-Luttinger model. They found the Tomonaga-Luttinger model to give an adequate prediction of said observables even in this non-equilibrium situation.

Subsequently, Chudzinski and Schuricht [169] considered several different finite time quench protocols of a Tomonaga-Luttinger and were able to obtain analytic solutions to the resulting differential equations. Their analysis finds a finite delay in the light cone of correlation spreading through the system as response to the finite duration of the quenches.

In this work, we study the same finite time quench protocols for interaction quenches of the XXZ Heisenberg chain in the critical regime. We then contrast our results for the position of the light cone front of correlation spreading with the correlation functions for the Tomonaga-Luttinger model after a quench.

4.2 Model and Setup

The Hamiltonian of the XXZ Heisenberg chain reads

$$H(t) = J \left[\sum_i S_i^x S_{i-1}^x + S_i^y S_{i-1}^y + \Delta(t) S_i^z S_{i-1}^z \right] , \tag{4.1}$$

where S_i^j denotes the spin operators in direction j on lattice site i. The time-dependent exchange anisotropy Δ can be mapped via a Jordan-Wigner transformation onto a nearest neighbor interaction between spinless fermions, hence the name interaction quench.

The equilibrium properties of the model are well known [27, 36]. For $|\Delta| < 1$, the system is quantum critical, whereas for $|\Delta| > 1$ the ground state is antiferromagnetically ordered and the excitation energies are gapped.

A way to prepare the system in a non-equilibrium state is by means of a quantum quench. In a typical interaction quench, the system is prepared at $t = 0$ in the ground state of the Hamiltonian H_0 with initial anisotropy Δ_i, typically $\Delta_i = 0$. Subsequently, the anisotropy is suddenly switched and the time evolution is performed with a Hamiltonian featuring a different anisotropy $\Delta_f \neq \Delta_i$. In the quench protocol that we study here, the change in the anisotropy is not sudden but continuous and extends over a finite duration τ. In particular, we numerically simulate two types of continuous switching, a linear and an exponential ramp, both of which have been previously studied analytically for the Tomonaga Luttinger model (TLM) in [169]. The linear quench is implemented as

$$\Delta(t) = \begin{cases} \Delta \frac{t}{\tau} & t < \tau \\ \Delta & t \geq \tau \end{cases} , \tag{4.2}$$

and the exponential quench as

$$\Delta(t) = \begin{cases} \Delta \left[\exp(\log(2)t/\tau) - 1 \right] & t < \tau \\ \Delta & t \geq \tau \end{cases} . \tag{4.3}$$

In the following, we present a numerical study of the quench dynamics and compare our results to analytical expressions for the correlation functions of the TLM as well as previous numerical results for sudden quenches in the XXZ Heisenberg chain [170].

For our numerical study, we employ a time-dependent density-matrix renormalization group (tDMRG) algorithm. Unlike many other tDMRG algorithms, we use a Krylov subspace method [179] to calculate to full matrix exponential of the Hamiltonian for the time evolution giving us the possibility to choose time steps of arbitrary size Δt while the Hamiltonian is time-independent. In a first DMRG step, we have calculated the ground state of a chain of length $L = 80$ sites with periodic boundary conditions. A calculation of the ground state energy density for $\Delta = 0$ finds $E_0/(JL) = -0.318378704$, which constitutes a deviation from the exact value $E_0/(JL) = -1/\pi$ by $\Delta E_0/(JL) = 7 \cdot 10^{-6}$ indicating that finite size effects are sufficiently small at this system size.

Starting from the ground state, we perform the first part of time evolution over the quench duration τ where we choose a small step size $\Delta t \approx J\tau/80$. For this particular time evolution, we use time-independent snapshots of the Hamiltonian $H(t_i < t < t_{i+1}) \simeq H(t_i)$. Additional calculations with smaller step sizes have been

performed finding identical results, thus confirming that the chosen step size is suffi-
ciently small to capture the details of the ramping function. Alternatively, one could
employ a Magnus expansion [171] of the time-dependent Hamiltonian, in which
case larger step sizes would be feasible. For the second part of the time evolution
after the quench, we use a larger constant step size $J\Delta t < 1$. An important aspect
of a global quantum quench is the linear growth of the entanglement entropy in re-
sponse to it. We therefore dynamically adjust the number of kept states per block
$1400 < N_{\mathrm{cut}} \leq 14000$ in each DMRG step to ensure that the maximum amount of
discarded entanglement entropy does not exceed $\delta S_{\mathrm{max}} = 10^{-4}$. The large number
of kept states is also necessitated by the criticality of the system, due to which the
entanglement entropy grows as a logarithm of the system size L.

Within the tdDMRG algorithm, we measure the time-dependent expectation values
of the equal-time transverse and longitudinal correlation functions of the spin oper-
ators at a distance ℓ. The transverse two-point function reads

$$C_t(\ell, t) = \left\langle S_i^x(t) S_{i+\ell}^x(t) \right\rangle = \frac{1}{4} \left(\left\langle S_i^+(t) S_{i+\ell}^-(t) \right\rangle + \left\langle S_i^-(t) S_{i+\ell}^+(t) \right\rangle \right), \qquad (4.4)$$

and the longitudinal two-point function is

$$C_l(\ell, t) = \left\langle S_i^z(t) S_{i+\ell}^z(t) \right\rangle. \qquad (4.5)$$

We chose the lattice sites on which we measure the spin operators to be centered
around the middle of the chain, i.e. $i = L/2 - \ell/2$, to maximize the time during
which the two-point functions are unaffected by excitations entering through the
periodic boundary.

4.3 Correlation functions for the Tomonaga-Luttinger Model

In the low-energy regime, gapped one-dimensional fermionic systems can be mapped
onto a field theory of the form

$$H_{TL} = \frac{v_F}{i} \int dx \left[\psi_+(x) \partial_x \psi_+(x) - \psi_-(x) \partial_x \psi_-(x) \right] \qquad (4.6)$$
$$+ \int dx\, dx' \left[g_4(x - x') \rho_\pm(x) \rho_\pm(x') + g_2(x - x') \rho_\pm(x) \rho_\mp(x') \right]$$

where $\psi_\pm$ denote chiral fermion fields moving in either right $(+)$ or left $(-)$ direction,
$\rho_\pm$ the chiral fermion densities, and the parameters v_F, $g_2(x - x')$ and $g_4(x - x')$ are
specific to the microscopic model system. For the equilibrium, it is well known that
this Hamiltonian can be diagonalized by introducing bosonic operators that create
or annihilate collective excitations in the system [32, 36]. The effective bosonic theory
then reads

$$H_{LL} = \frac{\tilde{v}}{2\pi} \int dx \left[K \left(\partial_x \theta(x) \right)^2 - \frac{1}{K} \left(\partial_x \phi(x) \right)^2 \right], \qquad (4.7)$$
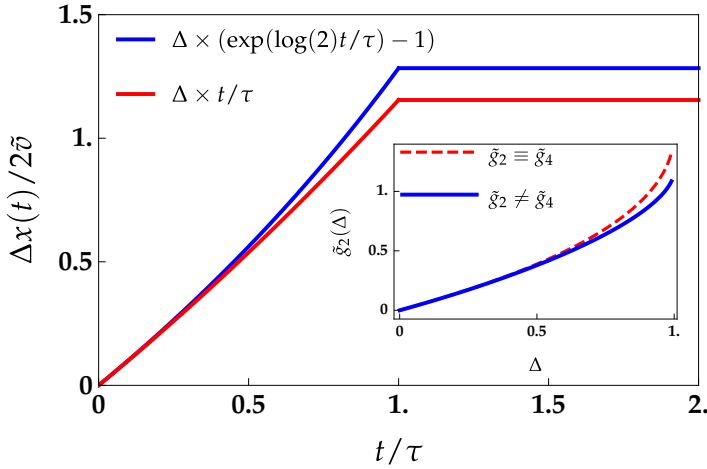
Figure 4.1: *Time-dependent delay $\Delta x(t)$ of the light-cone front of correlation spreading after an interaction quench of finite duration $J\tau = 1$ in the Tomonaga Luttinger model. We show the delay for a linear quench (red) and an exponential quench (blue) protocol. Inset: Interaction strength $\tilde{g}_2(q = 0)$ of the Tomonaga Luttinger model, which describes the low energy regime of the XXZ Heisenberg chain, as a function of the anisotropy Δ. The blue line indicates the actual value $\tilde{g}_2(0)$ as the solution to the set of equation (8)-(11). The dashed red line shows $\tilde{g}_2(0)$, if we impose Galilean invariance $\tilde{g}_2(q) \equiv \tilde{g}_4(q)$. In this case, the value of $\tilde{g}_2(0)$ is given by (4.12).*

where φ denotes a canonical boson field and θ its dual field. The details of the original system are now encoded in the Luttinger parameters $\tilde{v}$ and K. The connection between the free boson theory and the interacting fermionic theory is made via

$$\tilde{v} = v_F \sqrt{(1 + \tilde{g}_4(0))^2 - \tilde{g}_2(0)^2}\,, \tag{4.8}$$

$$K = \sqrt{\frac{1 + \tilde{g}_4(0) - \tilde{g}_2(0)}{1 + \tilde{g}_4(0) + \tilde{g}_2(0)}}\,. \tag{4.9}$$

where we have replaced $g_{2,4}(q)/(2\pi v_F) \to \tilde{g}_{2,4}(0)$, since the momentum dependence of the interaction in equilibrium is known to be irrelevant in the RG sense. The XXZ Heisenberg chain can also be mapped onto a fermionic lattice model containing spinless fermions with nearest neighbor interaction by means of a Jordan-Wigner transformation. As such, it is likewise described by a free boson theory with a specific set of Luttinger parameters. The XXZ Heisenberg chain can furthermore be solved exactly by Bethe ansatz and analytical expression for the Luttinger param-

eters are known. These expressions read

$$\tilde{v} = \frac{\pi}{2} \frac{\sqrt{1 - \Delta^2}}{\arccos \Delta} , \tag{4.10}$$

$$K = \frac{\pi}{2} \frac{1}{\pi - \arccos \Delta} . \tag{4.11}$$

Through equations 4.9 and 4.11 we can determine the parameters $\tilde{g}_2(0)$ and $\tilde{g}_4(0)$ of the fermionic field theory that corresponds to our microscopic system at each point in time. The analytical results for the quench dynamics after finite-time quenches in the TLM by Chudzinski and Schuricht depend on Galilean invariance, ie $\tilde{g}_2(0) = \tilde{g}_4(0)$. In the inset of figure 4.1, we plot the interaction strength $\tilde{g}_2$ as a function of the anisotropy of the XXZ chain with and without the assumption of Galilean invariance. We find that for $\Delta \leq 0.8$, Galilean invariance is realized to a good approximation in the XXZ chain and a comparison of our numerical results and the analytical results for a Galilean invariant TLM should be feasible. The time-dependent interaction strength $\tilde{g}_2$ of the TLM corresponding to this specific XXZ chain is then given by

$$\tilde{g}_2(t) = \frac{3\pi^2 - 8\pi \arccos \Delta(t) + 4 \arccos^2 \Delta(t)}{2\pi^2} . \tag{4.12}$$

4.3.1 Correlation functions for a Tomonaga-Luttinger Model after a Quench

Previous work by Cazalilla [63] has looked into the two-point functions of a Tomonaga-Luttinger model after a sudden interaction quench $\Delta = 0 \to \Delta \neq 0$. In the thermodynamic limit the two-point function reduces to

$$\left\langle \psi_\alpha(x, t > 0) \psi_\alpha(0, t > 0) \right\rangle = \frac{i}{2\pi(x + ia)} \left| \frac{R_0}{x} \right|^{\gamma^2} \left| \frac{x^2 - (2\tilde{v}t)^2}{(2\tilde{v}t)^2} \right|^{\frac{\gamma^2}{2}} , \tag{4.13}$$

where a denotes the lattice spacing, R_0 the order of magnitude of the range of interactions and γ encodes the details of the Bogoliubov transformation. Similarly, the density-density correlator reads

$$\left\langle J_\alpha(x, t > 0) J_\alpha(x, t > 0) \right\rangle = -\frac{1}{4\pi} \left[\frac{1 + \gamma^2}{|x|^2} - \frac{\gamma^2}{2|x - 2\tilde{v}t|^2} - \frac{\gamma^2}{2|x + 2\tilde{v}t|^2} \right] . \tag{4.14}$$

In terms of spin operators, the two-point functions for the XXZ Heisenberg chain become [170]

$$\left\langle S_i^x(t) S_{i+\ell}^x(t) \right\rangle \simeq (-1)^n \frac{A^x}{\sqrt{\ell}} \left| \frac{1}{(2\tilde{v}t)^2} \frac{\ell^2 - (2\tilde{v}t)^2}{\ell^2} \right|^{\frac{1}{8}\left(\frac{1}{K^2} - 1\right)} , \tag{4.15}$$

$$\left\langle S_i^z(t)S_{i+\ell}^z(t)\right\rangle \simeq B^z\left\{-\frac{1-K^2}{8\pi^2}\left[\frac{1}{(\ell+2\tilde{v}t)^2}+\frac{1}{(\ell-2\tilde{v}t)^2}-\frac{1+K^2}{4\pi^2}\frac{1}{\ell^2}\right]\right\} \quad (4.16)$$

$$+A^z\frac{(-1)^\ell}{\ell^2}\left|\frac{1}{(2\tilde{v}t)^2}\frac{\ell^2-(2\tilde{v}t)^2}{\ell^2}\right|^{\left(\frac{K^2-1}{2}\right)},$$

where analytical expressions for the coefficients A^x, A^z and B^z are thus far only known in equilibrium [172].

The spin-spin correlation functions reflect the light cone picture put forward by Calabrese and Cardy [173]. The quench excites quasi-particles, which are quantum entangled if they are excited within a distance $r \leq \xi$ from each other, where ξ is the correlation length of the system. These quasi-particles propagate semi-classically through the system at a speed v and induce correlations between two points x_i and x_j at time t if $|x_i - x_j| = 2vt$. This constitutes a light cone of correlation spreading in spacetime. Said light cones have been observed in numerical simulations of the Bose-Hubbard model [64] and experimentally in ultracold atomic gases [65].

For quenches of finite duration, we expect the excitation of quasi-particles to occur continuously during the quench in contrast to a sudden quench, where all excitations take place at $t = 0$. Furthermore, the renormalized velocity $\tilde{v}$ of the instantenous system at time $t < \tau$ is in general smaller than the the renormalized velocity of the post-quench system. The maximum velocity that quasi-particles can propagate at is thus smaller, if they are excited early in the quench and only matches that of quasi-particles from a sudden quench, if they are excited late in the quench. In that case they are delayed by $\Delta t \simeq \tau$ as compared to excitations from a sudden quench. This mismatch of velocities will result in a deformed light cone during the finite duration quench, $t \leq \tau$, and a delay of the light cone front after the quench, for $t > \tau$. We thus expect the spin-spin correlation function to acquire the shape

$$\left\langle S_i^x(t)S_{i+\ell}^x(t)\right\rangle \simeq (-1)^\ell\frac{A^x}{\sqrt{\ell}}\left|\frac{1}{(2\tilde{v}t-\Delta x)^2}\frac{\ell^2-(2\tilde{v}t-\Delta x)^2}{\ell^2}\right|^{\frac{1}{8}\left(\frac{1}{K^2}-1\right)}, \quad (4.17)$$

where Δx describes the delay of the light cone front due to the finite quench duration. Chudzinski and Schuricht recently obtained an expression for this delay Δx in the Galilean invariant Tomonaga-Luttinger model [169]. For this model, they were also able to analytically determine the time-dependent Bogoliubov coefficients $u_n(t)$ and $v_n(t)$ for a set of common quench protocols. For the delay of the light cone front, they identified

$$\Delta x = v_F\tau\left(\frac{4K}{1-K^2}\right)\left[g_2(q,\tau)-\frac{1}{\tau}\int_0^\tau dt\, g_2(q,t)\right], \quad (4.18)$$

which holds for arbitrary quench protocols but is limited to quench durations

$$\tau \leq \frac{10}{v_F q_c} \simeq \pi. \quad (4.19)$$

In figure 4.1, we plot the light-cone delay Δx as a function of time for a linear and an exponential quench, $\Delta(t = 0) = 0 \rightarrow \Delta(t = \tau) = 0.2$, of duration $J\tau = 1.0$. We observe that an exponential quench leads to a increased delay Δx as compared to the linear quench.

4.4 Numerical Results for Quenches inside the Critical Regime

We have quenched the XXZ chain from the initial non-interacting model, $\Delta(t = 0) = 0$, to one of two final interaction strengths, $\Delta(\tau) = 0.2$ or $\Delta(\tau) = 0.5$. From the inset of figure 4.1 we see that Galilean invarince is approximately satisfied for both these final values. For the quench durations, we have chosen $J\tau = 0.2$, $J\tau = 1.0$ and $J\tau = 4.0 > \pi$. A first set of calculations was performed using $\tau = 0$ to compare our approach to previous results for sudden quenches obtained with iTEBD [170].

In figure 4.2, we plot the time-dependent correlation functions $C_t(\ell, t)$ and $C_l(\ell, t)$ at distance $\ell = 10$ for the two respective quench protocols and four quench durations with $\Delta(\tau) = 0.2$. In fig. 4.2 (a), we plot the transverse correlation function $\langle S_i^x(\tilde{v}t)S_{i+\ell}^x(\tilde{v}t)\rangle$ for a linear quench and the corresponding theoretical predictions from the Tomonaga Luttinger model (4.17). We fit the value $A^x = 0.140 \pm 0.005$ solely for the sudden quench ($\tau = 0$).
We find that the onset of correlations for $\tilde{v}t > \ell/2$ is clearly visible in all our numerical results. Using the fitted value A^x from the sudden quench for the correlation functions (4.17) of the Tomonaga-Luttinger model after a linear ramp, we find our numerical results for the correlation function to be in good agreement with the predictions for $\tau < \pi$ with regard to the delay of the light cone front Δx and to still agree reasonably well for $\tau > \pi$. Our results for the sudden quench are furthermore in excellent agreement with previous results from iTEBD.
In fig. 4.2 (b), we display the transverse correlation function $C_t(10, t)$ for the XXZ chain and for the Tomonaga-Luttinger model after an exponential quench. Again using the previously fitted value of A^x we once more find very good agreement between our tDMRG results and the analytic expression for the correlation function for the TL model. Our results also reflect the increased delay of the light cone front compared to a linear quench as shown in fig. 4.1.
Fig. 4.2 (c), shows the longitudinal correlation function $\langle S_i^z(\tilde{v}t)S_{i+10}^z(\tilde{v}t)\rangle$ after a linear ramp. For the quench durations $J\tau = 0$, $J\tau = 0.2$, and $J\tau = 1.0$, we find that the inflection point of the correlation function is reasonably well situated at the position of the light cone front. For $J\tau = 4.0$ this is clearly not the case, indicating that the relation for the delay of the light cone is indeed no longer valid for $J\tau > \pi$.
In fig. 4.2 (d), we plot the tDMRG data for transverse correlation function $C_t(10, t)$ in response to a linear ramp to $\Delta(\tau) = 0.5$ and the corresponding correlators for the TL model. For the sudden quench, we fit a value $A^x = 0.129 \pm 0.002$ and use this value for the correlation functions of the TL model describing the quenches of finite duration. Once again we observe very good agreement between the correla-

tions functions for the quenches of duration $J\tau \leq 1.0$. For $J\tau = 4.0$ on the other hand the agreement is not quite as good.

In figure 4.3, we plot the rescaled transverse correlation function $C_t(\ell, t)$ at distances $\ell = 2, 4, \dots, 16$, where the rescaled time has shifted by the delay Δx of the fastest quasi-particle excitations. For a sudden quench, where $\Delta x = 0$, these rescaled correlation functions collapse upon each other. For finite duration quenches, we observe a less well established collapse with larger deviations for shorter distances $\ell \leq 10$. At short distances correlations are induced by quasi-particles propagating at velocities $v < \tilde{v}$, before correlations can be induced by quasi-particles excitations propagating with velocity $v = \tilde{v}$. At larger distances the quasi-particles propagating at smaller velocities are overtaken by the quasi-particles propagating at $v = \tilde{v}$. We observe that at large distances, the correlation functions indeed collapse on the analytical result of the TL model, which is shown as the dashed black line.

Figure 4.4 displays contour plots of the transverse and longitudinal correlation functions of the XXZ chain after linear quenches of duration $J\tau = 1$ and $J\tau = 4$. The dashed white line indicates the position of the light cone front as expected after a sudden quench. The solid white line marks the position one would expect for the respective finite duration quench based on the analytical results for the TL model. In fig. 4.4 (a), we observe that the dashed white line, representing the sudden quench light cone position, is significantly ahead of the minimum of the rescaled transverse correlation function $\langle S_i^x(\tilde{v}t) S_{i+\ell}^x(\tilde{v}t) \rangle \times \ell^{\alpha+1/2}$. In fig. 4.2 we have seen as well that for $\ell = 10$ and $J\tau = 1$, the TL model correlation functions agreed well with the results for the microscopic model.

In fig. 4.4 (a), we find the distance between the solid white line, indicating the position of the light cone front and the minimum of our numerical data to be consistent with our previous findings for $\ell = 10$. For the longitudinal correlation function after a linear quench of duration $J\tau = 1$, shown in fig 4.4 (b), we again find the numerical results for the XXZ chain and the analytical result for the TL model to match well. This is shown in detail for $\ell = 10$ in fig. 4.2 (c). Fig. 4.4 (c) depicts the contour plot of the transverse correlation function for a linear quench of duration $J\tau = 4$. We notice that the estimated delay Δx is for the most part larger than the effective delay we observe in the numerical results for the XXZ chain. The relation (4.18) thus appears indeed not to be valid for quenches of duration $J\tau \geq \pi$. This situation is even more clearly noticeable in fig. 4.4 (d), where we plot the longitudinal correlation function for quench duration $J\tau = 4$. The maximum and thus the inflection point consistently occurs before a light cone $x = (2\tilde{v}t - \Delta x)$ would connect two points at the respective distances ℓ.

4.5 Conclusion

In this work, we have studied the time evolution of the XXZ Heisenberg chain for interaction quenches of finite duration τ. The finite duration quenches were performed in the critical regime, starting at $\Delta(t = 0) = 0$ and increasing the anisotropy either linearly or exponentially up to a final value, $1 > \Delta(t = \tau) > 0$. We used a
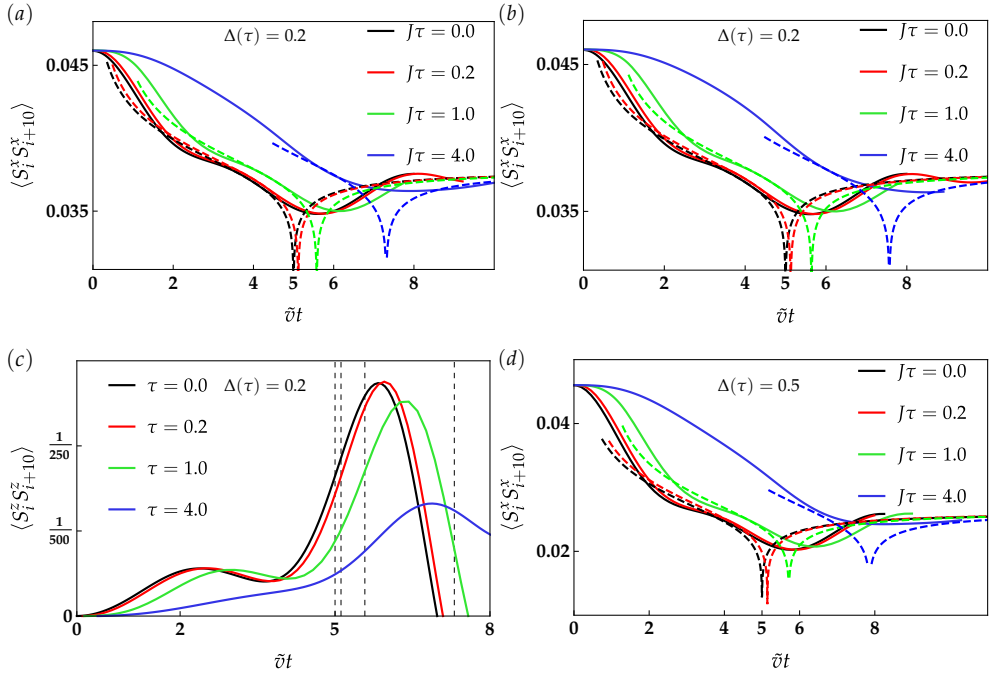
Figure 4.2: *Equal time spin-spin correlation functions at distance $\ell = 10$ for quenches of various durations τ. We show both linear and exponential quench protocols. (a) Transverse correlation function for a sudden quench (black) and three linear quenches of duration $J\tau = 0.2$, $J\tau = 1$ and $J\tau = 4$ with $\Delta(\tau) = 0.2$. As dashed lines, we plot the the correlation functions for the Tomonaga-Luttinger model after a quench with the predictions for the light cone front delay Δx from (4.18). (b) Transverse correlation function for a sudden quench (black) and three exponential quenches of duration $J\tau = 0.2$, $J\tau = 1$ and $J\tau = 4$ with $\Delta(\tau) = 0.2$. For the correlation functions of the TL (dashed lines), we use the same fitted value A^x as in (a).(c) Longitudinal correlation function for a sudden quench (black) and three linear quenches of duration $J\tau = 0.2$, $J\tau = 1$ and $J\tau = 4$ with $\Delta(\tau) = 0.2$. As dashed lines we plot, the expected position of the light cone front. (d) Transverse correlation function for a sudden quench (black) and three linear quenches of duration $J\tau = 0.2$, $J\tau = 1$ and $J\tau = 4$ with $\Delta(\tau) = 0.5$. As dashed lines, we again plot the the correlation functions for the Tomonaga-Luttinger model with the predictions for the light cone front delay Δx from (4.18).*
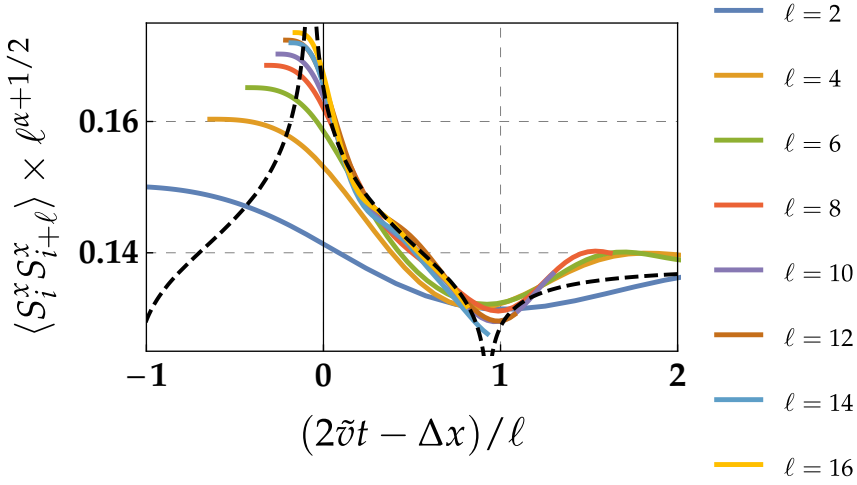
Figure 4.3: *Rescaled transverse correlation function for a linear quench of duration $J\tau = 1$ and a final anisotropy $\Delta(\tau) = 0.2$ for various distances ℓ. Unlike the sudden quench situation, the correlation do not all collapse on a single curve especially at shorter distances ℓ. This is because correlations are induced at shorter distances by quasi-particles moving at smaller velocities before the sites are connected by quasi-particles propagating at velocity $\tilde{v}$. The dashed black line indicates the correlation function for the Tomonaga Luttinger model given by (4.17) at $\ell = 16$. At larger distances, we observe a good agreement between our numerical results and the correlation function for the TL model after a quench.*

time-dependent density matrix renormalization algorithm to calculate the transverse and longitudinal equal-time spin-spin correlation functions at a distance ℓ. Our results show a light-cone like feature consistent with the quasi-particle picture put forward by Calabrese and Cardy [173]. Unlike the light cone resulting from a sudden quench, the light cone front after finite-time quenches features a delay Δx. We have compared this delay with analytical results for the light cone front delay calculated for the Tomonaga Luttinger model [169], which is known to describe the low-energy equilibrium properties of the XXZ Heisenberg model. We find good agreement between the delay in numerical results for the XXZ chain and the results for the TL model at short and intermediate quench durations. For longer quench durations, we see that the TL model predictions become less accurate. We conclude that, despite the non-equilibrium nature of the quantum quench, the Tomonaga-Luttinger model can still adequately describe certain behavior of this particular microscopic model.
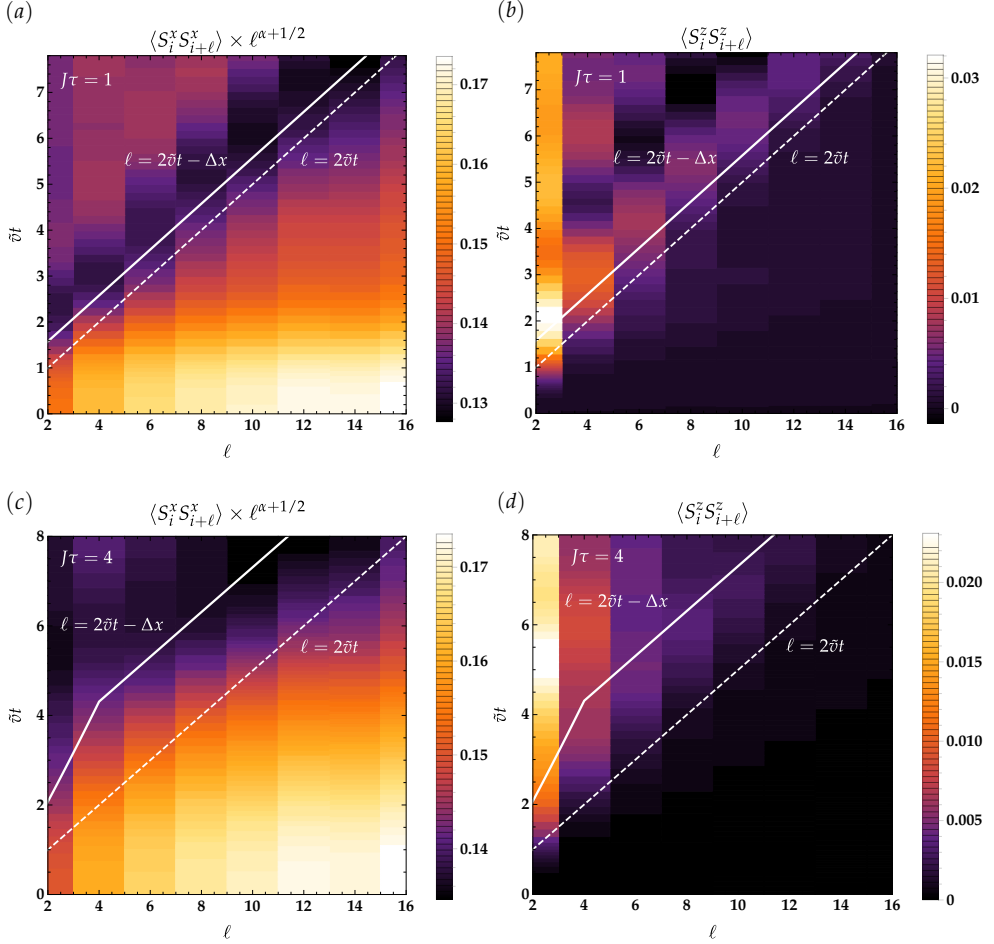
Figure 4.4: *Time-dependent transverse and longitudinal correlation functions direction after two linear ramps of duration $J\tau = 1$ and $J\tau = 4$ with $\Delta(t = 0) = 0 \rightarrow \Delta(t = \tau) = 0.2$. The dashed white lines indicate the light cone position after a sudden quench as has been observed by Collura et al. [170]. The solid white lines highlights the expected light-cone front after a linear quench of respective duration τ. (a) Rescaled transverse correlation function for $J\tau = 1$. (b) Longitudinal correlation function for $J\tau = 1$. (c) Rescaled transverse correlation function for $J\tau = 4$. (d) Longitudinal correlation function for $J\tau = 4$.*

Chapter 5

5 Long-lived circulating currents in strongly correlated Nanorings

In this chapter, we study the time evolving currents flowing in an interacting, ring-shaped nanostructure after a bias voltage has been switched on. The source-to-drain current exhibits the expected relaxation towards its quasi-static equilibrium value at a rate Γ_0 reflecting the lead-induced broadening of the ring states. In contrast, the current circulating within the ring decays with a different rate Γ, which is a rapidly decaying function of the interaction strength and thus can take values orders of magnitude below Γ_0. This implies the existence of a regime in which the nanostructure is far from equilibrium even though the transmitted current is already stationary.

The chapter is organized as follows: First, in Sec. 5.2, we introduce the model of the nanostructure. Subsequently, we present our tDMRG and perturbation theory results in Sec. 5.3 and Sec. 5.4, respectively. Lastly, we discuss a Schrieffer-Wolff transformation of the model system in Sec. 5.5 and experimental setups to observe the long-lived ring transients in Sec. 5.6.

5.1 Introduction

Isolated quantum systems, such as small molecules, feature a discrete set of energy levels. When brought to contact with two electrodes, a nano-junction can form and a current begins to flow. At weak coupling, the associated level broadening, Γ_0, is still small as compared to the typical energy spacing, ΔE, of the isolated system. One might perhaps suspect that these energies by themselves set the only relevant time scales. But in fact an prominent exception is known, the Kondo phenomenon [174], which occurs in a situation where ΔE is dominated by a strong on-site repulsion between the charge carriers. This suppresses charge fluctuations but allows for quantum-fluctuations of the spin, leading to an emergent energy scale, the Kondo

temperature T_K, which is parametrically small compared to the native scales Γ_0 and ΔE.

In this work, we report another example of an emergent energy scale, Γ; it manifests in the relaxation of circulating currents in mesoscopic nanostructures. Like the Kondo temperature, the new scale is a many-body phenomenon, originating from interactions between particles on the nanostructure. However, the manifestation of the new relaxation rate Γ requires the nanostructure to be brought out of equilibrium.

A sketch of the model system that exhibits the novel scale Γ is displayed in Fig. 5.1. Originally, similar ring-shaped devices served as a toy-models to study the interplay of interaction and interference [175, 176] and to explain quantum-interference effects in transport through functionalised graphene ribbons [177]. The ring geometry supports stationary circulating ("orbital") currents that can exceed the source-drain ("transport") current by orders of magnitude at Fermi-energies situated close to a Fano-resonance.

Strong circulating currents in ring-shaped devices, Fig. 5.1, generically arise as transients after a voltage quench. They then carry an oscillating amplitude with a frequency resembling the lowest lying excitation gap of the nanostructure. We here report results from time-dependent density matrix renomalisation group (td-DMRG) [66, 158, 178, 179] simulations showing that in situations where the interaction U is the dominating native scale of the nanoring, these oscillations can be very pronounced and very long-lived. They exhibit a lifetime Γ^{-1} that exceeds the transients in transport currents, Γ_0^{-1}, by orders of magnitude if the repulsive interaction U becomes strong. The computational finding is complemented with perturbative arguments that explain this effect and clarify the relevant physical processes. In essence, the strong suppression of Γ is due to a mirror symmetry of the nanoring which in turn leads to a cancellation of the leading-order processes and yields $\Gamma \sim U^{-6}$ at strong interactions. Possible experimental signatures of the effect proposed here are discussed.

5.2 Nanostructure

The model associated with Fig. 5.1 is represented by the Hamiltonian $H = H_r + H_l + H_c$ describing the ring, the leads and their mutual coupling, respectively. The ring Hamiltonian is given by

$$H_r = -J \sum_{\langle i,j \rangle} \left(d_i^\dagger d_j + d_j^\dagger d_i \right) + U \sum_{\langle i,j \rangle} \left(n_i n_j - \frac{n_i + n_j}{2} \right) + \varepsilon_T n_2, \qquad (5.1)$$

with operators $d_j^\dagger$ and d_j creating/annihilating spinless fermions at site j and $n_j = d_j^\dagger d_j$ denoting the corresponding density. The first term describes hopping of the fermions between nearest neighbours, while the second represents the repulsive nearest-neighbour interaction. The last term is an external potential at the top site which breaks the symmetry between the upper and lower path through the ring.
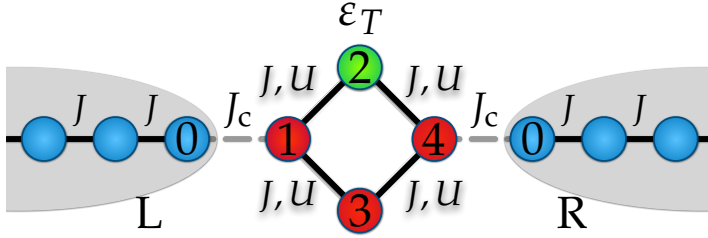
Figure 5.1: *Schematic representation of the nanostructure. The ring (red and green dots) is coupled by J_c to left and right leads (blue dots). Spinless fermions can hop within the ring and leads with amplitude J, the top site (site 2) on the ring is subject to the potential ε_T, and inside the ring a nearest-neighbour interaction U is present.*

The lead Hamiltonian reads

$$H_l = -J \sum_{\alpha=L,R} \sum_{n \geq 0} \left(c_{\alpha,n+1}^\dagger c_{\alpha,n} + c_{\alpha,n}^\dagger c_{\alpha,n+1} \right), \tag{5.2}$$

where $c_{n,\alpha}^\dagger$ and $c_{n,\alpha}$ create and annihilate a spinless fermion at site n in the lead α=L,R. For simplicity we assume the hopping parameter J in the ring and lead to be equal. Finally, the coupling between both subsystems is facilitated by

$$H_c = -J_c \left(d_1^\dagger c_{L,0} + c_{L,0}^\dagger d_1 + d_4^\dagger c_{R,0} + c_{R,0}^\dagger d_4 \right) \tag{5.3}$$

coupling the outer sites on the ring to the first sites of the leads.

In the following we analyse the non-equilibrium currents in the nanostructure by three different methods: (i) tdDMRG simulations, (ii) a reduced density-operator transport theory (RDTT) [180, 181], and (iii) mapping to an effective two-state nanostructure [182].

5.3 tdDMRG simulations

First, we study the time evolution after a voltage quench using the tdDMRG algorithm [183–189]. Specially we use the time evolution scheme outlined in Refs. [179, 189, 190] performing the evaluation of the time evolution via matrix exponentials within the framework of Krylov spaces. At times $t < 0$ the system is prepared in the ground state of the model with an additional charge excess induced by a stationary gating with $V/2(\sum_i n_{L,i} - \sum_i n_{R,i})$. At $t = 0$ the gate is switched off, so the electrodes begin to discharge and currents start to flow through the system. We simulate the time evolution with finite leads which are long enough to be able to study the transient regime all the way into the quasi-stationary, non-equilibrium limit. Finite-size
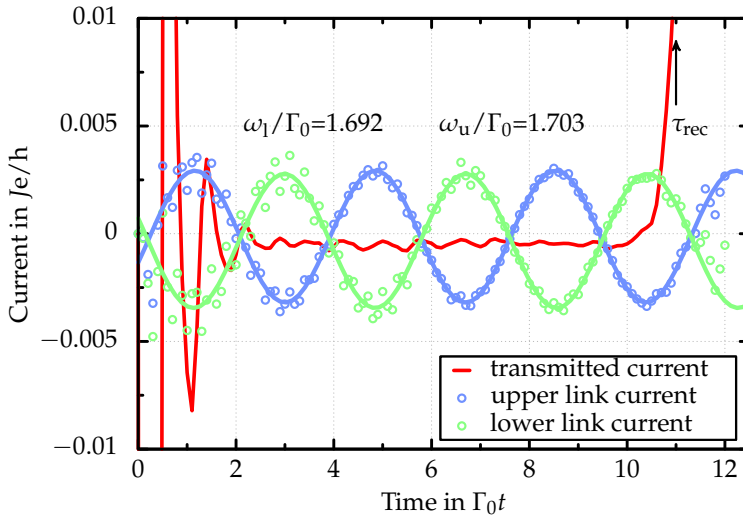
Figure 5.2: *Time evolution of the transmitted and ring currents, $\langle I_t \rangle(t)$ and $\langle I_r \rangle(t)$, evaluated using tdDMRG on the links $1 \rightarrow 2$ and $1 \rightarrow 3$ in Fig. 5.1. The recurrence time $\tau_{rec} = L/(2v_F) \simeq 44$ is indicated by the black arrow. While the transmitted current quickly relaxes to a stationary value, the ring currents show persistent oscillations with frequencies $\omega_{l,u}$ over the accessible times. The simulation parameters are $L = 96$, $U = 4J$, $\varepsilon_T = J/2$, $J_c = J/2$ and $eV = 0.4J$.*

effects will interfere only at times exceeding the recurrence time $\tau_{rec}=L/(2v_F)$, at which the electrons reach the boundary of the leads. (For details of the quenching protocol see Ref. [189].) Here L denotes the total number of sites, ie, the length of the leads is given by $(L-4)/2 \approx L/2$, and $v_F = 2J$ is the Fermi velocity of the lead electrons.

During the time evolution we determine the expectation values of the local currents $I_t \propto \mathrm{Im}(c_i^\dagger c_{i-1})$ and $I_r \propto \mathrm{Im}(d_k^\dagger d_l)$ flowing in the leads and the impurity, respectively, where l and k are neighbouring sites. The local current densities after quenching are displayed in Fig. 5.2. The transport ("transmitted") current I_t initially fluctuates in response to the quench for times $\Gamma_0 t \leq 3$, where we use $\Gamma_0 = 2\pi\rho(\varepsilon_F)J_c^2$ with the density of states in the leads $\rho(\varepsilon_F) = 1/(2\pi J)$ as our time unit. After this transient the transmitted current appears to have reached a largely time-independent steady state in line with predictions from non-equilibrium Green function formalism for the transient currents through interacting regions [191, 192].

In contrast, for the local currents in the ring I_r we observe a drastically different behaviour. Although some transient features decay quickly, the ring currents oscillate with a distinct frequency ω for long times. In fact, for sufficiently strong Coulomb repulsions U we do not observe a significant reduction of the oscillation amplitude within the observation times accessible to our simulations.
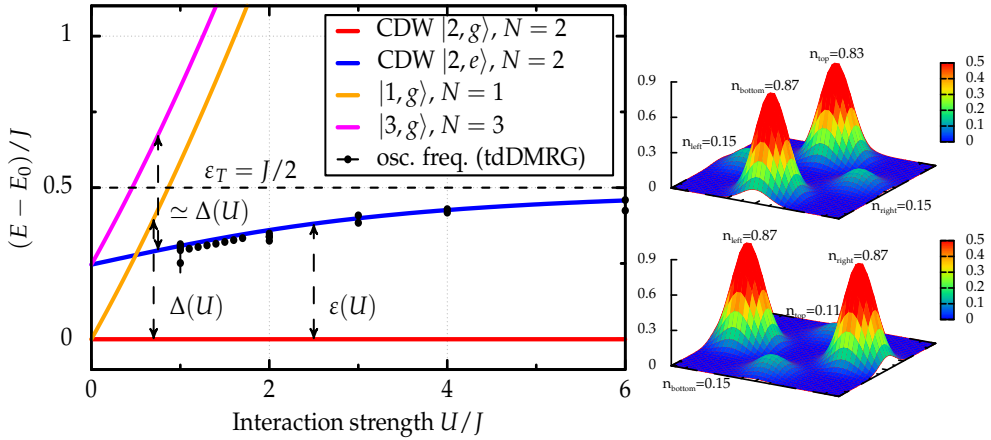
Figure 5.3: *Spectrum of the uncoupled ring H_r relative to the ground-state energy E_0. The ground state $|2, g\rangle$ is a CDW state with $N = 2$ particles, for $U > J$ the first excited state $|2, e\rangle$ is also a CDW state with two particles. The corresponding particle densities are shown for $U = 2J$. The observed oscillation frequencies of the ring currents match the energy difference $\varepsilon(U)$ between these two states. The higher excited states are obtained by adding or removing particles, with $\Delta(U)$ denoting the corresponding energies.*

The frequency of the oscillations can be understood based on the spectrum [190] of the uncoupled ring H_r shown in Fig. 5.3. We find that the frequency ω extracted from the tdDMRG simulations matches the energy gap between the two lowest-lying states on the ring. These two states can be identified as charge-density wave (CDW) states with $N = 2$ particles on the ring, one being the ground state $|2, g\rangle$ and the other the first excited state $|2, e\rangle$. Thus we confirm what one would have expected, namely that the ring current originates from the initial state being a superposition of these two states.

The decay rate Γ of the ring currents is very rapidly decreasing with the interaction strength U, see Fig. 5.4, exhibiting a wide regime with $\Gamma \ll \Gamma_0$. To understand the origin of this regime, we proceed with the RDTT analysis.

5.4 RDTT analysis.

The RDTT [180, 181] method aims at determining the time evolution of the reduced density matrix of the nanostructure, $\rho_{ns}(t) = \mathrm{tr}_l \rho(t)$, where the trace is taken over the lead degrees of freedom in the density matrix $\rho(t)$ of the full system. The time evolution of $\rho_{ns}(t)$ can be cast in the form $\dot{\rho}_{ns}(t) = -iL_{ns}\rho_{ns}(t)$, with the effective Liouvillian L_{ns} governing the relaxation of the nanostructure. Since the ring current
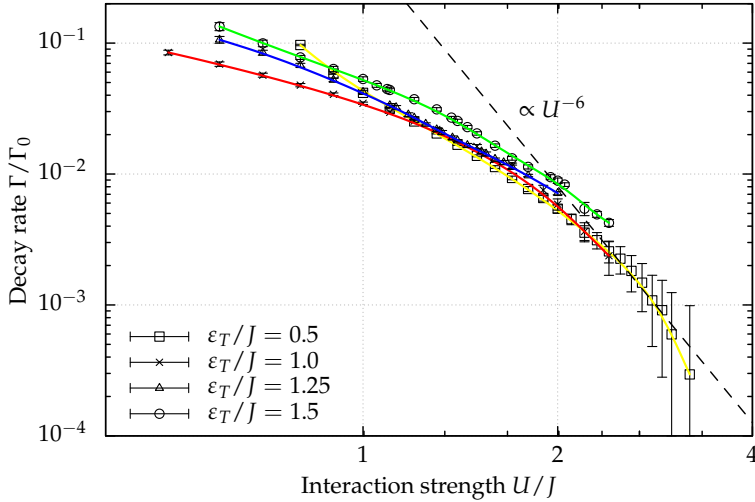
Figure 5.4: *Decay rate Γ of the ring current extracted from tdDMRG simulations. For $U/\varepsilon_T \simeq 1$ the decay rate appears to be exponentially suppressed in U, resulting in very small decay rates at large interaction values. For $U \gg \varepsilon_T$ the decay is consistent with $\Gamma \sim U^{-6}$ predicted using an effective two-level system (5.5), as is indicated by the dashed line. All other parameters as in Fig. 5.2.*

originates from the superposition of the two CDW states $|2, g\rangle$ and $|2, e\rangle$, its decay is related to the decay of the off-diagonal elements ρ_{ge} and ρ_{eg} of ρ_{ns}. In order to determine the corresponding decay rate, we have calculated [190] the effective Liouvillian to first order in the bare coupling rate Γ_0, where the perturbative regime is given by $\Gamma_0 \ll T$ with the temperature T.

The obtained results for the decay rate Γ of the ring current are shown in Fig. 5.5(a). The results are qualitatively similar to the ones obtained via tdDMRG shown in Fig. 5.4 in the sense that the rate is strongly suppressed at large U. The quantitative differences between the RDTT and tdDMRG results reflect the fact that both methods operate in different parameter regimes.

Furthermore, the RDTT allows us to identify [190] the relaxation processes contributing to the decay rate, which are visualised in Fig. 5.5(b). The dominant processes are shown in sketches (1) and (2), which involve the tunneling of a particle off or onto the ring, while the sub-leading processes are shown in sketches (3) and (4). All processes are constraint by energetics: (1) and (2) only contribute in the regions (i) and (ii) in Fig. 5.5(a), (3) only in regions (i) and (iii), and (4) is relevant in the regions (i)–(iv). We stress that in region (v) no relaxation processes in order Γ_0 exist. Thus at sufficiently large interaction strengths U the rate Γ essentially drops to zero (to order Γ_0^2), explaining the very slow decay of the ring current.
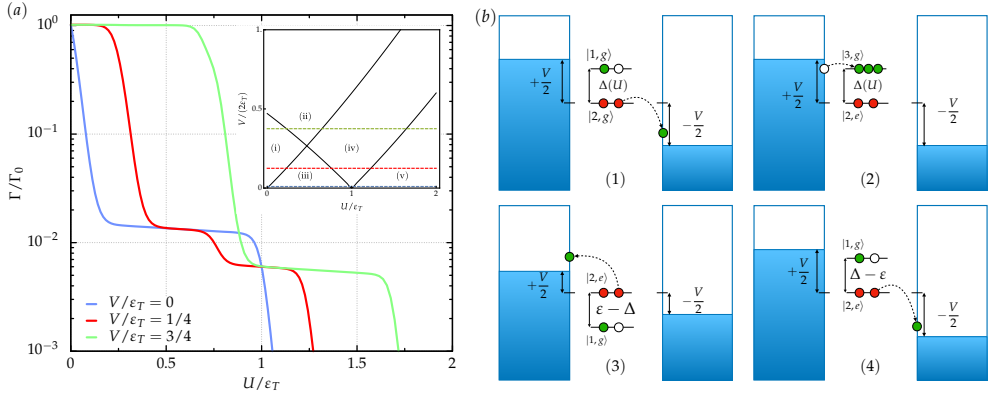
Figure 5.5: *(a) Decay rate Γ obtained from RDTT for the temperature $T = 10\,\Gamma_0$. Inset: In U-V-parameter space we identify five distinct regions labeled (i) to (v), in which Γ takes strongly different values. The dashed lines indicate cuts shown in the main figure. (b) Relaxation processes contributing to the rate Γ, which result in the distinct regions (i)–(v). Red and green dots represent initial and final configurations, respectively, $\Delta = \Delta(U)$ denotes the energy required to add or remove a particle (see Fig. 5.3), while $\varepsilon \approx \varepsilon_T$ is the energy gap between the two CDW states.*

5.5 Schrieffer–Wolff transformation.

Finally we focus on the regime of strong interactions, $U/\max(\varepsilon_T, J) \to \infty$, where we can derive the analytic dependence $\Gamma \sim U^{-6}$ consistent with our computational results, Fig. 5.4. As can be seen from the spectrum of the bare ring (Fig. 5.3), in this limit the two CDW states $|2, g\rangle$ and $|2, e\rangle$ will be well separated by an energy splitting $\Delta(U) \sim U$ from the higher excited states. It is thus instructive to construct an effective two-level system containing only these states, where the couplings to the higher excited states are treated using a Schrieffer–Wolff transformation [182] in fourth order in the couplings J and J_c. Going to this order in the expansion is necessary since all off-diagonal matrix elements exactly cancel in second order due to the mirror symmetry of the isolated ring structure [190].

The resulting two-level system can be written in the form of an electronic Kondo model, with the localised spin identified with the CDW states as $|\downarrow\rangle = |2, g\rangle$ and $|\uparrow\rangle = |2, e\rangle$ and the corresponding spin operator denoted by $\vec{S}$. An effective reservoir electronic degree of freedom can be formed via $c_{\mathrm{res},\uparrow\downarrow} = (c_L \pm c_R)/\sqrt{2}$ from the leads (5.2) of the original model; the effective spin operator formed from the first sites ($n = 0$) is denoted by $\vec{S}_{\mathrm{res}}$. With this notation the effective model reads [190]

$$
\begin{aligned}
H_{\mathrm{SW}} = \sum_{k,\sigma} \epsilon_k c^\dagger_{\mathrm{res},k\sigma} c_{\mathrm{res},k\sigma} + h S^z + \tilde{h} S^z_{\mathrm{res}} \\
+ J_\perp \left(S^x S^x_{\mathrm{res}} + S^y S^y_{\mathrm{res}} \right) + J_z S^z S^z_{\mathrm{res}},
\end{aligned}
\tag{5.4}
$$

where the first term is the energy of the electronic reservoir, the second and third are effective magnetic fields $h \approx \varepsilon_T$ and $\tilde{h} = \mathcal{O}(U^{-4}) \ll h$ acting on the two-level system and spin of the electron reservoir. The fourth and fifth term represent a Kondo coupling between the two, with the coupling being strongly anisotropic with $J_z \simeq 10 J^2 J_c^2 / U^3$ and $J_\perp = \mathcal{O}(U^{-5})$, and thus $|J_\perp| \ll |J_z| \ll J_c, J$.

Due to the formation of the effective reservoir electron spin from the leads L,R the bias voltage V enters the effective Kondo model in the form of a transverse field in the reservoir, ie, as $V/2 \sum_{k\sigma\sigma'} c_{\mathrm{res},k\sigma} \tau^x_{\sigma\sigma'} c_{\mathrm{res},k\sigma'}$ with τ^x being the x-component of the Pauli matrices. Finally, the ring current corresponds to oscillations between the two CDW states and thus is related to the localised spin via $I_r \sim S^y$. Performing a suitable spin rotation in the electronic reservoir we calculated [190] the corresponding relaxation rate using standard perturbation theory in the Kondo system [180, 193, 194] with the result

$$\Gamma = \frac{\pi J_\perp^2}{16} \left(|\varepsilon_T + V| + |\varepsilon_T - V| + 2|\varepsilon_T| \right) + \frac{\pi J_z^2}{8} V. \qquad (5.5)$$

We stress that in the considered regime of strong interactions this rate is vanishingly small, $\Gamma \sim J_z^2 V \sim J^4 J_c^4 V / U^6$, in accordance with our finding of long-lived oscillations in the ring current. In particular, the predicted behaviour $\Gamma \sim U^{-6}$ is consistent with our tdDMRG simulations shown in Fig. 5.4. We note that the result (5.5) is applicable deep in region (v) of Fig. 5.5(a), where we found that processes of order Γ_0 vanish. Finally we note that the effective model (5.4) will show the Kondo effect, however, the relevant energy scale T_K will be much smaller than the energy scales we consider here, in particular $T_K \ll \varepsilon_T$. Thus the equilibrium Kondo effect is not observable in our setup.

5.6 Experimental verification.

We see a possible experimental realisation of the ring-shaped model system, Fig. 5.1, in molecules such as porphyrines or phthalocyanines. Single molecule conductance measurements have indeed been performed at these systems [195–197] so the possibility for bias-ramping has also been demonstrated already. As an observable indicating the slow decay of the ring currents we propose to measure the photons that are emitted when these currents decay via coupling to the radiation field. In this context we note that single-molecule electroluminscence measurements have been performed [198, 199] already and thus are indeed experimentally feasible. An alternative realisation of our ring-shaped model may be provided by quantum dot arrays [200], which in particular offer a high level of control of the couplings and allow to enter the regime of strong interactions essential for the long-lived ring currents.

5.7 Conclusion.

We have studied the relaxation of transport processes in an interacting ring-shaped nanostructure. Owing to a mirror symmetry of the Hamiltonian, the system sup-

ports oscillating ring currents long after the transmitted current has died out, with the ratio Γ/Γ_0 of the respective relaxation rates being strongly suppressed by the interactions. Our work provides a striking example for an untypical situation in thermodynamic relaxation processes: Two observable currents approach their equilibrium values on timescales that are parametrically separated with rates differing by orders of magnitude. In addition, our system provides new insight into the field of quantum devices as we show that internal oscillations can be longer-lived than observed in currents through the system.

6

Chapter 6

Appendix to "Long-lived circulating currents in correlated Nanorings"

6.1 Exact diagonalization of the decoupled ring impurity

Spectrum and particle densities   We have performed an exact numerical diagonalization of the Hamiltonian matrix $H_r(U, \varepsilon_T, J)$ of the ring impurity in the absence of the leads. In figure 2 we plot the relative spectrum $(E - E_0)$ for the for eigenstates with the lowest energy. The energy of these states is shown as a function of the interaction strength U and a gate potential $\varepsilon_T = J/2$. The ground state features half-filling of the ring ($n = 2$) and is indicated by the red line. The other eigenstate in the spectrum with half-filling is shown as the blue line. The state marked by the orange line features only a single electron in the ring while the state indicated by the magenta line has three electrons in the ring. For interaction $U/\varepsilon_T \geq 1$ we observe an increasing energy separation between the two eigenstates at half-filling and the rest of the spectrum. When comparing the frequency of the observed oscillations of the local currents in the ring with the relative spectrum of the ring, we find an excellent agreement of the frequencies with the energy gap between the ground state $|2, g\rangle$ and the second eigenstate at half-filling $|2, e\rangle$. The frequencies that we have obtained from the fit of a cosine function to the data of the ring current are displayed as black dots in figure 2. We show the local electron density on the ring sites for the four low energy eigenstates in figure 2. We find that the two eigenstates at half-filling exhibit characteristics of charge density waves. The ground state has a significantly increased electron density on site 1 and 4 of the ring, while the excited state features an increased density on sites 2 and 3. The other two states have a more evenly distributed electron density. We will therefore refor to the states $|2, g\rangle$ and $|2, e\rangle$ as charge density wave (CDW) states from now on.
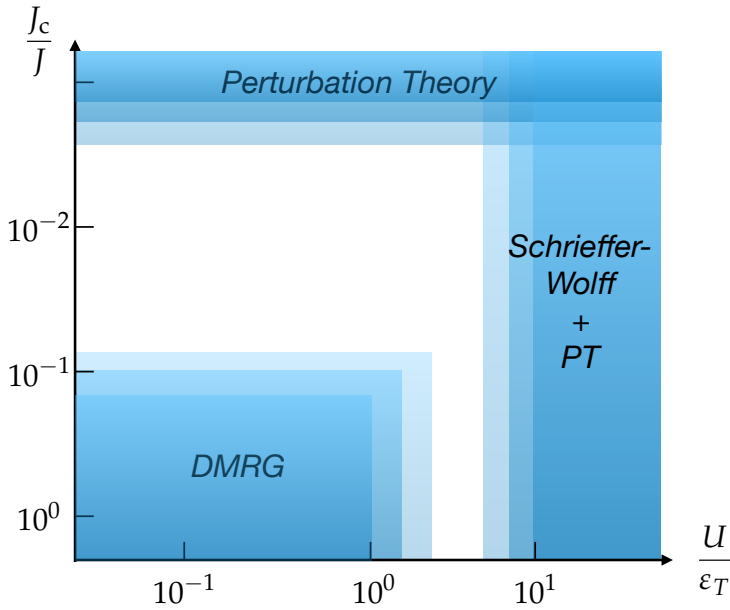
Figure 6.1: *Parameter ranges U/ε_T and J_c/J in which our employed methods are applicable. For the DMRG time evolutions we require a coupling J_c/J between leads and impurity which is large enough to allow relaxation to the nonequilibrium steady state within the maximum simulation time $L/(2v_F)$. The coupling J_c/J also needs to be larger than the typical level splitting $2\pi J/L$. The range of interaction strengths for our DMRG method is restricted by the limitations of our fitting procedure. For large enough interaction strength the fitting error exceeds the value of the fitted decay rate. The perturbation theory (more precisely reduced density-operator transport theory) is perturbative in $\rho_0 J_c^2/T$ and therefore requires small $J_c/J \ll 1$ to be valid. The Schrieffer-Wolff transformation is perturbative in $J^2 J_c^2/U^3$. It is thus only valid in the regime $U \gg J \simeq \varepsilon_T$.*
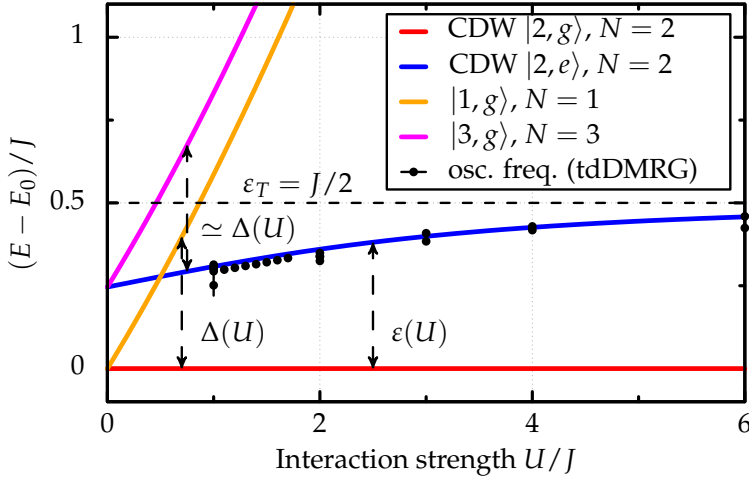
Figure 6.2: *Relative, low-energy spectrum of the bare ring impurity as a function of the interaction strength U/J in the repulsive regime $U > 0$. The red line indicates the ground state energy E_0. The blue line shows the energy of the excited charge density wave (CDW) state. $\varepsilon_T = J/2$ denotes the applied gate potential. The points indicate the values obtained within DMRG calculations for the oscillation frequency of the local currents inside the ring impurity.*
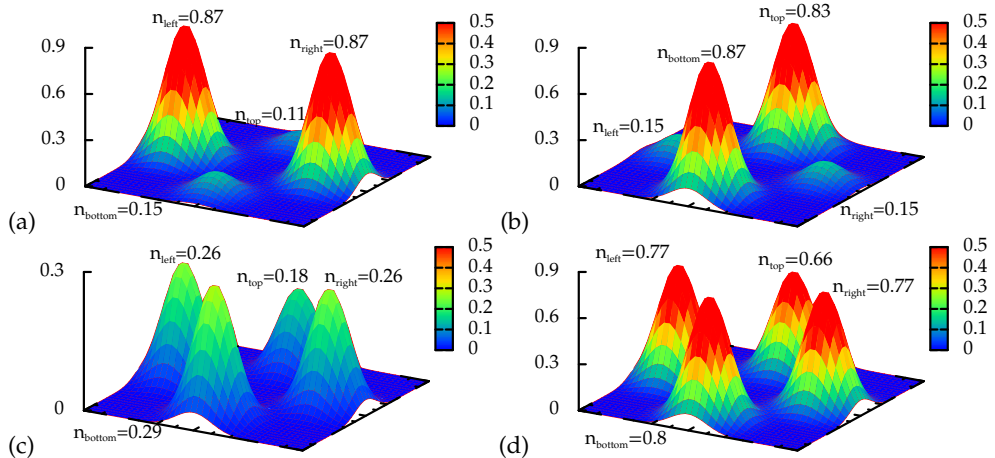
Figure 6.3: *Local electron density on the four lattice sites in the ring for $U/J = 2$ and $\varepsilon_T/J = 0.5$. (a) Density for $|2, g\rangle$. (b) Density for $|2, e\rangle$. We find the characteristics of charge density waves for (a) and (b). (c) Density for $|1, g\rangle$. (d) Density for $|3, g\rangle$.*

Time evolution of an initial superposition   We have performed DMRG calculations of the time-dependent reduced density matrix of the ring impurity. We find finite occupation probabilities for both CDW states at time $t = 0$. With increasing bias voltage, the occupation probability of the excited CDW state tends to grow as well. We have used these occupation probabilities from the DMRG to construct an initial pure state

$$|\psi_0\rangle = \sqrt{N} \left(\sqrt{\rho_{gg}}|2, g\rangle \pm \sqrt{\rho_{ee}}|2, e\rangle \right) , \tag{6.1}$$

where $\sqrt{N}$ is a normalization factor, ρ_{gg} refers to the ground state occupation probability and ρ_{ee} to the occupation probability of the excited CDW state. Using exact diagonalization we then perform the time evolution of this initial state in the bare ring impurity as

$$|\psi(t)\rangle = \exp(-iH_{\mathrm{r}}t)|\psi_0\rangle, \tag{6.2}$$

and calculate the expectation values $\langle I_{\mathrm{u}}\rangle$ and $\langle I_{\mathrm{l}}\rangle$ of the local currents in the ring. The results of this calculation are in good agreement with our DMRG results in both amplitude and frequency.

6.2 DMRG

DMRG implementation   For our numerical calculation of the time evolution of the complete system including ring impurity and leads we have employed a typical finite lattice Density Matrix Renormalization Group (DMRG) algorithm. We keep a maximum of $N_{\mathrm{cut}} = 2800$ states per block and set the maximum amount of discarded entanglement entropy to $\delta S_{\mathrm{max}} = 10^{-7}$ in each DMRG step. We use a Krylov subspace method to calculate the matrix exponential, allowing us to chose larger time steps up to Δt of order one. Each state that is reached through application of the matrix exponential onto the initial state $|\psi_0\rangle$ is included into the density matrix from which we determine the subspace of the Hilbert that we project onto in each DMRG step. At each time step we measure the observables of interest as $\langle\psi(t)|\mathcal{O}|\psi(t)\rangle$ where the operator $\mathcal{O}$ has also been projected onto the retained subspace of the Hilbert space.

Quench protocol   At time $t = 0$ we prepare the system in the ground state of

$$H(t = 0) = H + \frac{V}{2} \left(\sum_i n_{\mathrm{L},i} - \sum_i n_{\mathrm{R},i} \right) , \tag{6.3}$$

and perform the time evolution using $H(t > 0) = H$. We simulate time evolution up $t \leq L/2v_F$, where L is the length of the chain (usually $L \geq 72$) and $v_F = 2J$ is the
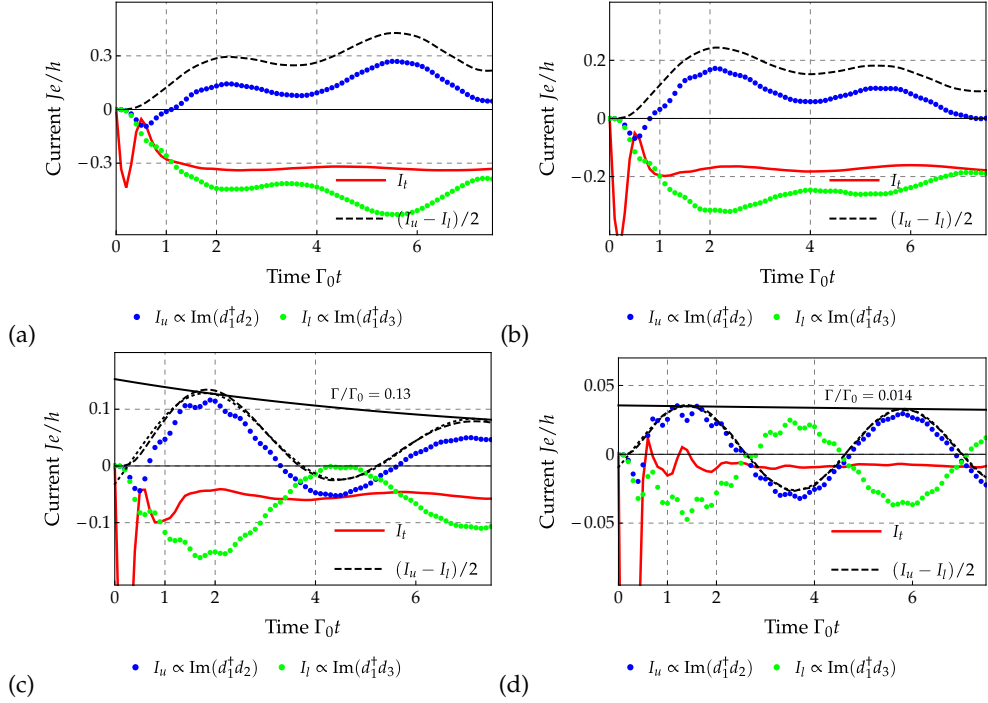
Figure 6.4: *Time dependent currents calculated within DMRG. The red line denotes the transport ("transmitted") current I_t. Blue dots mark the upper link current I_u and green dots the lower link current I_l. (a): $U/J = 0.1$, $\varepsilon_T/J = 0.5$, $eV/J = 0.4$, (b): $U/J = 0.5$, $\varepsilon_T/J = 0.5$, $eV/J = 0.4$, (c): $U/J = 1.0$, $\varepsilon_T/J = 0.5$, $eV/J = 0.4$, (d): $U/J = 2.0$, $\varepsilon_T/J = 0.5$, $eV/J = 0.4$. The solid black lines indicate a fit function $f(\Gamma_0 t) \propto \exp(\Gamma t)$.*

Fermi velocity of the fermions in the leads. During the time evolution we measure the expectation value of the local currents in the leads as

$$I_t = -2eJ \left(c_i^\dagger c_{i-1} - \text{h.c.} \right) , \tag{6.4}$$

and on specific bonds $1 \to 2$ and $1 \to 3$ in the ring (see Fig. 1 in the main paper) as

$$I_u = -eJ \left(d_2^\dagger d_1 - \text{h.c.} \right) , \tag{6.5}$$

$$I_l = -eJ \left(d_3^\dagger d_1 - \text{h.c.} \right) . \tag{6.6}$$

For the majority of our calculations we have used a set of default parameters, namely $L = 72$, $\varepsilon_T = J/2$, $J_c = J/2$ and $V = 0.4\,J/e$.

Detailed discussion of the DMRG time evolution results In figure 6.4 we plot the time-dependent expectation values of the operators I_t, I_u and I_l using our de-

fault parameters and interaction strengths $U/J \in \{0.1, 0.5, 1.0, 2.0\}$. We begin by discussing the results for weak interaction $U/J = 0.1$ shown in figure 6.4 (a). For the transmitted current $\langle I_t \rangle(t)$ we observe significant initial oscillations inside the typical transient regime $\Gamma_0 t \leq 1$ that appear to have decayed for $\Gamma_0 t > 1$ while a weak periodic oscillation remains even for large times. This periodic oscillation is not physical but a known finite size effect with a frequency $\omega \equiv V$. For the local currents in the ring we first verify that $I_u + I_l = I_t$ as a consistency check of our results. For times $\Gamma_0 t \leq 1$ we find the oscillations of $\langle I_u \rangle(t)$ and $\langle I_l \rangle(t)$ small when compared to the oscillations of $\langle I_t \rangle(t)$. The finite size effect with $\omega = V$ for the the local currents in the ring on the other hand is large when compared to the transmitted current. We also indicate $(\langle I_u \rangle - \langle I_l \rangle)/2$ as a dashed black line in fig. 6.4. This observable corresponds to a ring current in clockwise direction. For interaction strength $U/J = 0.5$, shown in fig. 6.4 (b), we solely observe quantitative differences for $\langle I_t \rangle(t)$. While the initial transient features remain largely unchanged, the steady state current for $\Gamma_0 t > 1$ is reduced. For $(\langle I_u \rangle - \langle I_l \rangle)/2$ we observe what seems to be an initial oscillatory feature that is not due to finite size effect for $\Gamma_0 t < 4$. Due to the small window $1 \leq \Gamma_0 t \leq 4$ a fit does not yield reliable results for frequency and decay rate. For $U/J = 1$ the steady state value of the transmitted current experiences yet another significant reduction, whereas the transient features remain of similar size as for $U/J = 0.1$. We stil observe that the transient features of the transmitted current have largely decayed by $\Gamma_0 t = 1$. For the ring currents we find a qualitatively different behavior. The ring current exhibits periodic oscillations with a distinct frequency and a visible decay rate Γ which is an order of magnitude smaller than Γ_0. For the directional ring current $(\langle I_u \rangle - \langle I_l \rangle)/2$ there is even a window in which the direction of the current has changed. By increasing the interaction strength to $U/J = 2$ we find yet another decrease of the steady state trnamsitted current. In the transient regime $\Gamma_0 t \leq 1$ we now also observe an additional sign change of the transmitted current. We also no longer see the oscillations due to the finite system size. The oscillations of the local currents in the ring I_u and I_l become even more pronounced and feature a periodic change of direction. Through a fit we find that the decay rate of these oscillations is an order of magnitude smaller than in the case $U/J = 1$ and now amounts to $\Gamma/\Gamma_0 \approx 1/100$. There is a clear separation of scales between the typical decay rate Γ_0 which holds for the transmitted current and the decay rate Γ of the local currents in the ring impurity. Calculations for stronger interaction $U/J > 2$ show a continuation of this trend.

Fitting procedure for the computation of Γ   To determine the oscillation frequency ε and decay rate Γ we fit a function

$$f(t) = a \exp(-\Gamma t) \cos(\varepsilon t + b) + c\,, \tag{6.7}$$

to our DMRG data for the local currents where Γ, ε, a, b and c are fitting parameters. The fit is performed for $\Gamma_0 < t < L/2v_F$. This fitting procedure only yields reliable results for $0.5 < U/J \leq 5$. For weak interaction $U/J \leq 0.5$ the decay time is too short to observe the amount of sine waves necessary to reliably determine the decay
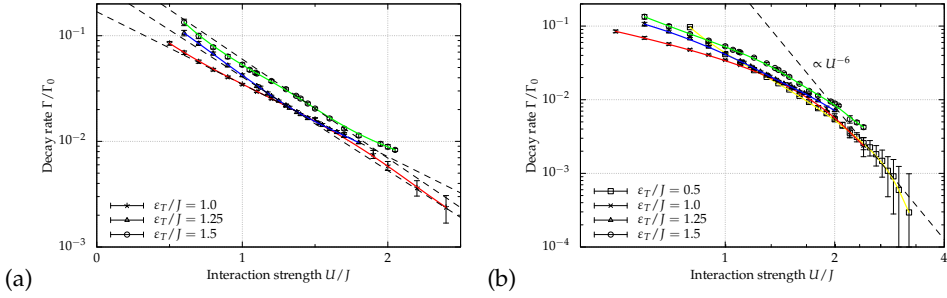
Figure 6.5: *Decay rate of the oscillating ring current obtained within DMRG calculations for several values of ε_T on a log-linear (a) and a log-log scale (b). We find that for $U \simeq \varepsilon$ the decay rate appears to be exponential in U whereas for $U \gg \varepsilon_T$ the decay rate exhibits an algebraic behavior. We plot a power law $f(U) \propto U^{-6}$ in (b) for comparison.*

rate. For very strong interaction the decay rate becomes so small that it does not lead to a visible reduction in oscillation amplitude for $t < L/2v_F$. As a result, the fitting error associated with decay rate becomes larger than the decay rate itself. These limitation of the fitting procedure limit the application of our DMRG method as a tool to determine the decay rate Γ to a parameter range $0.5 < U/J \leq 5$ as indicated in figure 5.4.

6.2.1 DMRG calculations for the decay rate Γ

We have performed a set of DMRG calculations to study the behavior of the decay rate Γ as a function of U/J for a range of specifically chosen parameters U, ε_T and V. The results of these calculations are shown in figures 6.5 (a) and (b). Due to the aforementioned limitations of our fitting procedure it is not possible to quantify Γ for $0.5 < U/J \leq 5$. In the vicinity of $U/\varepsilon_T \simeq 1$ a comparison of the log-linear and log-log plots indicates a small region of exponential suppression. For stronger interactions $U/\varepsilon_T > 1$ we observe a power law behavior of the decay rates as a function of U/J. The fit of a power law to the data indicates a smaller exponent for smaller values of ε_T. In the case of $\varepsilon_T = 0.5$ we are safely in the regime $U/\varepsilon_T \gg 1$ for $U/J \geq 4$. In this regime one could consider the data comparable to results obtained in the limit $U/\varepsilon_T \to \infty$. The fit of a power law finds an exponent $\alpha = 6.0 \pm 0.4$ in this case.

6.3 Perturbation theory in the limit of small hybridization

For our computation of the decay rate Γ, which is associated with the oscillation of the local currents in the ring, we make use of the reduced density-operator transport theory (RDTT). We mainly follow Schoeller, Eur. Phys. J. Special Topics **168**, 179 (2009). The RDTT approach is exact in the Hilbert space $\mathcal{H}_r$ of the impurity and perturbative in the hybridization between impurity and reservoirs. It may be applied if the associated perturbative scale $\Gamma_0 = 2\pi\rho_0 J_c^2$ satisfies $\Gamma_0 \ll T$, where T denotes the system temperature. The RDTT determines the time-dependent reduced density-matrix $\rho_{ns}(t)$ of an impurity by calculating corrections to the Liouvillian L of the impurity caused by tunneling processes between impurity and leads. The Liouvillian can be understood as a *superoperator* that corresponds to the action of the commutator between the Hamiltonian H and a second operator $A \in \mathcal{H}$,

$$LA \equiv \left[H, A\right]_- .\tag{6.8}$$

The von Neumann equation, which governs the time-evolution of the density matrix ρ, can be written in terms of the Liouvillian as

$$\dot{\rho}(t) = -i\left[H, \rho(t)\right]_- = -iL\rho(t),\tag{6.9}$$

and is in turn solved by

$$\rho(t) = \exp\left[-iL(t - t_0)\right]\rho(t_0).\tag{6.10}$$

A Laplace transform and a subsequent trace over the reservoir degrees of freedom of solution (6.10) yields the expression

$$\tilde{\rho}_{ns}(E) = \text{tr}_l \int_{t_0}^{\infty} dt \, \exp\left[i(E - L)(t - t_0)\right]\rho(t_0)$$

$$= \text{tr}_l \frac{i}{E - L_l - L_{ns} - L_V}\rho_l\rho_{ns}(t_0),\tag{6.11}$$

where L_{ns} denotes the original Liouvillian of the impurity and L_l the Liouvillian of the reservoirs, i.e., the total Liouvillian is decomposed as $L = L_l + L_{ns} + L_V$. Expression (6.11) can conveniently be expanded in powers of L_V, the contribution to the Liouvillian containing the coupling between the impurity and the reservoirs. The resulting series expansion for $\tilde{\rho}_{ns}$ reads

$$\tilde{\rho}_{ns}(E) = i\sum \text{tr}_l \frac{1}{E - L_l - L_{ns}}L_V \ldots L_V \frac{1}{E - L_l - L_{ns}}\rho_l\rho_{ns}(t_0).\tag{6.12}$$

In the limit $J_c^2 \ll T$ we can set up a perturbation theory in L_V. The effective Liouvillian L_{eff} of the impurity then obtains perturbative corrections $\Sigma(E)$ that are functions of the Laplace variable E. It reads

$$L_{eff}(E) = L_{ns} + \Sigma(E).\tag{6.13}$$

The transient features of the reduced density matrix $\rho_{ns}(t)$ are encoded in non-zero poles of

$$\frac{i}{E - L_{eff}(E)} . \tag{6.14}$$

To obtain these poles we solve for the complex roots of

$$z - L_{eff}(z) . \tag{6.15}$$

The Laplace variables $z^*_{\pm}$, that are roots of equation (6.15), have a real part that corresponds to an oscillation frequency ε of the associated transient feature and an imaginary part denoting its decay rate Γ. Our aim is to compute the particular Γ of the transient features whose frequency coincide with the frequency ε of the oscillation of the currents in the ring shaped impurity.

Properties of the Liouville space   In order to represent the Liouvillians L_{ns} and L_V as well as other superoperators G as matrices we introduce a new vector space $\mathcal{L}$ that we refer to as Liouville space. Objects that act as matrices in the Hilbert space $\mathcal{H}_r$ of the impurity can be thought of as vectors in this Liouville space $\mathcal{L}$. The most relevant example of such an object is the reduced density matrix ρ_{ns} of the impurity. Each matrix element $(\rho_{ns})_{i,j} = |i\rangle\langle j|$ of ρ_{ns} corresponds to a basis vector $|m)$ of the Liouville space $\mathcal{L}$. We will subsequently denote vectors in $\mathcal{H}_r$ as $|i\rangle$ and vectors in $\mathcal{L}$ as $|j)$. To represent each element of an operator $O \in \mathcal{H}_r$ as a basis vector of $\mathcal{L}$, the size of the vector space $\mathcal{L}$ has to be chosen such that $\dim(\mathcal{L}) = \dim(\mathcal{H}_r)^2$.

Definition of the superoperators   The coupling Liovilliain L_V, which can be interpreted as the interaction vertex of the perturbation theory, induces charge fluctuations on the impurity. It has the form

$$L_V = G_1^{p_1} : J_1^{p_1} :, \tag{6.16}$$

where $G_1^{p_1}$ denotes the superoperator acting on the impurity and $: J_1^{p_1} :$ the normal ordered field superoperator acting on the reservoirs. The reservoir field superoperator is defined by its action on operators A acting in the reservoir Hilbert space and reads

$$J_1^p A = \begin{cases} c_1 A & p = + \\ A c_1 & p = - \end{cases} , \tag{6.17}$$

where $1 \equiv \eta, \nu, \omega$ is a collection of indices classifying the field operator c_1 such that

$$c_1 = \begin{cases} c^\dagger_{\nu,\omega} & \eta = + \\ c_{\nu,\omega} & \eta = - \end{cases} . \tag{6.18}$$

Similarly we define $\bar{1} \equiv -\eta, \nu, \omega$. The action of the impurity vertex superoperator on this specific eigenvector is given by

$$G_1^p A = \begin{cases} d_1 A & p = + \\ -\sigma^p A d_1 & p = - \end{cases}.$$

(6.19)

The index p, that appears in the definition of both superoperators, determines whether the respective field operator acts on the second operator A from the left ($p = +$) or from the right ($p = -$). It can be interpreted as indicating the position of the field operator on the Keldysh contour and is thus sometimes referred to as Keldysh index. The operator σ^p accounts for fermionic sign factors. It returns a negative sign if

$$|l) = G_1^- |m) = |i\rangle\langle j|,$$

(6.20)

such that

$$\mathrm{mod}\left[\left(\sum_i d_i^\dagger d_i |i\rangle - \sum_i d_i^\dagger d_i |j\rangle\right), 2\right] = 1.$$

(6.21)

Reservoir contractions   We perform the trace tr_l over the lead degrees of freedom by contracting pairs of reservoir field superoperators in our series expansion of $\tilde{\rho}_{\mathrm{ns}}(E)$. We denote these contractions

$$\gamma_{11'}^{pp'} = \langle J_1^p J_{1'}^{p'} \rangle_{\mathrm{eq.}},$$

(6.22)

where $\langle \dots \rangle_{\mathrm{eq.}}$ indicates that we assume the semi-infinite reservoirs to be in thermal equilibrium. The contractions are thus proportional to the equilibrium distribution function $f(\omega)$ at temperature T. We can simplify the subsequent calculations by separating the distribution function $f(\omega)$ into a symmetric and an antisymmetric contribution. The reservoir contraction then reads

$$\gamma_{11'}^{pp'} = \delta_{1\bar{1}'} p' \gamma_1^s + \delta_{1\bar{1}'} \gamma_1^a,$$

(6.23)

with the symmetric contribution

$$\gamma_1^s = \frac{1}{2}\rho_0,$$

(6.24)

and the antisymmetric contribution

$$\gamma_1^a = \rho_0\left(f(\omega) - \frac{1}{2}\right),$$

(6.25)

where ρ_0 is the density of states in the reservoir. It is possible to absorb the Keldysh index appearing in the contraction (6.23) by introducing the vertices

$$\bar{G}_1 = \sum_{p=\pm} G_1^p,$$

(6.26)

$$\tilde{G}_1 = \sum_{p=\pm} p G_1^p.$$

(6.27)

Definition of the perturbative corrections The leading order correction $\Sigma^{(1)}(E)$ to the effective impurity Liouvillian L_{eff}, which derives from charge fluctuations, has the form

$$\Sigma^{(1)}(E) = \int_{-D}^{D} d\omega_1 \sum_{p,p'=\pm} \sum_{1,1'} G_1^p \frac{1}{\omega_1 + E + \eta_1\mu_1 - L_{\text{ns}}} G_{1'}^{p'} \gamma_{11'}^{pp'} . \tag{6.28}$$

As with the reservoir contractions we can separate $\Sigma^{(1)}(E)$ in a symmetric and an antisymmetric term,

$$\Sigma^{(1)}(E) = \Sigma_s + \Sigma_a(E), \tag{6.29}$$

where Σ_s does not depend on the Laplace variable E. When using the redefined vertices $\bar{G}_1$ and $\tilde{G}_1$ we can write Σ_s as

$$\Sigma_s = \frac{1}{2}\rho_0 \sum_{\nu_1,\eta_1} \bar{G}_1 \int_{-D}^{D} d\omega_1 \frac{1}{\omega_1 + E + \eta_1\mu_1 - L_{\text{ns}}} \tilde{G}_{\bar{1}} \tag{6.30}$$

$$= -i\frac{\pi}{2}\rho_0 \sum_{\nu_1,\eta_1} \bar{G}_1 \tilde{G}_{\bar{1}},$$

where we have integrated over all reservoir frequencies ω_1 ranging from the lower to the upper reservoir band edge D. The symmetric contribution Σ_s turns out to be entirely imaginary. It thus adds only to the decay rate of transient features but not to their oscillation frequency. The antisymmetric contribution $\Sigma_a(E)$ is a function of the Laplace variable. It reads

$$\Sigma_a(E) = -\frac{\rho_0}{2} \sum_{j=1}^{d(\mathcal{L})} \sum_{\nu_1,\eta_1} \int_{-D}^{D} d\omega_1 \frac{\tanh\left(\frac{\omega_1}{2T}\right)}{\omega_1 + E + \eta_1\mu_1 - \lambda_j} \bar{G}_1 |v_j)(v_j| \bar{G}_{\bar{1}} \tag{6.31}$$

$$= \rho_0 \sum_{j=1}^{d(\mathcal{L})} \sum_{\nu_1,\eta_1} \left[\psi\left(\frac{1}{2} - i\frac{E + \eta_1\mu_1 - \lambda_j}{2\pi T}\right) - \log\left(\frac{D}{2\pi T}\right) \right] \bar{G}_1 |v_j)(v_j| \bar{G}_{\bar{1}},$$

where $\psi(x) = \partial_x \log(\Gamma(x))$ is the Digamma function and $|v_j)$ are the eigenvectors of the initial impurity Liouvillian L_{ns} associated with the eigenvalues λ_j of L_{ns}. The imaginary part of $\Sigma_a(E)$, which is the part contributing to the decay rate, takes a more simple, intuitive form. It reads

$$\text{Im}\left(\Sigma_a(E)\right) = -\frac{\pi}{2}\rho_0 \sum_{j=1}^{d(\mathcal{L})} \sum_{\nu_1,\eta_1} \tanh\left(\frac{E + \eta_1\mu_1 - \lambda_j}{2T}\right) \bar{G}_1 |v_j)(v_j| \bar{G}_{\bar{1}}. \tag{6.32}$$

In the basis spanned by the eigenvectors $|l\rangle$ of the impurity Hamiltonian H_r the initial impurity Liouvillian L_{ns} is diagonal as well and one can easily establish a one-to-one correspondence between an eigenvector $|v_j)$ of L_{ns} and a matrix element of ρ_{ns} in this eigenbasis through

$$|v_j) = |l\rangle\langle m|, \tag{6.33}$$

with the associated eigenvalue

$$\lambda_j = E_l - E_m \, , \tag{6.34}$$

where λ_j is the energy difference between the two eigenstates $|l\rangle$ and $|m\rangle$ of the Hamiltonian H_r. There are two eigenvalues $\lambda_{\varepsilon,\pm}$ of the impurity Liovilliain L_{ns} that correspond to the energy difference between the two charge density wave eigenstates $|g\rangle$ and $|e\rangle$. We denote the eigenvector that corresponds to the positive eigenvalue $\lambda_{\varepsilon,+}$ as

$$|v_\varepsilon) = |2,e\rangle\langle 2,g| \, . \tag{6.35}$$

The action of the impurity vertex superoperators on this eigenvector is given by

$$G_1^+|v_\varepsilon) = d_1|2,e\rangle\langle 2,g| \, , \tag{6.36}$$
$$G_1^-|v_\varepsilon) = -(-1)|2,e\rangle\langle 2,g|d_1 \, , \tag{6.37}$$

where d_1 creates or annihilates a particle on lattice sites $x = 1$ or $x = 4$ of the impurity.

Perturbative diagonalization of $L_{\text{eff}}(E)$ While L_{ns} is diagonal in the eigenbasis of H_r, the corrections Σ_s and $\Sigma_a(E)$ are not. Due to the large size of the Liouville space, $\dim(\mathcal{L}) = 256$, an analytical diagonalization of the effective Liouvillian $L_{\text{eff}}(E) = L_{ns} + \Sigma_s + \Sigma_a(E)$ is not feasible. To determine the eigenvalues of $L_{\text{eff}}(E)$ we therefore treat $\Sigma_s + \Sigma_a(E)$ as perturbations to the initial Liouvillian L_{ns} and calculate the leading order corrections to its eigenvalues λ_j. This approximation is reasonable because $\|\Sigma_s + \Sigma_a(E)\| \leq J_c^2 \ll \varepsilon_T \approx \lambda_j$. The eigenvalue corresponding to $|v_\varepsilon)$ is then given by

$$\lambda_\varepsilon(E) = (v_\varepsilon|L_0|v_\varepsilon) + \left[(v_\varepsilon|\Sigma_s|v_\varepsilon) + (v_\varepsilon|\Sigma_a(E)|v_\varepsilon)\right] \, . \tag{6.38}$$

The particle number symmetry of the impurity Hamiltonian ($[H_r, \sum_j n_j] = 0$) guarantees that $\langle 2,e|d_1|2,e\rangle \equiv 0 \equiv \langle 2,g|d_1|2,g\rangle$. We therefore find

$$(v_\varepsilon|G_1^+ G_{\bar{1}}^-|v_\varepsilon) \equiv 0 \, , \tag{6.39}$$
$$(v_\varepsilon|G_1^- G_{\bar{1}}^+|v_\varepsilon) \equiv 0 \, . \tag{6.40}$$

Using (6.39) and (6.40) the perturbation theory corrections from the symmetric contribution Σ_s reduce to

$$(v_\varepsilon|\Sigma_s|v_\varepsilon) = \sum_{\nu_1,\eta_1} -i\frac{\pi}{2}\rho_0(v_\varepsilon|[G_1^+ + G_1^-][G_{\bar{1}}^+ - G_{\bar{1}}^-]|v_\varepsilon) \tag{6.41}$$

$$= \sum_{\nu_1,\eta_1} -i\frac{\pi}{2}\rho_0(v_\varepsilon|G_1^+ G_{\bar{1}}^+|v_\varepsilon) + i\frac{\pi}{2}\rho_0(v_\varepsilon|G_1^- G_{\bar{1}}^-|v_\varepsilon)$$

$$= -2\pi i\rho_0 J_c^2 = -i\Gamma_0 \, .$$

We see that the symmetric contribution from the leading order tunneling processes between reservoirs and impurity causes a decay rate Γ equal to the typical decay rate Γ_0 of transient features. However, this contribution does not yet factor in the fermion distribution function $f(\omega)$ in the reservoirs, meaning that each tunneling process is treated equally. The information about the distribution function is encoded in the antisymmetric correction $\Sigma_a(E)$.

Matrix elements of the antisymmetric contribution $\Sigma_a(E)$ The evaluation of the antisymmetric corrections is more involved as the contribution from each intermediate eigenstate $|v_j)$ of the Liouvillian L_{ns} is individually weighted by $\psi[1/2 - i(E \pm V - \lambda_j)/(2\pi T)]$. First, we identify the intermediate states $|v_j)$ that feature in the finite contributions

$$(v_\varepsilon|\bar{G}_1|v_j)(v_j|\bar{G}_{\bar{1}}|v_\varepsilon) = (v_\varepsilon|\left[G_1^+ + G_1^-\right]|v_j)(v_j|\left[G_{\bar{1}}^+ + G_{\bar{1}}^-\right]|v_\varepsilon) \tag{6.42}$$
$$= (v_\varepsilon|G_1^+|v_j)(v_j|G_{\bar{1}}^+|v_\varepsilon) + (v_\varepsilon|G_1^-|v_j)(v_j|G_{\bar{1}}^-|v_\varepsilon) \neq 0 \, .$$

The impurity vertex superoperator $G_1^\pm$ either creates or annihilates a fermion on the impurity. Finite contributions thus only involve eigenstates $|v_j)$ which satisfy $|v_j) = |m\rangle\langle 2, g|$ or $|v_j) = |2, e\rangle\langle m|$ such that $\sum_{i=1}^{4} n_i |m\rangle \in \{1, 3\}$. One finds in total $N = 8$ eigenstates in the Hilbert space $\mathcal{H}_r$ with particle number $n = 1$ or $n = 3$, implying $N_L \leq 16$ finite matrix elements. A quantitative study of the matrix elements $(G_1^\pm)_{j\varepsilon}$ reveals large contributions $|(v_j|G_1^\pm|v_\varepsilon)|^2 \simeq J_c^2$ for two eigenstates $|v_j) \in \mathcal{L}$. The two particular eigenstates are

$$|v_1^-) = |2, e\rangle\langle 1, g| \, , \tag{6.43}$$
$$|v_3^+) = |3, g\rangle\langle 2, g| \, , \tag{6.44}$$

where $|1, g\rangle$ and $|3, g\rangle$ are the two low-energy eigenstates of the impurity Hamiltonian that do not exhibit a charge density wave character and for which the energy, $E_1 = \langle 1, g|H_r|1, g\rangle < \langle 3, g|H_r|3, g\rangle = E_3$, is plotted in figure 2. The matrix elements read

$$(v_\varepsilon|G_1^-|v_1^-)(v_1^-|G_{\bar{1}}^-|v_\varepsilon) \simeq -J_c^2 \, , \tag{6.45}$$
$$(v_\varepsilon|G_1^+|v_3^+)(v_3^+|G_{\bar{1}}^+|v_\varepsilon) \simeq +J_c^2 \, , \tag{6.46}$$

where we note that the difference in Keldysh index $p = \pm$ of the vertex superoperators G_1^p causes the opposite sign of the matrix elements. An analysis of the remaining matrix elements reveals a third matrix element that gives a sizable contribution to the self energy. Here, the intermediate state is

$$|v_1^+) = |1, g\rangle\langle g| \, , \tag{6.47}$$

and the matrix element evaluates to

$$(v_\varepsilon|G_1^+|v_1^+)(v_1^+|G_{\bar{1}}^+|v_\varepsilon) \simeq +\frac{J_c^2}{80} \, . \tag{6.48}$$

The contribution from this matrix element becomes particularly relevant in the vicinity of $U = \varepsilon_T$ due to the analytic structure of its associated weight function.

(a)   (b)
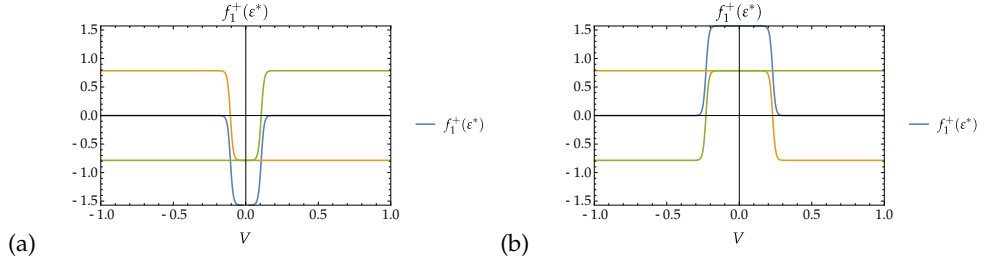
Figure 6.6: *Weight function $f_1^+(\varepsilon^*, V)$ for two values of the interaction strength, (a) $U/\varepsilon_T = 0.9$ and (b) $U/\varepsilon_T = 1.2$. The orange line indicates $f(v) = -\pi \tanh[\varepsilon - \Delta + v/(2T)]/4$ and the green line $f(v) = -\pi \tanh[\varepsilon - \Delta - v/(2T)]/4$. When $U/\varepsilon_T = 1$ and $v = 0$ the weight function changes sign and leads to complete a cancellation of the symmetric and antisymmetric corrections. The weight function $f_1^+(\varepsilon^*, V)$ becomes finite if $v \leq |\varepsilon - \Delta|$. (a): $(\varepsilon - \Delta) = 0.11$, (b): $(\varepsilon - \Delta) = -0.23$.*

Weight function   The weight function $f(\omega)$ contains the information about the fermionic distribution function $n(\omega)$ in the leads, which details the probability for an eigenstate of the lead Hmailtonian H_l with energy ω to be occupied by a fermion. Our aim is to determine the decay rate Γ which directly corresponds to the imaginary part of the the eigenvalue λ_ε of the effective Liouvillian that satisfies

$$\varepsilon^* - \lambda_\varepsilon(\varepsilon^*) = 0. \tag{6.49}$$

The imaginary part of λ_ε originates entirely from the imaginary part of the self-energy $\Sigma(\omega)$ correction, which for the asymmetric correction $\Sigma_a(\omega)$ stems from the weight function $f_j^\pm(\omega)$. The imaginary part of the weight function evaluated at the eigenvalue ε^* has the simple form

$$f_j(\varepsilon^*) = -i\frac{\pi}{2} \sum_{\eta_1 = \pm} \tanh\left(\frac{\varepsilon^* + \eta_1 \frac{V}{2} - \lambda_j}{2T}\right), \tag{6.50}$$

We know that $\varepsilon^* \simeq E_e - E_g$. We can thus also express the weigth function as

$$f_j(\varepsilon^*) = -i\frac{\pi}{2} \sum_{\eta_1 = \pm} \tanh\left(\frac{E_e - E_g - \lambda_j + \eta_1 \frac{V}{2}}{2T}\right). \tag{6.51}$$

The eigenvalues λ_j that correspond to the three largest matrix elements read

$$\lambda_1^+ = E_1 - E_g \equiv \Delta, \tag{6.52}$$

$$\lambda_3^+ = E_3 - E_g = E_3 - E_e + E_e - E_g \simeq \varepsilon + \Delta, \tag{6.53}$$

$$\lambda_1^- = E_e - E_1 = E_e - E_g + E_g - E_1 \simeq \varepsilon - \Delta, \tag{6.54}$$

It is easy to see that, depending on the eigenvalue λ_j, either the dependence on E_g or E_e is removed from the argument of the weight function. To simplify the expression we introduce $v \equiv |V/2|$. The weight function then reads

$$f_j(\varepsilon^*) = -i\frac{\pi}{2}\rho_0 \left[\tanh\left(\frac{\varepsilon - \lambda_j + v}{2T}\right) + \tanh\left(\frac{\varepsilon - \lambda_j - v}{2T}\right) \right] . \tag{6.55}$$

In the limit $T \ll \{J, U, \varepsilon, D\}$ we can approximate the weight function as

$$f_j(\varepsilon^*) = -i\frac{\pi}{2}\rho_0 \left[\text{sign}(\varepsilon - \lambda_j + v) + \text{sign}(\varepsilon - \lambda_j - v) \right] . \tag{6.56}$$

When evaluating this approximation for the three relevant eigenvalues $\lambda_j^\pm$ one finds

$$f_1^+(\varepsilon^*) = -i\frac{\pi}{2}\rho_0 \left[\text{sign}(\varepsilon - \Delta + v) + \text{sign}(\varepsilon - \Delta - v) \right] \tag{6.57}$$

$$= -i\frac{\pi}{2}\rho_0 \left[\theta(\varepsilon_T - U)\left(1 + \text{sg}(\varepsilon - \Delta - v)\right) + \theta(U - \varepsilon_T)\left(\text{sg}(\varepsilon - \Delta + v) - 1\right) \right] ,$$

$$f_3^+(\varepsilon^*) = -i\frac{\pi}{2}\rho_0 \left[\text{sign}(-\Delta + v) + \text{sign}(-\Delta - v) \right] \tag{6.58}$$

$$= -i\frac{\pi}{2}\rho_0 \left[\text{sign}(v - \Delta) - 1 \right] ,$$

$$f_1^-(\varepsilon^*) = -i\frac{\pi}{2}\rho_0 \left[\text{sign}(\Delta + v) + \text{sign}(\Delta - v) \right] \tag{6.59}$$

$$= -i\frac{\pi}{2}\rho_0 \left[1 + \text{sign}(\Delta - v) \right] ,$$

where we note that $\varepsilon, \Delta \geq 0$.

Decay channels
The three matrix elements $(v_\varepsilon | G_1^- | v_{\bar{1}}^-)(v_{\bar{1}}^- | G_{\bar{1}}^- | v_\varepsilon)$, $(v_\varepsilon | G_1^+ | v_3^+)(v_3^+ | G_{\bar{1}}^+ | v_\varepsilon)$ and $(v_\varepsilon | G_1^+ | v_1^+)(v_1^+ | G_{\bar{1}}^+ | v_\varepsilon)$ correspond to four different decay channels that cause the decoherence of a state of the form $|\psi\rangle = \alpha|2, g\rangle + \beta|2, e\rangle$. A schematic of these decay channels is shown in figure 6.8. We now turn to the discussion of the decay channels and why they become suppressed for specific sets of parameters U, ε_T and V.

$(v_\varepsilon | G_1^- | v_{\bar{1}}^-)(v_{\bar{1}}^- | G_{\bar{1}}^- | v_\varepsilon)$: An electron is ejected from the ring impurity, which has initially been in the ground state $|2, g\rangle$. Due to the particle hole symmetry of the repulsive nearest neighbor interaction U, this requires the energy $\Delta(U)$. Said energy needs to be supplied by the increase of chemical potential energy μ, which the electron gains by entering the metallic lead. The process is thus only possible if $\mu = -V/2 < -\Delta(U)$. Here, we have assumed that the electron can only enter the lead to which a negative chemical potential $-V/2 \sum_k n_k$ was applied. The condition is reflected by the weigth function $f_1^-(\varepsilon^*)$, which evaluates to zero if v surpasses Δ. Then the imaginary part of the asymmetric correction $\Sigma_a(\omega)$ does not compensate

the constant imaginary part of the symmetric correction Σ_s for this decay channel. A sketch of the decay process is shown figure 6.8 (1), where red in indicates the initial and green the final configuration of the decay process.

$(v_\varepsilon | G_1^+ | v_3^+)(v_3^+ | G_{\bar{1}}^+ | v_\varepsilon)$:   An electron tunnels onto the ring impurity, which has initially been in the excited charge density wave state $|2,e\rangle$. The additional electron increases the interaction energy on the ring impurity by $\Delta(U)$. This energy has to be supplied by the additional electron. The process is thus only possible if the chemical potential in the lead that the electron originates from satisfies $\mu = V/2 > \Delta(U)$. As with the previous matrix element, $f_3^+(\varepsilon^*)$ vanishes once $v > \Delta$ such that the constant negative imaginary part of the symmetric correction Σ_s is not compensated. We display a sketch of this decay channel in figure 6.8 (2).

The decay channels $(v_\varepsilon | G_1^- | v_1^-)(v_1^- | G_{\bar{1}}^+ | v_\varepsilon)$ and $(v_\varepsilon | G_1^+ | v_3^+)(v_3^+ | G_{\bar{1}}^+ | v_\varepsilon)$ are closely related - one involves the ground state while the other one involves the excited state - and are thus respectively allowed or suppressed in the same parameter regimes.

$(v_\varepsilon | G_1^+ | v_1^+)(v_1^+ | G^+ | v_\varepsilon)$:   An electron tunnels out of the ring impurity, which has initially been in the excited charge density wave state $|2,e\rangle$. Depending on the interaction strength U, this tunneling process is energetically favorable or unfavorable. For $U < \varepsilon_T$ the one particle state $|1,g\rangle$ is lower in energy than $|2,e\rangle$. Since the electron can carry this excess energy it can tunnel into either lead as long as $\mu = V/2 < \varepsilon - \Delta$. Having two effective decay channels, one for each lead, increases the decay rate as can be seen in sector (i) and (iii) of figure 6.7. The weight function reflects this as $f_1^+(\varepsilon^*) = -i\pi\rho_0$, which adds to the imaginary part of the symmetric correction $\Sigma_s \propto -i\pi\rho_0$ instead of compensating for it. A schematic of this process is shown in figure 6.8 (3) and (4). For $U > \varepsilon_T$ the state $|1,g\rangle$ becomes higher in energy than $|2,e\rangle$. For an electron to tunnel out of the ring additional energy is now required. This energy needs to be provided by the increase in chemical potential energy μ that the electron gains by entering the lead. The tunneling process is thus only possible if $\mu = -V/2 < -(\Delta - \varepsilon)$. We sketch this process in figure 6.8 (4).

For $U > \varepsilon_T$ and $v < \Delta - \varepsilon$ each decay channel becomes suppressed and we find

$$\text{Im} \left[\Sigma_a(\varepsilon^*) \right] \equiv -\text{Im} \left[\Sigma_s \right] . \tag{6.60}$$

The first order corrections to the imaginary part of the transient feature with oscillation frequency ε^* therefore vanish entirely.

Discussion of the phase diagram   In figure 6.7 we plot the decay rate Γ/Γ_0 of the eigenvalue $\lambda_\varepsilon(\varepsilon^*)$ as a function of the ratios U/ε_T and $V/(2\varepsilon_T)$. We identify five different sectors of these ratios in which the decay rate Γ take different values due to the presence or absence of the previously outlined decay channels respectively. In sector (i) we find the presence of the decay channels (1), (2), (3) and (4). The
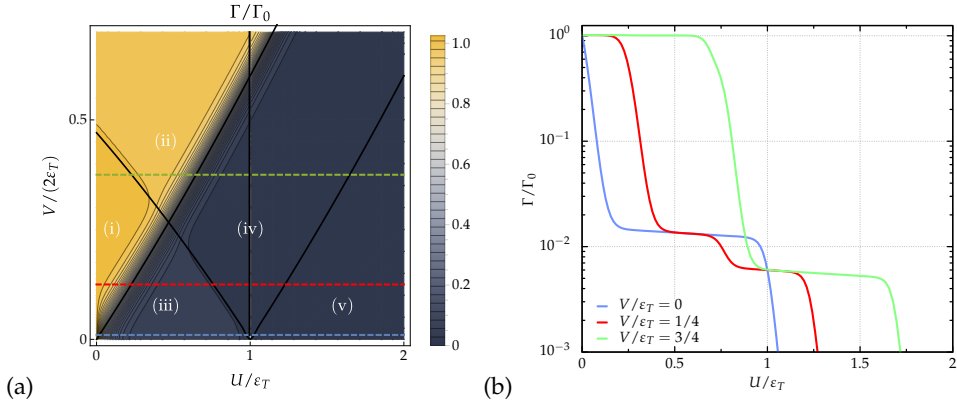
Figure 6.7: *(a) Perturbation theory results for the decay rate $\Gamma = Im[\lambda_\varepsilon(\varepsilon^*)]$ of the transient feature with oscillation frequency ε as a function of the interaction strength U/ε_T and bias voltage $V/(2\varepsilon_T)$ in units of Γ_0. We observe five distinct sectors $[(i)-(v)]$ in which the decay rate assumes different values. These sectors are characterized by their available decay channels. In sector (i) the decay rate Γ exceeds Γ_0 due to the presence of an unconventional decay channel, see fig. 6.8 (3). For $V/(2\varepsilon_T) < \Delta$ we find the dominant decay channels suppressed, leading to a decrease of the decay rate Γ by an order of magnitude compared to Γ_0. In sector (v) each decay channel is suppressed leading to an effective decay rate $\Gamma/\Gamma_0 \to 0$. (b) shows the decay rate Γ/Γ_0 as a function of U/ε_T for three distinct values of the bias voltage V. The chosen parameters are indicated by the blue, red and green dashed lines in (a).*

decay channel (3) does not exist for many of the typical quantum dot systems. Its presence leads to a decay rate Γ that exceeds the typical level broadening Γ_0. By increasing the bias voltage V one crosses from sector (i) into sector (ii) where the decay channel (3) becomes suppressed as there is no remaining unoccupied state with energy $\omega = \varepsilon_F + (\varepsilon - \Delta)$ available in the left lead . In sector (ii) we find $\Gamma = \Gamma_0$. By increasing the interaction strength U/ε_T sufficiently one passes from sector (ii) into sector (iv). The increase in interaction strength causes an increased energy gap $\Delta(U)$. As soon as $\Delta(U) > V/2$ both the decay channels (1) and (2) simultaneously become suppressed. This leads to a significant reduction of the decay rate by almost two orders of magnitude such that $\Gamma \leq \Gamma_0/80$. For $U/\varepsilon_T < 1$ the reduction of the bias voltage facilitates a crossover from sector (iv) into sector (iii). In this sector, the decay channel (3) is no longer suppressed leading to small increase of $\Delta\Gamma \simeq \Gamma_0/80$. For $U/\varepsilon_T > 1$ and $V/(2\varepsilon_T) < (\Delta - \varepsilon)$ every decay channel is suppressed as is shown in sector (v). The corresponding decay rate becomes $\Gamma/\Gamma_0 \to 0$. For a finite decay rate, higher order perturbation theory corrections would be required. However, these corrections can induce no more than a decay rate $\Gamma \propto \Gamma_0^2 \ll T$.
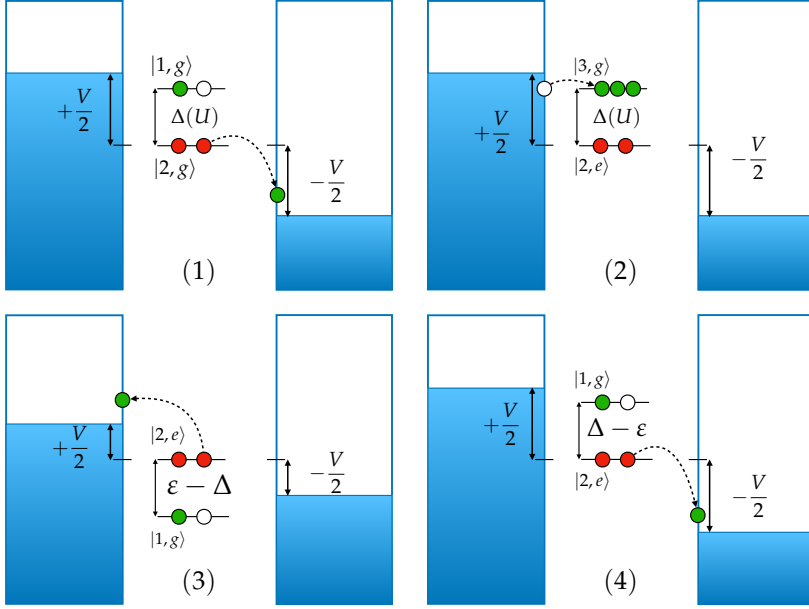
Figure 6.8: *Dominant decay channels in the first order perturbation theory. The red circles indicate the initial configuration and the green circles mark the final configuration of the process. (1): Decay channel associated with the matrix element $(v_\varepsilon | G_1^- | v_1^-)(v_1^- | G_{\bar{1}}^- | v_\varepsilon)$. An electron tunnels from the impurity into a lead, causing a transition from the ground state $|2, g\rangle$ to the excited state $|1, g\rangle$. (2): Decay channel associated with the matrix element $(v_\varepsilon | G_1^+ | v_3^+)(v_3^+ | G_{\bar{1}}^+ | v_\varepsilon)$. An electron tunnels from a lead onto the impurity, causing a transition from the excited state $|2, e\rangle$ into the excited state $|3, g\rangle$. (3): First decay channel associated with the matrix element $(v_\varepsilon | G_1^+ | v_1^+)(v_1^+ | G_{\bar{1}}^+ | v_\varepsilon)$ for $U/\varepsilon_T < 1$. An electron tunnels from the impurity into the lead with positive chemical potential $\mu = +V/2$, causing a transition from the excited state $|2, e\rangle$ to the excited state $|1, g\rangle$ which releases the energy $\varepsilon - \Delta$. (4): Second decay channel associated with the matrix element $(v_\varepsilon | G_{\bar{1}}^+ | v_1^+)(v_1^+ | G_{\bar{1}}^+ | v_\varepsilon)$. An electron tunnels from the impurity into the lead with negative chemical potential $\mu = -V/2$, causing a transition from the excited state $|2, e\rangle$ to the excited state $|1, g\rangle$ which releases the energy $\varepsilon - \Delta$ for $U/\varepsilon_T \leq 1$ and requires the energy $\Delta - \varepsilon$ for $U/\varepsilon_T > 1$.*
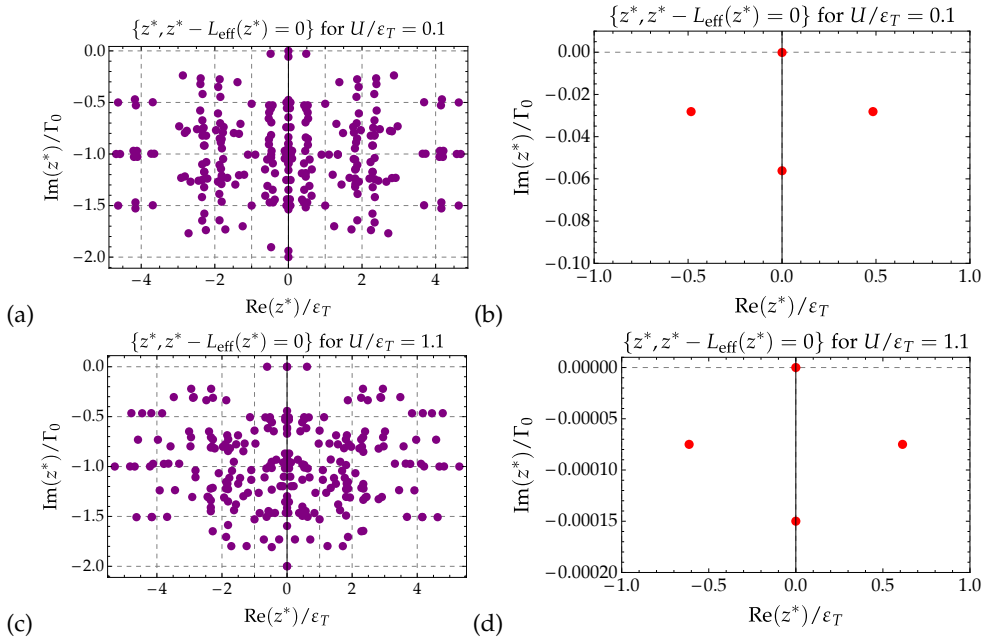
Figure 6.9: *Roots z^* of $z - L_{eff}(z) = 0$. (a),(b): $U/\varepsilon_T = 0.1$ and (c),(d): $U/\varepsilon_T = 1.1$. We find that the imaginary part $Im(z^*)$ of the majority of roots z^* is of order $\mathcal{O}(\Gamma_0)$. In addition we find four roots with an imaginary part orders of magnitude smaller than Γ_0. In (b) and (d) we zoom in on these four roots. We find that the imaginary part of three poles is two orders of magnitude smaller than Γ_0 for $U/\varepsilon_T = 0.1$ and five orders of magnitude smaller for $U/\varepsilon_T = 1.1$. The root with imaginary part $\Gamma \equiv 0$ is associated with the stationary state.*

Eigenvalue spectrum of the effective Liouvillian   The disappearance of the decay rate Γ for an eigenvalue $\lambda(z)$ of the effective Liouvillian with finite real part is unique to the eigenvalues $\pm\varepsilon^* - i\Gamma$. In figure 6.9 we display the real and imaginary part of each root of

$$z - \lambda_j(z) = 0, \tag{6.61}$$

where $\lambda_j(z)$ are the eigenvalues of the effective Liouvillian. We find that the imaginary part of all but four roots is of order $\mathcal{O}(\Gamma_0)$. This means that almost all transient features decay on the expected time scale. In figure 6.9 (d) we zoom in on the four extraordinary roots. We see that their imaginary part is $Im(z) \simeq \Gamma_0/100000$. This indicates a clear separation of scales between the decay rate of these four roots and each other root. Such a separation of scales in the solutions to (6.61) is sometimes referred to as dissipative phase transition. The four roots that feature a small imaginary part belong to $|2,g\rangle\langle 2,g|$ with root $z = 0 - i0^+$, $|2,e\rangle\langle 2,e|$ with root $z = 0 - i\Gamma_1$, $|2,e\rangle\langle 2,g|$ with root $z = \varepsilon - i\Gamma$, and $|2,g\rangle\langle 2,e|$ with root $z = -\varepsilon - i\Gamma$.

(a)

(b)
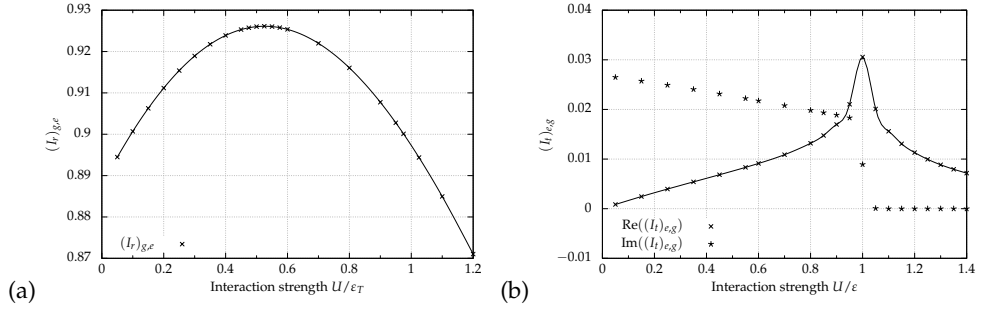
Figure 6.10: *(a) Matrix element $(I_r)_{g,e}$ of the ring current operator coupling to the transient feature of the reduced density matrix $\tilde{\rho}_{ns}(E)$ with oscillation frequency ε. (b) Real and imaginary part of the matrix element $(I_t)_{e,g}$ of the transmitted current operator coupling to the transient feature of the reduced density matrix $\tilde{\rho}_{ns}(E)$ with oscillation frequency ε.*

6.3.1 Inverse transformation to realtime

The effective reduced density matrix matrix of the impurity in Laplace space $\tilde{\rho}_{ns}(E)$ is given by

$$\tilde{\rho}_{ns}(E) = \frac{i}{E - L_{\text{eff}}(E)} \rho_{ns}(t_0) \,, \tag{6.62}$$

where each pole of the resolvent

$$\frac{1}{E - \lambda_j(E)} |v_j)(v_j| \,, \tag{6.63}$$

has an imaginary part $\Gamma_j \leq 0$. We can therefore replace the inverse Laplace transform by a Fourier transform and close the integration contour in the lower half-plane such that

$$\tilde{\rho}_{ns}(t) = \frac{1}{2\pi} \sum_j \int_{-\infty}^{+\infty} dE \, \frac{ie^{-iE(t-t_0)}}{E - \lambda_j(E)} |v_j)(v_j| \, \rho_{ns}(t_0) \tag{6.64}$$

$$= \theta(t - t_0) \sum_j \exp(i\lambda_j t - \Gamma_j t) |v_j)(v_j| \, \rho_{ns}(t_0) \,.$$

Each pole of (6.62) corresponds to a transient feature with frequency λ_j and decay rate Γ_j.

6.3.2 Coupling of the current operators to the pole λ_ε

Ring current The operator I_r measuring the local current in the ring reads

$$I_r = I_u - I_l \, , \tag{6.65}$$

$$I_u = -i\,[n_2, H] \propto i\left(d_1^\dagger d_2 - d_2^\dagger d_1\right) \, , \tag{6.66}$$

$$I_l = -i\,[n_3, H] \propto i\left(d_1^\dagger d_3 - d_3^\dagger d_1\right) \, . \tag{6.67}$$

with

$$\langle I_r \rangle(t) = \mathrm{Tr}_S\left[I_r \rho_{\mathrm{ns}}(t)\right] \, . \tag{6.68}$$

After a transformation of the current operator and the reduced density matrix ρ_{ns} to the basis of the eigenstates of Hamiltonian, this becomes

$$\langle I_r \rangle(t) = \sum_{n=1}^{d(\mathcal{H})} \langle n|\underbrace{\left(UI_rU^\dagger\right)}_{=\tilde{I}_r}\rho_{\mathrm{ns},n}(t)|n\rangle \, , \tag{6.69}$$

where $\rho_{\mathrm{ns},n}(t)$ denotes the time-dependent reduced density matrix expressed in the basis given by the eigenstates of the Hamiltonian. We are mainly interested in the matrix element of $\tilde{I}_r$ that couples to the matrix element $|v_\varepsilon\rangle = |2,e\rangle\langle 2,g|$ of the reduced density matrix

$$\langle I_r \rangle_{\mathrm{osc.}}(t) = 2\langle 2,g|\left((\tilde{I}_r)_{g,e}|2,g\rangle\langle 2,e|\right)\left[\exp(i\lambda_\varepsilon t - \Gamma t)|2,e\rangle\langle 2,g|\right]|2,g\rangle \, . \tag{6.70}$$

In figure 6.10 (a) we plot the absolute value of the coupling of the current operator to the off-diagonal matrix element $|e\rangle\langle g|$ of the reduced density matrix. We find that after an initial increase with interaction strength, the coupling decreases with interaction strength. In the entire range of values for the interaction strength that we have studied, the matrix element $(\tilde{I}_r)_{g,e}$ exceed every other matrix element of the current operator $\tilde{I}_r$.

Transmitted current We determine the extent to which the operator I_t, measuring the transmitted current, couples to the matrix elements $|2,e\rangle\langle 2,g|$ and $|2,g\rangle\langle 2,e|$ of the reduced density matrix $\tilde{\rho}_S(E)$ directly from the perturbation theory. The expectation value of the transmitted current in Laplace space is given by

$$\langle I_t \rangle(E) = \mathrm{tr}_{\mathrm{ns}}\Sigma_{I_t}(E)\frac{1}{E - L_{\mathrm{eff}}(E)}\rho_{\mathrm{ns}}(t_0) \, , \tag{6.71}$$

where

$$\Sigma_{I_t}(E) = \int_{-D}^{D} d\omega_1 \sum_{p,p'=\pm}\sum_{1,1'}(I_t)_1^p\frac{1}{\omega_1 + E + \eta_1\mu_1 - L_S}G_{1'}^{p'}\gamma_{11'}^{pp'} \, . \tag{6.72}$$

The modified vertex superoperator is defined as

$$(I_t)_1^p A = \begin{cases} I_t A & p = + \\ \sigma^p A I_t & p = - \end{cases} , \tag{6.73}$$

where the operator I_t acts in the Hilbert space $\mathcal{H}_r$ of the ring as

$$I_t = d_1^\dagger - d_1 . \tag{6.74}$$

The part of the transmitted current that acquires the small decay rate Γ is given by

$$(I_t)_{e,g} = \sum_n^{d(\mathcal{H})} \langle n| \Sigma_{I_t}(\lambda_\varepsilon) |v_\varepsilon\rangle |n\rangle , \tag{6.75}$$

where the vectors $|n\rangle$ form a basis of the Hilbert space of the ring. In figure 6.10 (b) we plot the real and imaginary part of $(I_t)_{e,g}$ as a function of U/ε_T. We find that the real part of $(I_t)_{e,g}$ is small but features a reasonance at $U = \varepsilon_T$. We thus find that only a small part of the transmitted current I_t decays with the decay rate Γ while the majority relaxes with the decay rate Γ_0.

6.4 Schrieffer-Wolff transformation and perturbation theory

6.4.1 Schrieffer-Wolff transformation of the impurity system

In the limit $U/\varepsilon_T \to \infty$ the low-energy sector of the spectrum of the uncoupled ring impurity features only the two charge density wave eigenstates $|2, g\rangle$ and $|2, e\rangle$. From figure 2 it becomes obvious that for $U/J \gg 1$ the energy gap ε between the two CDW eigenstates becomes small compared to the energy separation between the CDW states and the remainder of the spectrum. It is then intuitive to construct an effective low-energy Hamiltonian in the subspace of the Hilbert space $\mathcal{H}_r$, which is spanned by the two CDW eigenstates. In the limit $U/\varepsilon_T \to \infty$ and $U/J \to \infty$ the CDW eigenstates take the form of simple product states $|2, g\rangle = |1\rangle|0\rangle|0\rangle|1\rangle \equiv |1001\rangle$ and $|2, e\rangle = |0\rangle|1\rangle|1\rangle|0\rangle \equiv |0110\rangle$. We define the operator that projects onto this low-energy subspace as

$$P_0 = |1001\rangle\langle1001| + |0110\rangle\langle0110| . \tag{6.76}$$

The Hamiltonian of the full system can be separated into a contribution that is diagonal in this new basis

$$H_0 = \varepsilon_T n_2 + \sum_{\langle i,j\rangle} U \left(n_i n_j - \frac{n_i + n_j}{2} \right) , \tag{6.77}$$

and a contribution that connects the subspace spanned by the CDW eigenstates with the rest of the Hilbert space, which reads

$$\hat{V} = -J \sum_{\langle i,j \rangle} \left(d_i^\dagger d_j + \text{h.c.} \right) - J_c \left(d_1^\dagger c_{L,0} + d_4^\dagger c_{R,0} + \text{h.c.} \right) . \tag{6.78}$$

The second contribution can be regarded as a small perturbation. We then perform a Schrieffer-Wolff transformation to project onto the subspace spanned by the CDW states and to virtually include transitions to states orthogonal to the CDW eigenstates. We follow the work by Bravyi, DiVincenzo and Loss [Ann. Phys. **326**, 2793 (2011)] to expand the general expression for a transformation of the Hamiltonian

$$H_{\text{eff}} = P_0 \exp(S)(H_0 + \hat{V}) \exp(-S) P_0 , \tag{6.79}$$

where $\exp(S)$ is a unitary operator, into a power series up to fourth order in the perturbation $\hat{V} = V_{\text{od}} + V_{\text{d}}$ reading

$$\begin{aligned}
H_{\text{eff}}^{(4)} = \; & H_0 P_0 + P_0 \hat{V} P_0 + \frac{1}{2} P_0 \left[\mathcal{L}(V_{\text{od}}), V_{\text{od}} \right] P_0 \\
& - \frac{1}{2} P_0 \left(\left[V_{\text{od}}, \left[\mathcal{L}(V_{\text{d}}), \left[\mathcal{L}(V_{\text{d}}), \mathcal{L}(V_{\text{od}}) \right] \right] \right] \right) P_0 \\
& + \frac{1}{6} P_0 \left(\left[V_{\text{od}}, \mathcal{L}[\mathcal{L}(V_{\text{od}}), \left[\mathcal{L}(V_{\text{od}}), V_{\text{od}} \right] \right] \right) P_0 \\
& + \frac{1}{24} P_0 \left(\left[\mathcal{L}(V_{\text{od}}), \left[\mathcal{L}(V_{\text{od}}), \left[\mathcal{L}(V_{\text{od}}), V_{\text{od}} \right] \right] \right] \right) P_0,
\end{aligned} \tag{6.80}$$

where V_{od} denotes the part of the perturbation $\hat{V}$ that facilitates transitions between the low-energy Hilbert and the complementary Hilbert space and V_{d} denotes the part of the perturbation that only connects states exclusively inside either subspace. We use the shorthand

$$\mathcal{L}(X) = \frac{\langle i | X | j \rangle}{E_i - E_j} | i \rangle \langle j | , \tag{6.81}$$

to denote the inverse energy difference between two states $|i\rangle$ and $|j\rangle$ that are connected through the operator X. After evaluation of the commutators we arrive at the

expression for the effective Hamiltonian $H_{\text{eff}}^{(4)}$. It reads

$$
\begin{aligned}
H_{\text{eff}}^{(4)} = {}& H_0 P_0 + \frac{1}{2} P_0 \left[\mathcal{L}(V_{\text{od}}) V_{\text{od}} - V_{\text{od}} \mathcal{L}(V_{\text{od}}) \right] P_0 \\
& - \frac{1}{2} P_0 \left[V_{\text{od}} (\mathcal{L} V_{\text{d}})^2 \mathcal{L}(V_{\text{od}}) - \mathcal{L}(\mathcal{L}(\mathcal{L}(V_{\text{od}}) V_{\text{d}}) V_{\text{d}}) V_{\text{od}} \right] P_0 \\
& + \frac{1}{24} P_0 \left[(\mathcal{L}(V_{\text{od}}))^3 V_{\text{od}} - 3 \mathcal{L}(V_{\text{od}})^2 V_{\text{od}} \mathcal{L}(V_{\text{od}}) \right. \\
& \qquad\qquad \left. + 3 \mathcal{L}(V_{\text{od}}) V_{\text{od}} \mathcal{L}(V_{\text{od}})^2 - V_{\text{od}} \mathcal{L}(V_{\text{od}})^3 \right] P_0 \\
& + \frac{1}{6} P_0 \left[V_{\text{od}} \left(\mathcal{L}\mathcal{L}(V_{\text{od}})^2 V_{\text{od}} - 2 \mathcal{L}\mathcal{L}(V_{\text{od}}) V_{\text{od}} \mathcal{L}(V_{\text{od}}) + \mathcal{L} V_{\text{od}} \mathcal{L}(V_{\text{od}})^2 \right) \right. \\
& \qquad\qquad \left. - \mathcal{L} \left(\mathcal{L}(V_{\text{od}})^2 V_{\text{od}}^2 + 2 \mathcal{L}(V_{\text{od}}) V_{\text{od}} \mathcal{L}(V_{\text{od}}) V_{\text{od}} - V_{\text{od}} \mathcal{L}(V_{\text{od}})^2 V_{\text{od}} \right) \right] P_0 ,
\end{aligned}
\tag{6.82}
$$

where the first two lines include all contributions up to second order in the perturbation $\hat{V}$ and lines three through six contain the contributions up to fourth order.

Second order correction   Evaluating the diagonal contribution H_0 for the two CDW eigenstates yields the effective Hamiltonian in zeroth order as

$$
H_{\text{eff}}^{(0)} = H_0 P_0 = \begin{pmatrix} \varepsilon_T & 0 \\ 0 & 0 \end{pmatrix},
\tag{6.83}
$$

where from now on we treat the two CDW states like pseudo-spins defined as

$$
|0110\rangle = \begin{pmatrix} 1 \\ 0 \end{pmatrix} \equiv |\uparrow\rangle
\tag{6.84}
$$

$$
|1001\rangle = \begin{pmatrix} 0 \\ 1 \end{pmatrix} \equiv |\downarrow\rangle.
\tag{6.85}
$$

The leading order corrections to the effective Hamiltonian are of second order in the perturbation $\hat{V}$. The corrections encompass two consecutive tunneling processes, either tunneling within the ring impurity leading to corrections $\propto J^2$, or tunneling between the ring and the leads and back yielding corrections $\propto J_c^2$. In the follwing we show the calculation of each correction term featured in

$$
H_{\text{eff}}^{(2)} = H_0 P_0 + \frac{1}{2} P_0 \left[\mathcal{L}(V_{\text{od}}) V_{\text{od}} - V_{\text{od}} \mathcal{L}(V_{\text{od}}) \right] P_0.
\tag{6.86}
$$

The first leading order correction term gives

$$
\begin{aligned}
-V_{\text{od}}&\mathcal{L}(V_{\text{od}})P_0 \tag{6.87}\\
&=JV_{\text{od}}\mathcal{L}\left(d_2^\dagger d_1 + d_4^\dagger d_2 + d_3^\dagger d_4 + d_1^\dagger d_3 + d_1^\dagger d_2 + d_2^\dagger d_4 + d_4^\dagger d_3 + d_3^\dagger d_1\right)P_0\\
&\quad + J_c V_{\text{od}}\mathcal{L}\left(d_1^\dagger c_{\text{L},0} + d_4^\dagger c_{\text{R},0} + c_{\text{L},0}^\dagger d_1 + c_{\text{R},0}^\dagger d_4\right)P_0\\[4pt]
&=-J^2\left(\frac{1}{U+\varepsilon_T}d_3^\dagger d_4 d_2^\dagger d_1 + \frac{1}{U}d_2^\dagger d_1 d_3^\dagger d_4 + \frac{1}{U+\varepsilon_T}d_3^\dagger d_1 d_2^\dagger d_4 + \frac{1}{U}d_2^\dagger d_4 d_3^\dagger d_1\right)|1001\rangle\\
&\quad -J^2\left(\frac{1}{U+\varepsilon_T}d_1^\dagger d_2 d_2^\dagger d_1 + \frac{1}{U}d_4^\dagger d_3 d_3^\dagger d_4 + \frac{1}{U+\varepsilon_T}d_4^\dagger d_2 d_2^\dagger d_4 + \frac{1}{U}d_1^\dagger d_3 d_3^\dagger d_1\right)|1001\rangle\\
&\quad -J^2\left(\frac{1}{U-\varepsilon_T}d_1^\dagger d_3 d_4^\dagger d_2 + \frac{1}{U}d_4^\dagger d_2 d_1^\dagger d_3 + \frac{1}{U-\varepsilon_T}d_4^\dagger d_3 d_1^\dagger d_2 + \frac{1}{U}d_1^\dagger d_2 d_4^\dagger d_3\right)|0110\rangle\\
&\quad -J^2\left(\frac{1}{U-\varepsilon_T}d_2^\dagger d_4 d_4^\dagger d_2 + \frac{1}{U}d_3^\dagger d_1 d_1^\dagger d_3 + \frac{1}{U-\varepsilon_T}d_2^\dagger d_1 d_1^\dagger d_2 + \frac{1}{U}d_3^\dagger d_4 d_4^\dagger d_3\right)|0110\rangle\\
&\quad -J_c^2\left[\frac{1}{U}\left(c_{\text{L},0}^\dagger d_1 d_1^\dagger c_{\text{L},0} + c_{\text{R},0}^\dagger d_4 d_4^\dagger c_{\text{R},0}\right)|0110\rangle\right]\\
&\quad -J_c^2\left[\frac{1}{U}\left(d_1^\dagger c_{\text{L},0} c_{\text{L},0}^\dagger d_1 + d_4^\dagger c_{\text{R},0} c_{\text{R},0}^\dagger d_4\right)|1001\rangle\right]\\[4pt]
&=-J^2\left(\frac{1}{U+\varepsilon_T}d_2^\dagger d_3^\dagger d_4 d_1 + \frac{1}{U}d_2^\dagger d_3^\dagger d_4 d_1 - \frac{1}{U+\varepsilon_T}d_2^\dagger d_3^\dagger d_4 d_1 - \frac{1}{U}d_2^\dagger d_3^\dagger d_4 d_1\right)|1001\rangle\\
&\quad -J^2\left(\frac{2}{U+\varepsilon_T}+\frac{2}{U}\right)|1001\rangle\\
&\quad -J^2\left(\frac{-1}{U-\varepsilon_T}d_1^\dagger d_4^\dagger d_3 d_2 - \frac{1}{U}d_1^\dagger d_4^\dagger d_3 d_2 + \frac{1}{U-\varepsilon_T}d_1^\dagger d_4^\dagger d_3 d_2 + \frac{1}{U}d_1^\dagger d_4^\dagger d_3 d_2\right)|0110\rangle\\
&\quad -J^2\left(\frac{2}{U-\varepsilon_T}+\frac{2}{U}\right)|0110\rangle\\
&\quad -J_c^2\left(\frac{(1-n_{\text{L},0})+(1-n_{\text{R},0})}{U}|1001\rangle + \frac{n_{\text{L},0}+n_{\text{R},0}}{U}|0110\rangle\right),
\end{aligned}
$$

where $n_{\text{L},0}$ and $n_{\text{R},0}$ is the electron density on the site of the lead closest to the impurity for the left and the right lead respectively. The second term of the leading order

correction yields

$$\mathcal{L}(V_{\mathrm{od}})V_{\mathrm{od}}P_0 \tag{6.88}$$

$$=J^2\left(\frac{-1}{U}d_3^\dagger d_4 d_2^\dagger d_1 + \frac{-1}{U+\varepsilon_T}d_2^\dagger d_1 d_3^\dagger d_4 + \frac{-1}{U}d_3^\dagger d_1 d_2^\dagger d_4 + \frac{-1}{U+\varepsilon_T}d_2^\dagger d_4 d_3^\dagger d_1\right)|1001\rangle$$

$$+J^2\left(\frac{-1}{U+\varepsilon_T}d_1^\dagger d_2 d_2^\dagger d_1 + \frac{-1}{U}d_4^\dagger d_3 d_3^\dagger d_4 + \frac{-1}{U+\varepsilon_T}d_4^\dagger d_2 d_2^\dagger d_4 + \frac{-1}{U}d_1^\dagger d_3 d_3^\dagger d_1\right)|1001\rangle$$

$$+J^2\left(\frac{-1}{U}d_1^\dagger d_3 d_4^\dagger d_2 + \frac{-1}{U-\varepsilon_T}d_4^\dagger d_2 d_1^\dagger d_3 + \frac{-1}{U}d_4^\dagger d_3 d_1^\dagger d_2 + \frac{-1}{U-\varepsilon_T}d_1^\dagger d_2 d_4^\dagger d_3\right)|0110\rangle$$

$$+J^2\left(\frac{-1}{U-\varepsilon_T}d_2^\dagger d_4 d_4^\dagger d_2 + \frac{-1}{U}d_3^\dagger d_1 d_1^\dagger d_3 + \frac{-1}{U-\varepsilon_T}d_2^\dagger d_1 d_1^\dagger d_2 + \frac{-1}{U}d_3^\dagger d_4 d_4^\dagger d_3\right)|0110\rangle$$

$$+J_c^2\left[\frac{-1}{U}\left(c_{\mathrm{L},0}^\dagger d_1 d_1^\dagger c_{\mathrm{L},0} + c_{\mathrm{R},0}^\dagger d_4 d_4^\dagger c_{\mathrm{R},0}\right)|0110\rangle\right]$$

$$+J_c^2\left[\frac{-1}{U}\left(d_1^\dagger c_{\mathrm{L},0} c_{\mathrm{L},0}^\dagger d_1 + d_4^\dagger c_{\mathrm{R},0} c_{\mathrm{R},0}^\dagger d_4\right)|1001\rangle\right]$$

$$=J^2\left(\frac{-1}{U}d_2^\dagger d_3^\dagger d_4 d_1 + \frac{-1}{U+\varepsilon_T}d_2^\dagger d_3^\dagger d_4 d_1 - \frac{-1}{U}d_2^\dagger d_3^\dagger d_4 d_1 - \frac{-1}{U+\varepsilon_T}d_2^\dagger d_3^\dagger d_4 d_1\right)|1001\rangle$$

$$+J^2\left(\frac{-2}{U+\varepsilon_T} + \frac{-2}{U}\right)|1001\rangle$$

$$+J^2\left(\frac{1}{U}d_1^\dagger d_4^\dagger d_3 d_2 - \frac{-1}{U-\varepsilon_T}d_1^\dagger d_4^\dagger d_3 d_2 + \frac{-1}{U}d_1^\dagger d_4^\dagger d_3 d_2 + \frac{-1}{U-\varepsilon_T}d_1^\dagger d_4^\dagger d_3 d_2\right)|0110\rangle$$

$$+J^2\left(\frac{-2}{U-\varepsilon_T} + \frac{-2}{U}\right)|0110\rangle$$

$$+J_c^2\left(-\frac{(1-n_{\mathrm{L},0})+(1-n_{\mathrm{R},0})}{U}|1001\rangle - \frac{n_{\mathrm{L},0}+n_{\mathrm{R},0}}{U}|0110\rangle\right).$$

Assuming that the mean electron density in both leads combined is $n_{\mathrm{L},x}+n_{\mathrm{R},x}=1$, the two correction terms are identical. The effective Hamiltonian in leading order then reads

$$H_{\mathrm{eff}}^{(2)} = \left[\varepsilon_T - \frac{2J^2}{U-\varepsilon_T} - \frac{2J^2}{U} - \frac{J_c^2}{U}\right]\left(\frac{1}{2}+S^z\right) - \left[\frac{2J^2}{U+\varepsilon_T} + \frac{2J^2}{U} + \frac{J_c^2}{U}\right]\left(\frac{1}{2}-S^z\right) \tag{6.89}$$

$$= \left[\varepsilon_T - J^2\left(\frac{2}{U-\varepsilon_T} - \frac{2}{U+\varepsilon_T}\right)\right]S^z \equiv \varepsilon^{(2)}S^z.$$
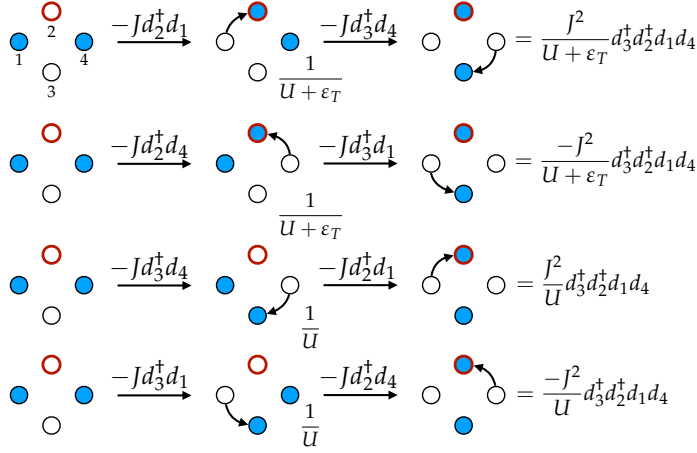
Figure 6.11: *Schematic representation of the correction terms connecting $|1001\rangle$ and $|0110\rangle$ in second order in the perturbation $\hat{V}$. There are two sets of two processes with the same amplitude that corresponds to processes which are mirror images of one another in the axis through sites 2 and 3. These processes are of opposite sign and we thus find pairwise cancellation of the off-diagonal correction terms.*

We see that the effective energy gap $\varepsilon^{(2)}$ between the ground state $|\downarrow\rangle$ and the excited state $|\uparrow\rangle$ is reduced as compared to the bare energy gap ε_T by the perturbative corrections. In leading order we furthermore find no off-diagonal terms and as it turns out not in any higher order $(J^2)^n$ of perturbations $\hat{V}$ which feature only in-ring hopping terms $\sim J\hat{d}_i^\dagger d_j$. Since the hopping between ring and leads alone cannot facilitate a pseudo-spin flip, one finds that they are not possible in leading order.

Mirror symmetry We attribute the lack of the off-diagonal, pseudo-spin flip terms to a symmetry of the nanostructure associated with the mirror symmetry in the axis through lattice sites 2 and 3 or equivalently an exchange of lattice sites $1 \leftrightarrow 4$. The operator M corresponding to this symmetry reads

$$M = \mathbf{1} + \left(d_1^\dagger - d_4^\dagger\right)\left(d_4 - d_1\right) \tag{6.90}$$
$$= \frac{1}{2}\left[-\left(d_4^\dagger d_1^\dagger d_1 d_4 + d_1^\dagger d_4^\dagger d_4 d_1\right) + \left(d_4 d_1 d_1^\dagger d_4^\dagger + d_1 d_4 d_4^\dagger d_1^\dagger\right)\right] + d_1^\dagger d_4 + d_4^\dagger d_1 \, .$$

The symmetry operator satisfies

$$M|1001\rangle = -|1001\rangle = -|\downarrow\rangle \tag{6.91}$$
$$M|0110\rangle = +|0110\rangle = +|\uparrow\rangle \, , \tag{6.92}$$

as well as

$$M^2 = \mathbf{1},\tag{6.93}$$

and

$$\left[H_r, M\right] = 0.\tag{6.94}$$

The CDW eigenstates of the Hamiltonian for $U/J \to \infty$ are also eigenstates of the symmetry operator M with eigenvalues $m = \pm 1$. Since M commutes with the Hamiltonian H_r of the uncoupled impurity for arbitrary U/J, the in-ring hopping terms of H_r cannot couple the different eigenstates of M. For the Hamiltonian H_c, which couples the ring to the leads, we instead find $\left[H_c, M\right] \neq 0$. As a consequence we have $\left[(H_c + H_r)^2, M\right] \neq 0$, indicating that off-diagonal, pseudo-spin flip terms can occur in higher orders of the perturbation. We illustrate the connection between the mirror symmetry and the absence of off-diagonal terms in leading order in figure 6.11. Each process connecting $|\downarrow\rangle$ and $|\uparrow\rangle$ has a mirror image with opposite sign leading to pairwise cancellation of all terms.

Fourth order correction   In order to obtain finite off-diagonal terms in the effective Hamiltonian one needs to include the fourth order corrections. Here we show an example calculation of one such correction term. All other fourth order correction terms follow accordingly.

$$V_{od}(\mathcal{L}V_d)^2 \mathcal{L}(V_{od})|1001\rangle \tag{6.95}$$

$$= V_{od}(\mathcal{L}V_d)^2 \mathcal{L} \left[-J\left(d_2^\dagger d_1 + d_2^\dagger d_4 + d_3^\dagger d_4 + d_3^\dagger d_1\right) \right.$$

$$\left. - J_c\left(c_{L,0}^\dagger d_1 + c_{R,0}^\dagger d_4\right) \right] |1001\rangle$$

$$= V_{od}(\mathcal{L}V_d)^2 \left[\frac{-J}{U + \varepsilon_T}\left(d_2^\dagger d_1 + d_2^\dagger d_4\right) + \frac{-J}{U}\left(d_3^\dagger d_4 + d_3^\dagger d_1\right) \right.$$

$$\left. + \frac{-J}{U}\left(c_{L,0}^\dagger d_1 + c_{R,0}^\dagger d_4\right) \right] |1001\rangle$$

$$= V_{od}\mathcal{L}V_d \left[\frac{J_c J}{(U + \varepsilon)^2}\left(d_1^\dagger c_{L,0}d_2^\dagger d_1 + c_{R,0}^\dagger d_4 d_2^\dagger d_1 + c_{L,0}^\dagger d_1 d_2^\dagger d_4 + d_4^\dagger c_{R,0}d_2^\dagger d_4\right) \right.$$

$$+ \frac{J_c J}{U^2}\left(c_{L,0}^\dagger d_1 d_3^\dagger d_4 + d_4^\dagger c_{R,0}d_3^\dagger d_4 + d_1^\dagger c_{L,0}d_3^\dagger d_1 + c_{R,0}^\dagger d_4 d_3^\dagger d_1\right)$$

$$+ \frac{J J_c}{(U + \varepsilon_T)U}\left(d_2^\dagger d_4 c_{L,0}^\dagger d_1 + d_2^\dagger d_1 c_{R,0}^\dagger d_4\right)$$

$$\left. + \frac{J J_c}{U^2}\left(d_3^\dagger d_4 c_{L,0}^\dagger d_1 + d_3^\dagger d_1 c_{R,0}^\dagger d_4\right) \right] |1001\rangle$$

The contributions that feature the underlined term in equation (6.96) combine into

$$P_0 V_{od} \mathcal{L} V_d \frac{J_c J}{(U+\varepsilon_T)^2} d_1^\dagger c_{L,0}^\dagger d_2^\dagger d_1 |1001\rangle \tag{6.96}$$

$$= P_0 \frac{J^2 J_c^2}{(U+\varepsilon_T)^3} \times$$

$$\times \Big(c_{L,0}^\dagger d_1 d_3^\dagger d_4 d_1^\dagger c_{L,0} d_2^\dagger d_1 + c_{R,0}^\dagger d_4 d_3^\dagger d_1 d_1^\dagger c_{L,0} d_2^\dagger d_1$$

$$+ d_3^\dagger d_4 c_{L,0}^\dagger d_1 d_1^\dagger c_{L,0} d_2^\dagger d_1 + d_3^\dagger d_1 c_{R,0}^\dagger d_4 d_1^\dagger c_{L,0} d_2^\dagger d_1$$

$$+ d_1^\dagger d_2 c_{L,0}^\dagger d_1 d_1^\dagger c_{L,0} d_2^\dagger d_1 + d_4^\dagger d_2 c_{R,0}^\dagger d_4 d_1^\dagger c_{L,0} d_2^\dagger d_1 \Big) |1001\rangle$$

$$= \frac{J^2 J_c^2}{(U+\varepsilon_T)^3} \Big[\big(2 n_{L,0} - 2 c_{R,0}^\dagger c_{L,0} \big) |0110\rangle + \big(n_{L,0} + c_{R,0}^\dagger c_{L,0} \big) |1001\rangle \Big] .$$

We find that the pseudo-spins on the impurity couple to a second spin-like degree of freedom in the leads which can be associated with the symmetric and antisymmetric modes in the leads. We define the annihilation operator for an electron with pseudo-spin σ in the leads as

$$c_\uparrow = \frac{1}{\sqrt{2}} \big(c_{L,0} + c_{R,0} \big) \tag{6.97}$$

$$c_\downarrow = \frac{1}{\sqrt{2}} \big(c_{L,0} - c_{R,0} \big) . \tag{6.98}$$

We use this pseudo-spin notation for the lead degrees of freedom and collect the different correction terms up to fourth order in the perturbation. The corrections read

$$V_{od} (\mathcal{L} V_d)^2 \mathcal{L} (V_{od}) |1001\rangle \tag{6.99}$$

$$= 2 J^2 J_c^2 \left(\frac{3}{U^3} + \frac{1}{U^2(U+\varepsilon_T)} - \frac{1}{U(U+\varepsilon_T)^2} - \frac{3}{(U+\varepsilon_T)^3} \right) d_\uparrow^\dagger d_\downarrow c_\downarrow^\dagger c_\uparrow$$

$$+ 2 J^2 J_c^2 \left[\left(\frac{1}{U^3} + \frac{1}{(U+\varepsilon_T)^3} \right) d_\downarrow^\dagger d_\downarrow c_\uparrow^\dagger c_\uparrow \right.$$

$$\left. + \left(\frac{4}{U^3} + \frac{1}{U^2(U+\varepsilon_T)} + \frac{2}{U(U+\varepsilon_T)^2} + \frac{1}{(U+\varepsilon_T)^3} \right) d_\uparrow^\dagger d_\downarrow c_\downarrow c_\downarrow^\dagger \right] ,$$

$$-\mathcal{L}(\mathcal{L}(\mathcal{L}(V_{\mathrm{od}})V_{\mathrm{d}})V_{\mathrm{d}})V_{\mathrm{od}}|1001\rangle \tag{6.100}$$

$$=2J^2J_{\mathrm{c}}^2\left(\frac{3}{(U-\varepsilon_T)^3}+\frac{1}{U(U-\varepsilon_T)^2}-\frac{1}{U^2(U-\varepsilon_T)}-\frac{3}{U^3}\right)d_{\uparrow}^{\dagger}d_{\downarrow}c_{\downarrow}^{\dagger}c_{\downarrow}$$

$$+2J^2J_{\mathrm{c}}^2\left[\left(\frac{1}{U^3}+\frac{1}{(U+\varepsilon_T)^3}\right)d_{\downarrow}^{\dagger}d_{\downarrow}c_{\uparrow}^{\dagger}c_{\uparrow}\right.$$

$$\left.+\left(\frac{4}{U^3}+\frac{1}{U^2(U+\varepsilon_T)}+\frac{2}{U(U+\varepsilon_T)^2}+\frac{1}{(U+\varepsilon_T)^3}\right)d_{\downarrow}^{\dagger}d_{\downarrow}c_{\downarrow}c_{\downarrow}^{\dagger}\right],$$

$$V_{\mathrm{od}}(\mathcal{L}V_{\mathrm{d}})^2\mathcal{L}(V_{\mathrm{od}})|0110\rangle \tag{6.101}$$

$$=2J^2J_{\mathrm{c}}^2\left(\frac{3}{U^3}+\frac{1}{U^2(U-\varepsilon_T)}-\frac{1}{U(U-\varepsilon_T)^2}-\frac{3}{(U-\varepsilon_T)^3}\right)d_{\downarrow}^{\dagger}d_{\uparrow}c_{\downarrow}c_{\uparrow}^{\dagger}$$

$$+2J^2J_{\mathrm{c}}^2\left[\left(\frac{1}{U^3}+\frac{1}{(U-\varepsilon_T)^3}\right)d_{\uparrow}^{\dagger}d_{\uparrow}c_{\uparrow}c_{\uparrow}^{\dagger}\right.$$

$$\left.+\left(\frac{4}{U^3}+\frac{1}{U^2(U-\varepsilon_T)}+\frac{2}{U(U-\varepsilon_T)^2}+\frac{1}{(U-\varepsilon_T)^3}\right)d_{\uparrow}^{\dagger}d_{\uparrow}c_{\downarrow}^{\dagger}c_{\downarrow}\right],$$

$$-\mathcal{L}(\mathcal{L}(\mathcal{L}(V_{\mathrm{od}})V_{\mathrm{d}})V_{\mathrm{d}})V_{\mathrm{od}}|0110\rangle \tag{6.102}$$

$$=2J^2J_{\mathrm{c}}^2\left(\frac{3}{(U+\varepsilon_T)^3}+\frac{1}{U(U+\varepsilon_T)^2}-\frac{1}{U^2(U+\varepsilon_T)^2}-\frac{3}{U^3}\right)\times$$

$$\times d_{\downarrow}^{\dagger}d_{\uparrow}c_{\downarrow}c_{\uparrow}^{\dagger}$$

$$+2J^2J_{\mathrm{c}}^2\left[\left(\frac{1}{U^3}+\frac{1}{(U-\varepsilon_T)^3}\right)d_{\uparrow}^{\dagger}d_{\uparrow}c_{\uparrow}c_{\uparrow}^{\dagger}\right.$$

$$\left.+\left(\frac{4}{U^3}+\frac{1}{U^2(U-\varepsilon_T)}+\frac{2}{U(U-\varepsilon_T)^2}+\frac{1}{(U-\varepsilon_T)^3}\right)d_{\uparrow}^{\dagger}d_{\uparrow}c_{\downarrow}^{\dagger}c_{\downarrow}\right].$$

First, we identify the off-diagonal terms which couple $|1001\rangle = |\downarrow\rangle$ and $|0110\rangle = |\uparrow\rangle$. Now, unlike the leading order corrections, the off-diagonal terms are finite and cause a simultaneous pseudo-spin-flip on the impurity and in the leads. We can thus

express the off-diagonal terms as

$$-J^2 J_c^2 \sum_\sigma \left[\frac{1}{U^2(U+\varepsilon_T)} - \frac{1}{U^2(U-\varepsilon_T)} - \left(\frac{1}{U(U+\varepsilon_T)^2} - \frac{1}{U(U-\varepsilon_T)^2} \right) \right. \qquad (6.103)$$

$$\left. - \left(\frac{3}{(U+\varepsilon_T)^3} - \frac{3}{(U-\varepsilon_T)^3} \right) \right] d_\sigma^\dagger d_{\bar\sigma} c_{\bar\sigma}^\dagger c_\sigma$$

$$= -2J^2 J_c^2 \sum_{p=\pm} \left(\frac{p}{U^2(U+p\varepsilon)} - \frac{p}{U(U+p\varepsilon)^2} - \frac{3p}{(U+p\varepsilon)^3} \right) \left(S^x S_{\text{res}}^x + S^y S_{\text{res}}^y \right).$$

We find that the off-diagonal terms describe a spin-spin interaction in the x and y direction with an amplitude $J_\perp(U, \varepsilon_T)$. The diagonal correction terms are

$$-2J^2 J_c^2 \left(\frac{1}{U^3} + \frac{1}{(U+\varepsilon_T)^3} \right) \left(\frac{1}{2}\mathbf{1} - S^z \right) \left(\frac{1}{2}\mathbf{1} + S_{\text{res}}^z \right)$$
$$(6.104)$$
$$-2J^2 J_c^2 \left(\frac{4}{U^3} + \frac{1}{U^2(U+\varepsilon_T)} + \frac{2}{U(U+\varepsilon_T)^2} + \frac{1}{(U+\varepsilon_T)^3} \right) \left(\frac{1}{2}\mathbf{1} - S^z \right) \left(\frac{1}{2}\mathbf{1} + S_{\text{res}}^z \right)$$
$$-2J^2 J_c^2 \left(\frac{1}{U^3} + \frac{1}{(U-\varepsilon_T)^3} \right) \left(\frac{1}{2}\mathbf{1} + S^z \right) \left(\frac{1}{2}\mathbf{1} - S_{\text{res}}^z \right)$$
$$-2J^2 J_c^2 \left(\frac{4}{U^3} + \frac{1}{U^2(U-\varepsilon_T)} + \frac{2}{U(U-\varepsilon_T)^2} + \frac{1}{(U-\varepsilon_T)^3} \right) \left(\frac{1}{2}\mathbf{1} + S^z \right) \left(\frac{1}{2}\mathbf{1} - S_{\text{res}}^z \right).$$

The diagonal correction terms contain three different couplings. A spin-spin interaction in the z-direction with amplitude $J_z(U, \varepsilon_T)$, a correction to the effective magnetic field on the impurity and a small effective magnetic field $h^*(U, \varepsilon_t)$ on the sites of the leads next to the impurity. The corrections expressed in the pseudo-spin notation are

$$+2J^2 J_c^2 \sum_{p=\pm} \left(\frac{5}{U^3} + \frac{1}{U^2(U+p\varepsilon_T)} + \frac{2}{U(U+p\varepsilon_T)^2} + \frac{2}{(U+p\varepsilon_T)^3} \right) S^z S_{\text{res}}^z \quad (6.105)$$

$$-J^2 J_c^2 \sum_{p=\pm} p \left(\frac{5}{U^3} + \frac{1}{U^2(U+p\varepsilon_T)} + \frac{2}{U(U+p\varepsilon_T)^2} + \frac{2}{(U+p\varepsilon_T)^3} \right) \left(S_{\text{res}}^z - S^z \right).$$

In the last step we collect the correction terms arising from lines three through five of (6.83). These read

$$\frac{1}{24}P_0\left[(\mathcal{L}(V_{\text{od}}))^3V_{\text{od}} - 3\mathcal{L}(V_{\text{od}})^2V_{\text{od}}\mathcal{L}(V_{\text{od}}) + 3\mathcal{L}(V_{\text{od}})V_{\text{od}}\mathcal{L}(V_{\text{od}})^2 - V_{\text{od}}\mathcal{L}(V_{\text{od}})^3\right]P_0$$

$$(6.106)$$

$$= -\left[\sum_{p=\pm}\frac{4p}{3}J^4\left(\frac{1}{(U+p\varepsilon_T)^3} + \frac{1}{U^2(U+p\varepsilon_T)} + \frac{1}{U(U+p\varepsilon_T)^2}\right)\right.$$

$$\left. + \frac{2p}{3}J^2J_c^2\left(\frac{1}{U^2(U+p\varepsilon_T)} + \frac{1}{U(U+p\varepsilon_T)^2}\right)\right]S^z,$$

$$\frac{1}{6}\left\{P_0\left[V_{\text{od}}\left(\mathcal{L}\mathcal{L}(V_{\text{od}})^2V_{\text{od}} - 2\mathcal{L}\mathcal{L}(V_{\text{od}})V_{\text{od}}\mathcal{L}(V_{\text{od}}) + \mathcal{L}V_{\text{od}}\mathcal{L}(V_{\text{od}})^2\right)\right]P_0 \quad (6.107)\right.$$

$$\left. + P_0\left[-\mathcal{L}\left(\mathcal{L}(V_{\text{od}})^2V_{\text{od}}^2 + 2\left(\mathcal{L}(V_{\text{od}})V_{\text{od}}\right)^2 - V_{\text{od}}\mathcal{L}(V_{\text{od}})^2V_{\text{od}}\right)\right]P_0\right\}$$

$$= \left[\sum_{p=\pm}p\frac{J^4}{3}\left(\frac{18}{(U+p\varepsilon_T)^3} + \frac{14}{U^2(U+p\varepsilon_T)} + \frac{14}{U(U+p\varepsilon_T)^2}\right)\right.$$

$$\left. + p\frac{J^2J_c^2}{6}\left(\frac{2}{(U+p\varepsilon_T)^3} + \frac{14}{U^2(U+p\varepsilon_T)} + \frac{14}{U(U+p\varepsilon_T)^2}\right)\right]S^z.$$

Adding the correction terms up to fourth order in the perturbation $\hat{V}$ to the Hamiltonian describing the lead degrees of freedom we arrive at the effective low-energy Hamiltonian $H_{\text{eff}}^{(4)}$ which reads

$$H_{\text{eff}}^{(4)} = h(U,\varepsilon_T)S^z + \tilde{h}(U,\varepsilon_T)S_{\text{res}}^z + J_z(U,\varepsilon_T)S^zS_{\text{res}}^z + J_\perp(U,\varepsilon_T)(S^xS_{\text{res}}^x + S^yS_{\text{res}}^y)$$

$$(6.108)$$

$$+ \sum_{k,\sigma}\varepsilon_k c_{k,\sigma}^\dagger c_{k,\sigma} + \theta(-t)\frac{V}{2}\sum_{k,\sigma,\sigma'}c_{k,\sigma}^\dagger \tau_{\sigma\sigma'}^x c_{k,\sigma},$$

where $h(U,\varepsilon_T)$ constitutes an effective magnetic field on the impurity and incorporates all terms coupling to $S^z \otimes \mathbf{1}_r$, $\tilde{h}(U,\varepsilon_T)$ denotes the terms proprotional to $\mathbf{1}_d \otimes S_{\text{res}}^z$, and $J_z(U,\varepsilon_T)$ and $J_\perp(U,\varepsilon_T)$ feature all terms coupling the impurity spin and the lead spins in the z-direction or x-y-direction respectively. This effective model is reminiscent of the anisotropic single-channel Kondo model with anisotropic coupling between lead spins and impurity spin in the z-direction and the x-y-plane

as well as a magnetic field $h(\varepsilon_T) \simeq \mathcal{O}(\varepsilon_T)$ on the impurity. In our effective model the spin degrees of freedom do not correspond to physical spins. Instead, we identify pseudo-spins $|\downarrow\rangle \equiv |g\rangle$ and $|\uparrow\rangle \equiv |e\rangle$ on the impurity. For vanishing bias voltage, $V = 0$, we can identify $|\downarrow\rangle$ with the antisymmetric and $|\uparrow\rangle$ with symmetric modes in the leads. The operators creating these modes read

$$c^{\dagger}_{\uparrow,k} = \frac{1}{\sqrt{2}} \left(c^{\dagger}_{L,k} + c^{\dagger}_{R,k} \right) , \tag{6.109}$$

$$c^{\dagger}_{\downarrow,k} = \frac{1}{\sqrt{2}} \left(c^{\dagger}_{L,k} - c^{\dagger}_{R,k} \right) . $$

For finite bias voltage, $V \neq 0$, the term

$$\frac{V}{2} \sum_{k,\sigma,\sigma'} c^{\dagger}_{k,\sigma} \tau^x_{\sigma,\sigma'} c_{k,\sigma'} , \tag{6.110}$$

leads to a hybridization of these two modes, which means they are no longer eigenstates of the lead Hamiltonian. The conserved quantum number becomes the lead index $\alpha = L, R$ instead. The linear dependance between lead index α and pseudo-spin index σ in the leads proves to be responsible for differing properties, e.g. decay rates, of our effective model as compared to the anisotropic Kondo model.

6.4.2 Schrieffer-Wolff transformation of the ring current operator

To determine how the ring current operator I_r couples to to the matrix elements of the reduced impurity density matrix ρ_{ns} we perform a second Schrieffer-Wolff transformation up to leading order in J^2/U. From this we obtain an effective ring current operator I_{eff} acting in the subspace P_0. The operators measuring the local currents in the ring were previously defined as

$$I_r = I_u - I_l , \tag{6.111}$$

$$I_u = -i \left[n_2, H \right] = ieJ \left(d^{\dagger}_1 d_2 - d^{\dagger}_2 d_1 \right) , \tag{6.112}$$

$$I_l = -i \left[n_3, H \right] = ieJ \left(d^{\dagger}_1 d_3 - d^{\dagger}_3 d_1 \right) . \tag{6.113}$$

The Schrieffer-Wolff has been performed in the same fashion as the transformation for the effective Hamiltonian. The resulting effective ring current operator reads

$$I_{eff} = P_0 \exp(S) \left(I_u - I_l \right) \exp(-S) P_0 \simeq P_0 \left(1 + \mathcal{L}(V_{od}) \right) \left(I_u - I_l \right) \left(1 - \mathcal{L}(V_{od}) \right) P_0 \tag{6.114}$$

$$= J^2 \left(\frac{2}{U} + \frac{1}{U - \varepsilon_T} + \frac{1}{U + \varepsilon_T} \right) S^y . $$

We immediately see that $(I_{eff})_{\uparrow,\downarrow} = (I_{eff})^{\dagger}_{\downarrow,\uparrow} \propto J^2/U$ and $(I_{eff})_{\downarrow,\downarrow} = (I_{eff})_{\uparrow,\uparrow} \equiv 0$. The effective current operator thus couples exclusively to the off-diagonal matrix

elements $\rho_{\uparrow,\downarrow}$ and $\rho_{\downarrow,\uparrow}$ of the reduced impurity density matrix ρ_{ns} of the effective low-energy model. The transient decay rate of the ring current is therefore determined by the decay rate of these two particular matrix elements.

6.4.3 Limitations on the viability of the effective low-energy model

As a consistency check of the effective model $H_{\text{eff}}^{(4)}$ up to order U^{-4} we perform a series expansion of the perturbative corrections in U^{-n} around $U/J \to \infty$. The results of this series expansion for the amplitudes of the spin-spin interaction terms read

$$J_z = 2J^2 J_c^2 \sum_{p=\pm} \frac{5}{U^3} + \frac{1}{U^2(U+p\varepsilon_T)} + \frac{2}{U(U+p\varepsilon_T)^2} + \frac{2}{(U+p\varepsilon_T)^3} \qquad (6.115)$$

$$\simeq \frac{10}{U^3} J^2 J_c^2 + \mathcal{O}\left(U^{-4}\right),$$

$$J_\perp = -2J^2 J_c^2 \sum_{p=\pm} \frac{p}{U^2(U+p\varepsilon_T)} - \frac{p}{U(U+p\varepsilon_T)^2} - \frac{3p}{(U+p\varepsilon_T)^3} \qquad (6.116)$$

$$\simeq 0 + \mathcal{O}\left(U^{-5}\right).$$

When expanding the expression for $J_\perp$ up to fourth order in the inverse interaction strength U^{-1} we encounter an inconsistency of our Schrieffer-Wolff transformation as $J_\perp$ vanishes up to this order. We can therefore not assume with certainty that the spin-spin interaction $J_\perp$ in the effective model is finite.

6.4.4 Perturbation theory for the effective model in the limit $T \to 0$

In our effective model the hybridization between the impurity and the leads satisfies

$$\sqrt{\Gamma_0} \propto \max(J_z, J_\perp) \propto \mathcal{O}(J^2 J_c^2/U^3), \qquad (6.117)$$

which is small in the limit $U \gg \max(J, \varepsilon)$ even in the case of a chosen bare coupling $J_c = \mathcal{O}(J)$. In the limit $U/\varepsilon \gg 1$ we can thus perform a perturbation theory calculation for the effective low-energy model whilst employing the same values for the bare model parameters J, J_c as in our initial DMRG calculations. This way we can compare the results from both methods for the decay rate of the off-diagonal matrix elements $\rho_{\uparrow,\downarrow}$ and $\rho_{\downarrow,\uparrow}$ and thus the decay rate of the transient ring current in the strong interaction limit. In contrast to the earlier perturbation theory calculation, we no longer study charge fluctuations on the impurity but pseudo-spin fluctuations instead. This requires a few modifications to the procedure outlined in the previous section on the perturbation theory. The coupling Liovilliain L_V now features two field superoperators for the leads and the impurity, instead of just one. It reads

$$L_V = G_{12}^{p_1 p_2} : J_1^{p_1} J_2^{p_2} :, \qquad (6.118)$$

where

$$
G_{12}^{p_1 p_2} A = \delta_{p_1 p_2} \begin{cases} d_1 d_2 A & p_1 = + \\ -A d_1 d_2 & p_1 = - \end{cases} .
\tag{6.119}
$$

The field superoperators for the leads remain unchanged

$$
J_1^p A = \begin{cases} c_1 A & p = + \\ A c_1 & p = - \end{cases} .
\tag{6.120}
$$

As a consequence, the first order corrections to the Liouvillian now contain two reservoir contractions $\gamma_{11'}^{pp'}$ which in turn requires integration over two reservoir frequencies ω_1 and ω_2. The perturbative correction reads

$$
\Sigma^{(1)}(E) = \sum_{p_1 p_2 p_3 p_4} \sum_{1234} G_{12}^{p_1 p_2} \frac{1}{E_{12} + \bar{\omega}_{12} - L_{ns}} G_{34}^{p_3 p_4} \gamma_{14}^{p_1 p_4} \gamma_{23}^{p_2 p_3} .
\tag{6.121}
$$

It is again possible to separate the corrections into a symmetric and an antisymmetric part. In the zero temperature limit the two contributions read

$$
\Sigma_s(E) = \frac{1}{4} \sum_{\nu_1, \eta_1} \sum_{\nu_2, \eta_2} \bar{G}_{12} \int_{-\infty}^{\infty} d\omega_1 d\omega_2 \frac{\rho(\omega_1)\rho(\omega_2)\left[1 + \text{sign}(\omega_1)\text{sign}(\omega_2)\right]}{E + \omega_1 + \omega_2 + \eta_1 \mu_1 + \eta_2 \mu_2 - L_{ns}} \bar{G}_{\bar{2}\bar{1}} ,
\tag{6.122}
$$

$$
\Sigma_a(E) = -\frac{1}{2} \sum_{\nu_1, \eta_1} \sum_{\nu_2, \eta_2} \bar{G}_{12} \int_{-\infty}^{\infty} d\omega_1 d\omega_2 \frac{\rho(\omega_1)\rho(\omega_2)\text{sign}(\omega_2)}{E + \omega_1 + \omega_2 + \eta_1 \mu_1 + \eta_2 \mu_2 - L_{ns}} \tilde{G}_{\bar{2}\bar{1}} .
\tag{6.123}
$$

First we discuss the integrals over the reservoir frequencies ω_1 and ω_2. For this we introduce the density of states

$$
\rho(\omega) = 2\rho_0 \theta\left(\omega - |D|\right) .
\tag{6.124}
$$

The integral in the symmetric part of the self-energy correction evaluates to

$$
\int_{-\infty}^{\infty}\int_{-\infty}^{\infty} d\omega_1 d\omega_2 \frac{\rho(\omega_1)\rho(\omega_2)}{4} \frac{1+\text{sign}(\omega_1)\text{sign}(\omega_2)}{z+\omega_1+\omega_2} \tag{6.125}
$$

$$
=\rho_0^2 \left(\int_{-D}^{0}\int_{-D}^{0} d\omega_1 d\omega_2 \frac{1}{z+\omega_1+\omega_2} \right.
$$

$$
\left. + \int_{0}^{D}\int_{0}^{D} d\omega_1 d\omega_2 \frac{1}{z+\omega_1+\omega_2} \right)
$$

$$
=\rho_0^2 \Big[2z\log z + (z-2D)\log(z-2D)
$$

$$
+ 2(z-D)\log(z-D) - 2(z+D)\log(z+D)
$$

$$
+ (z+2D)\log(z+2D) \Big]
$$

$$
\simeq \rho_0^2 \Big[2z\log z + (z-2D)\left(i\pi + \log D + \log 2 - \frac{z}{2D} \right)
$$

$$
+ (z+2D)\left(\log D + \log 2 + \frac{z}{2D} \right)
$$

$$
- 2(z+D)\left(\log D + \frac{z}{D} \right)
$$

$$
+ 2(-z+D)\left(i\pi + \log D - \frac{z}{D} \right) \Big]
$$

$$
\simeq \rho_0^2 \left[2z\log\left(\frac{2z}{D}\right) - 2z - i\pi z \right]
$$

$$
=\rho_0^2 \left[2z\log\left(\left|\frac{2z}{D}\right| - 1\right) - i\pi|z| \right] .
$$

Similarly, the integral in the antisymmetric self-energy correction gives

$$-\int_{-\infty}^{\infty}\int_{-\infty}^{\infty} d\omega_1 d\omega_2\, \frac{\rho(\omega_1)\rho(\omega_2)}{2}\, \frac{\text{sign}(\omega_2)}{z+\omega_1+\omega_2} \tag{6.126}$$

$$= -\int_{-D}^{D} 2d\omega_1 \left(\int_0^D \frac{\rho_0^2 d\omega_2}{z+\omega_1+\omega_2} - \int_{-D}^0 \frac{\rho_0^2 d\omega_2}{z+\omega_1+\omega_2} \right)$$

$$= -2\rho_0^2 \left\{ \int_{-D}^D d\omega_1 \left[-\log(\omega_1+z) + \log(\omega_1+z-D) \right] \right.$$

$$\left. + \int_{-D}^D d\omega_1 \left[-\log(\omega_1+z) + \log(\omega_1+z+D) \right] \right\}$$

$$= -2\rho_0^2 \left[2(z-D)\log(z-D) - 2(z+D)\log(z+D) \right.$$

$$\left. -(z-2D)\log(z-2D) + (z+2D)\log(z+2D) \right]$$

$$\simeq -2\rho_0^2 \left[2(z-D)\left(i\pi + \log D - \frac{z}{D} \right) \right.$$

$$- 2(z+D)\left(\log D + \frac{z}{D} \right)$$

$$+ (z+2D)\left(i\pi + \log D + \log 2 - \frac{z}{2D} \right)$$

$$\left. -(z-2D)\left(i\pi + \log D + \log 2 - \frac{z}{2D} \right) \right]$$

$$\simeq -2\rho_0^2 \left(i\pi z + 4D\log 2 \right).$$

Next, we discuss the superoperators acting in the Liouville space of the impurity. We follow the notation introduced in Schoeller and Reininghaus [Phys. Rev. B **80**, 045117 (2009)]. First we define the Liouville superoperators that act as the spin operators $\underline{S} = (S^x, S^y, S^z)$ on the impurity. These Liouville superoperators are

$$\underline{L}^{\pm} = (L^{\pm x}, L^{\pm y}, L^{\pm z}), \tag{6.127}$$

where the sign $p = \pm$ indicates the order of the operators as

$$\underline{L}^+ A = \underline{S}A \quad , \quad \underline{L}^- A = -A\underline{S}. \tag{6.128}$$

A matrix representation of these superoperators in the basis $| \uparrow\uparrow), | \downarrow\downarrow), | \uparrow\downarrow), | \downarrow\uparrow)$ reads

$$L^{+x} = \begin{pmatrix} 0 & 0 & 0 & \frac{1}{2} \\ 0 & 0 & \frac{1}{2} & 0 \\ 0 & \frac{1}{2} & 0 & 0 \\ \frac{1}{2} & 0 & 0 & 0 \end{pmatrix}, L^{+y} = \begin{pmatrix} 0 & 0 & 0 & -\frac{i}{2} \\ 0 & 0 & \frac{i}{2} & 0 \\ 0 & -\frac{i}{2} & 0 & 0 \\ \frac{i}{2} & 0 & 0 & 0 \end{pmatrix}, L^{+z} = \begin{pmatrix} \frac{1}{2} & 0 & 0 & 0 \\ 0 & -\frac{1}{2} & 0 & 0 \\ 0 & 0 & \frac{1}{2} & 0 \\ 0 & 0 & 0 & -\frac{1}{2} \end{pmatrix},$$

$$\tag{6.129}$$

$$L^{-x} = -\begin{pmatrix} 0 & 0 & \frac{1}{2} & 0 \\ 0 & 0 & 0 & \frac{1}{2} \\ \frac{1}{2} & 0 & 0 & 0 \\ 0 & \frac{1}{2} & 0 & 0 \end{pmatrix}, L^{-y} = \begin{pmatrix} 0 & 0 & 0 & -\frac{i}{2} \\ 0 & 0 & \frac{i}{2} & 0 \\ 0 & -\frac{i}{2} & 0 & 0 \\ \frac{i}{2} & 0 & 0 & 0 \end{pmatrix}, L^{-z} = \begin{pmatrix} \frac{1}{2} & 0 & 0 & 0 \\ 0 & -\frac{1}{2} & 0 & 0 \\ 0 & 0 & \frac{1}{2} & 0 \\ 0 & 0 & 0 & -\frac{1}{2} \end{pmatrix}.$$

$$(6.130)$$

From these superoperators we can construct a basis of superoperators sufficient to describe the spin-spin interaction processes between impurity and lead pseudo-spins. We further introduce the 'scalar' superoperators

$$L^a = \frac{3}{4}\mathbf{1} + \underline{L}^+ \cdot \underline{L}^-, \tag{6.131}$$

$$L^c = \frac{1}{2}\mathbf{1} + 2L^{+z}L^{-z},$$

$$L^h = L^{+z} + L^{-z},$$

as well as the vector superoperators

$$\underline{L}^1 = \frac{1}{2}\left(\underline{L}^+ - \underline{L}^- - 2i\underline{L}^+ \times \underline{L}^-\right), \tag{6.132}$$

$$\underline{L}^2 = -\frac{1}{2}\left(\underline{L}^+ + \underline{L}^-\right),$$

$$\underline{L}^3 = \frac{1}{2}\left(\underline{L}^+ - \underline{L}^- + 2i\underline{L}^+ \times \underline{L}^-\right).$$

Due to the anisotropy of the interactions we need to introduce a third set of super-operators, which reads

$$L_{\pm}^4 = L^{2x} \pm iL^{2y} \pm \left[\left(L^{+x} \pm iL^{+y}\right)L^{-z} + L^{+z}\left(L^{-x} \pm iL^{-y}\right)\right], \tag{6.133}$$

$$L_{\pm}^5 = L^{2x} \pm iL^{2y} \mp \left[\left(L^{+x} \pm iL^{+y}\right)L^{-z} + L^{+z}\left(L^{-x} \pm iL^{-y}\right)\right],$$

$$L_{\pm}^6 = L^c \pm \frac{1}{2}\left[\left(L^{3x} + iL^{3y}\right)\left(L^{1x} + iL^{1y}\right) + \left(L^{3x} - iL^{3y}\right)\left(L^{1x} - iL^{1y}\right)\right].$$

In terms of these basis superoperators the bare Liouvillian is given as

$$L_{\mathrm{ns}} = h(U, \varepsilon_T)L^h, \tag{6.134}$$

where $h(U, \varepsilon_T)$ is the effective magnetic field on the impurity and L^h represents the action of $[S^z, \bullet]$ on the impurity. The effective Liouvillian for the impurity in first order perturbation theory reads

$$L_{\mathrm{eff}}(E) = L_{\mathrm{ns}} + \Sigma^{(1)}(E). \tag{6.135}$$

The first order, energy-dependent self-energy corrections are

$$\Sigma^{(1)}(E) = \rho_0^2 \sum_{\substack{\nu_1,\eta_1 \\ \nu_2,\eta_2}} \bar{G}_{12} \left[2(E + \mu_{12} - L_{\text{ns}}) \left(\log \left| \frac{2(E + \mu_{12} - L_{\text{ns}})}{D} \right| - 1 \right) \right] \bar{G}_{\bar{2}\bar{1}} \quad (6.136)$$

$$+ \rho_0^2 \sum_{\substack{\nu_1\cdot\eta_1 \\ \nu_2,\eta_2}} \bar{G}_{12} \left[-i\pi \left| E + \mu_{12} - L_{\text{ns}} \right| \right] \bar{G}_{\bar{2}\bar{1}}$$

$$+ \rho_0^2 \sum_{\substack{\nu_1,\eta_1 \\ \nu_2,\eta_2}} \bar{G}_{12} \left[-8D \log 2 - 2\pi i (E + \mu_{12} - L_{\text{ns}}) \right] \tilde{G}_{\bar{2}\bar{1}} ,$$

where $\mu_{12} = \eta_1 \mu_1 + \eta_2 \mu_2$ and

$$\bar{G}_{12} = \begin{cases} +J_\perp \left(\tau^x_{\sigma_1\sigma_2} L^{2x} + \tau^y_{\sigma_1\sigma_2} L^{2y} \right) + J_z \tau_{\sigma_1\sigma_2} L^{2z} & \eta_1 = -\eta_2 = + \\ -J_\perp \left(\tau^x_{\sigma_2\sigma_1} L^{2x} + \tau^y_{\sigma_2\sigma_1} L^{2y} \right) - J_z \tau_{\sigma_2\sigma_1} L^{2z} & \eta_1 = -\eta_2 = - \end{cases} , \quad (6.137)$$

as well as

$$\tilde{G}_{12} = \begin{cases} +J_\perp \left[\tau^x_+ \left(L^{1x} + L^{3x} \right) + \tau^y_+ \left(L^{1y} + L^{3y} \right) \right] + J_z \tau_+ \left(L^{1z} + L^{3z} \right) & \eta_1 = + \\ -J_\perp \left[\tau^x_- \left(L^{1x} + L^{3x} \right) + \tau^y_- \left(L^{1y} + L^{3y} \right) \right] - J_z \tau_- \left(L^{1z} + L^{3z} \right) & \eta_1 = - \end{cases} , $$

$$(6.138)$$

where $\eta_1 \equiv -\eta_2$ and we have introduced $\tau^\alpha_+ = \tau^\alpha_{\sigma_1,\sigma_2}$ and $\tau^\alpha_- = \tau^\alpha_{\sigma_2,\sigma_1}$ for abbreviation. It is then straightforward to calculate the self energy corrections that are proportional to simple products $\bar{G}_{12}\bar{G}_{\bar{2}\bar{1}}$ and $\bar{G}_{12}\tilde{G}_{\bar{2}\bar{1}}$. The two different products of superoperators evaluate to

$$\bar{G}_{12}\bar{G}_{\bar{2}\bar{1}} = \sum_j \bar{G}_{12} |v_j)(v_j| \bar{G}_{\bar{2}\bar{1}} \quad (6.139)$$

$$= \frac{J_\perp^2}{2} L^c + \frac{J_\perp^2}{2} L^c + J_\perp^2 \left(L^a - L^c \right) + \frac{J_z^2}{2} \left(L^c + L^h \right) + J_\perp^2 \left(L^a - L^c \right) + \frac{J_z^2}{2} \left(L^c - L^h \right),$$

and

$$\bar{G}_{12}\tilde{G}_{\bar{2}\bar{1}} = \sum_j \bar{G}_{12} |v_j)(v_j| \tilde{G}_{\bar{2}\bar{1}} = \frac{J_\perp^2}{2} L^h - \frac{J_\perp^2}{2} L^h + J_z^2 L^{3z} - J_\perp^2 L^{3z} . \quad (6.140)$$

To calculate terms involving $\bar{G} f(\mu_{12}) \bar{G}$ and $\bar{G} f(\mu_{12}) \tilde{G}$ a rotation to a different basis is necessary.

6.4.5 Modifications to the perturbation theory for spin fluctuations due to the linear dependence between pseudo-spin and lead index

From eq. (6.106) we see that the magnetic field $\tilde{h}(U, \varepsilon_T)$, experienced by the pseudo-spins on the lead sites closest to the impurity, is small up to order $\mathcal{O}(U^{-4})$, ie $h^* \ll h, V$ and we can thus neglect it. It is then more useful to express the Hamiltonian in the basis of the lead index $\alpha \in \{L, R\}$ eigenstates, which corresponds to a rotation $\tau^x_{\sigma_1\sigma_2} \to \tau^z_{\alpha_1\alpha_2}$, $\tau^y_{\sigma_1\sigma_2} \to -\tau^y_{\alpha_1\alpha_2}$, $\tau^z_{\sigma_1\sigma_2} \to \tau^x_{\alpha_1\alpha_2}$ in the leads. In terms of the rotated operators, $c_{\alpha,k} = 1/\sqrt{2}(c_{\downarrow,k} \pm c_{\uparrow,k})$, the effective Hamiltonian reads

$$H^{(4)}_{\text{eff}} = hS^z + \sum_{k,\alpha} \varepsilon_k c^\dagger_{k,\alpha} c_{k,\alpha} + \frac{V}{2} \sum_{k,\alpha,\alpha'} c^\dagger_{k,\alpha} \tau^z_{\alpha\alpha'} c_{k,\alpha'} \tag{6.141}$$
$$+ \frac{J_z}{2} \sum_{\substack{k,k' \\ \alpha,\alpha'}} S^z c^\dagger_{k,\alpha} \tau^x_{\alpha\alpha'} c_{k',\alpha'} + \frac{J_\perp}{2} \sum_{\substack{k,k' \\ \alpha,\alpha'}} c^\dagger_{k,\alpha} c_{k',\alpha'} (S^x \tau^z_{\alpha\alpha'} + S^y(-\tau^y_{\alpha\alpha'})).$$

In this rotated basis the part of the Hamiltonian acting exclusively on the leads is diagonal so the reservoir contractions reduce to simple fermionic distribution functions. After rotation the vertex superoperators read

$$\bar{G}_{12} = \begin{cases} + \left[J_\perp L^{2x} \tau^z_{\alpha_1\alpha_2} + J_\perp L^{2y}(-\tau^y_{\alpha_1\alpha_2}) + J_z L^{2z} \tau^x_{\alpha_1\alpha_2} \right] & \eta_1 = -\eta_2 = + \\ - \left[J_\perp L^{2x} \tau^z_{\alpha_2\alpha_1} + J_\perp L^{2y}(-\tau^y_{\alpha_2\alpha_1}) + J_z L^{2z} \tau^x_{\alpha_2\alpha_1} \right] & \eta_1 = -\eta_2 = - \end{cases}, \tag{6.142}$$

and

$$\tilde{G}_{12} = \begin{cases} + \left[J_\perp \left((L^{1x} + L^{3x})\tau^z_+ - (L^{1y} + L^{3y})\tau^y_+ \right) + J_z(L^{1z} + L^{3z})\tau^x_+ \right] & \eta_1 = + \neq \eta_2 \\ - \left[J_\perp \left((L^{1x} + L^{3x})\tau^z_- - (L^{1y} + L^{3y})\tau^y_- \right) + J_z(L^{1z} + L^{3z})\tau^x_- \right] & \eta_1 = - \neq \eta_2 \end{cases},$$
$$\tag{6.143}$$

where we have introduced $\tau_+ = \tau_{\alpha_1,\alpha_2}$ and $\tau_- = \tau_{\alpha_2,\alpha_1}$ and have dropped the factor $1/2$ resulting from the substitution $S_{\sigma_1\sigma_2} \to \tau_{\alpha_1\alpha_2}$ for convenience. We reintroduce the factor in the final result. The first set of self-energy corrections that are affected by the linear dependance between pseudo-spin index and lead index involve terms proportional to $\bar{G}_{12}\mu_{12}\bar{G}_{\bar{2}\bar{1}}$ and $\bar{G}_{12}\mu_{12}\tilde{G}_{\bar{2}\bar{1}}$. The first term reads

$$\bar{G}_{12}\mu_{12}\bar{G}_{\bar{2}\bar{1}} = \sum_{\alpha_1,\alpha_2} \sum_{\eta_1=-\eta_2} \sum_{l,k=x,y,z} \tau^l_{\alpha_1\alpha_2} \tau^k_{\alpha_2\alpha_1} L^{2l} \left(\eta_1 V_{\alpha_1} + \eta_2 V_{\alpha_2} \right) L^{2k}. \tag{6.144}$$

In the following we evaluate the cases $l = k$ and $l \neq k$ separately. For each example calculation we set $\eta_1 = -\eta_2 = +$ without loss of generality. For $l = k$ we find

$$\bar{G}_{12} \mu_{12} \bar{G}_{\bar{2}\bar{1}} = J_l^2 \sum_{\substack{\alpha_1, \alpha_2 = 1,2 \\ l = x,y,z}} \tau_{\alpha_1 \alpha_2}^l \tau_{\alpha_2 \alpha_1}^l \left(V_{\alpha_1} - V_{\alpha_2} \right) L^{2l} L^{2l} \tag{6.145}$$

$$= J_l^2 \sum_{\substack{\alpha_1, \alpha_2 = 1,2 \\ l = x,y,z}} \tau_{\alpha_1 \alpha_2}^l \tau_{\alpha_2 \alpha_1}^l \left[\text{sign}(V_{\alpha_1})(1 - \delta_{\alpha_1 \alpha_2}) \right] L^{2l} L^{2l}$$

$$= J_l^2 V \sum_{l = x,y,z} \left[\text{sign}(V_2) \tau_{21}^l \tau_{12}^l + \text{sign}(V_1) \tau_{12}^l \tau_{21}^l \right] L^{2l} L^{2l} = 0,$$

and for $l \neq k$ we obtain

$$\bar{G}_{12} \mu_{12} \bar{G}_{\bar{2}\bar{1}} = J_l J_k \sum_{\substack{l \neq k \\ l,k = x,y,z}} \sum_{\alpha_1, \alpha_2 = 1,2} \tau_{\alpha_1 \alpha_2}^l \tau_{\alpha_2 \alpha_1}^k \left[\text{sign}(V_{\alpha_1})(1 - \delta_{\alpha_1 \alpha_2}) \right] L^{2l} L^{2k} \tag{6.146}$$

$$= J_l J_k V \sum_{\substack{l \neq k \\ l,k = x,y,z}} \left[\text{sign}(V_2) \tau_{21}^l \tau_{12}^k + \text{sign}(V_1) \tau_{12}^l \tau_{21}^k \right] L^{2l} L^{2k}$$

$$= \left(J_z J_\perp \right) V L^{2x}.$$

This term, proportional to the bias voltage V, does not appear in the perturbation theory of the regular anisotropic Kondo model. The correction term still satisfies $\text{Tr}_S(L^{2x}) = 0$ such that $\text{Tr}_S(L_{\text{eff}}) = 0$, a necessary requirement for the validity of the perturbation theory. Similarly for $\bar{G}_{12} \mu_{12} \tilde{G}_{\bar{2}\bar{1}}$ we find

$$\bar{G}_{12} \mu_{12} \tilde{G}_{\bar{2}\bar{1}} = J_l J_k \sum_{\substack{l \neq k \\ l,k = x,y,z}} \sum_{\alpha_1, \alpha_2 = 1,2} \tau_{\alpha_1 \alpha_2}^l \tau_{\alpha_2 \alpha_1}^k \left[\text{sign}(V_{\alpha_1})(1 - \delta_{\alpha_1 \alpha_2}) \right] L^{2l} \left(L^{1k} + L^{3k} \right)$$

$$\tag{6.147}$$

$$= J_l J_k V \sum_{\substack{l \neq k \\ l,k = x,y,z}} \left[\text{sign}(V_2) \tau_{21}^l \tau_{12}^k + \text{sign}(V_1) \tau_{12}^l \tau_{21}^k \right] L^{2l} \left(L^{1k} + L^{3k} \right)$$

$$= \left(J_z J_\perp \right) V L^{3x},$$

which satisfies $\text{Tr}_S(L^{3x}) = 0$ as well. Next we discuss the correction terms proportional to $\bar{G}_{12} | E + \mu_{12} - L_{\text{ns}} | \bar{G}_{\bar{2}\bar{1}}$. We know that $\Gamma_0 \ll h$ which means that the perturbative corrections to the roots of the unperturbed Liovillian L_{ns} are small. We can thus safely assume $\lambda_\pm^* = L_{\text{eff}}(\lambda_\pm^*) \simeq \pm h$. As such we evaluate the correction terms

proportional to $\bar{G}_{12}|E + \mu_{12} - L_{\text{ns}}|\bar{G}_{\bar{2}\bar{1}}$ for $E \simeq \pm h$ and obtain

$$\bar{G}_{12}|h + \mu_{12} - L_{\text{ns}}|\bar{G}_{\bar{2}\bar{1}} = J_l J_k \sum_{\substack{\alpha_1,\alpha_2=1,2 \\ l,k=x,y,z}} \tau^l_{\alpha_1\alpha_2} \tau^k_{\alpha_2\alpha_1} L^{2l} \left|h - L_{\text{ns}} + \eta_1 V_{\alpha_1} + \eta_2 V_{\alpha_2}\right| L^{2k}$$

(6.148)

$$\begin{aligned}
=& \frac{J_\perp^2}{4} \left(|h + V| + |h - V|\right) L^6_+ + \frac{J_\perp^2}{2} |h| L^6_- \\
&+ \frac{J_\perp^2}{4} \left(2|\delta h| + |\delta h + V| + |\delta h - V|\right) \left(L^a - L^c\right) \\
&+ \frac{J_\perp^2}{4} \left(2|2h| + |2h + V| + |2h - V|\right) \left(L^a - L^c\right) \\
&+ \frac{J_\perp J_z}{4} \left(|\delta h + V| - |\delta h - V|\right) \left(L^4_- + L^5_+\right) \\
&+ \frac{J_\perp J_z}{4} \left(|2h + V| - |2h - V|\right) \left(L^4_+ + L^5_-\right) \\
&+ \frac{J_z^2}{4} \left(|\delta h + V| + |\delta h - V|\right) \left(L^c + L^h\right) \\
&+ \frac{J_z^2}{4} \left(|2h + V| + |2h - V|\right) \left(L^c - L^h\right) ,
\end{aligned}$$

where $\delta h = h - h_0$ and we verify that $\text{Tr}_S(L^4_\pm) = \text{Tr}_S(L^5_\pm) = \text{Tr}_S(L^6_\pm) = 0$. Lastly we discuss the correction term that involves the logarithm of the Liouvillian L_{ns}. We abbreviate $z = E + \mu_{12} - L_{\text{ns}}$ and approximate $E = \pm h$. The correction term then

evaluates to

$$\bar{G}_{12} z \log \left| \frac{2z}{D} \right| \bar{G}_{\bar{2}\bar{1}} \tag{6.149}$$

$$= \frac{J_\perp^2}{4} h \log \left| \frac{2h}{D} \right| L_-^6$$

$$+ \frac{J_\perp^2}{4} \left((h+V) \log \left| \frac{2(h+V)}{D} \right| + (h-V) \log \left| \frac{2(h-V)}{D} \right| \right) L_+^6$$

$$+ \frac{J_\perp^2}{4} \left(\delta h \log \left| \frac{2\delta h}{D} \right| + (2h) \log \left| \frac{4h}{D} \right| \right) \left(L^a - L^c \right)$$

$$+ \frac{J_z^2}{4} \left((\delta h + V) \log \left| \frac{2(\delta h + V)}{D} \right| + (\delta h - V) \log \left| \frac{2(\delta h - V)}{D} \right| \right) \left(L^c + L^h \right)$$

$$+ \frac{J_z^2}{4} \left((2h + V) \log \left| \frac{2(2h + V)}{D} \right| + (2h - V) \log \left| \frac{2(2h - V)}{D} \right| \right) \left(L^c - L^h \right)$$

$$+ \frac{J_z J_\perp}{4} \left((\delta h + V) \log \left| \frac{2(\delta h + V)}{D} \right| - (\delta h - V) \log \left| \frac{2(\delta h - V)}{D} \right| \right) \left(L_-^4 + L_+^5 \right)$$

$$+ \frac{J_z J_\perp}{4} \left((2h + V) \log \left| \frac{2(2h + V)}{D} \right| - (2h - V) \log \left| \frac{2(2h - V)}{D} \right| \right) \left(L_+^4 + L_-^5 \right)$$

$$+ \frac{J_\perp^2}{4} \left((\delta h + V) \log \left| \frac{2(\delta h + V)}{D} \right| + (\delta h - V) \log \left| \frac{2(\delta h - V)}{D} \right| \right) \left(L^a - L^c \right)$$

$$+ \frac{J_\perp^2}{4} \left((2h + V) \log \left| \frac{2(2h + V)}{D} \right| + (2h - V) \log \left| \frac{2(2h - V)}{D} \right| \right) \left(L^a - L^c \right).$$

With all the self-energy terms evaluated we can determine the eigenvalues of the effective Liouvillian $L_{\text{eff}}(E)$. To obtain an analytical result for the roots $\pm h$ we perform the diagonalization of L_{eff} perturbatively as well. In first order

$$h^{(1)} = (\uparrow\downarrow \, |L_{\text{eff}}(h)| \, \uparrow\downarrow) = -(\downarrow\uparrow \, |L_{\text{eff}}(-h)| \, \downarrow\uparrow), \tag{6.150}$$

we find

$$h = h_0 + \frac{1}{4}\left[-2\left(J_\perp^2 h + J_z^2 \delta h\right) + \frac{J_\perp^2}{2}h\log\left|\frac{2h}{D}\right| \right. \tag{6.151}$$

$$+ \frac{J_\perp^2}{2}\left((h+V)\log\left|\frac{2(h+V)}{D}\right| + (h-V)\log\left|\frac{2(h-V)}{D}\right|\right)$$

$$+ J_z^2\left((\delta h+V)\log\left|\frac{2(\delta h+V)}{D}\right| + (\delta h-V)\log\left|\frac{2(\delta h-V)}{D}\right|\right)$$

$$\left. -i\frac{\pi}{4}J_\perp^2\left(|h+V| + |h-V| + 2|h|\right) - i\frac{\pi}{2}J_z^2\left(|\delta h+V| + |\delta h-V|\right)\right] ,$$

where $\delta h = h - h_0 \simeq 0$ and h_0 denotes the root of the bare Liouvillian L_{ns}. The imaginary part of the root h, which corresponds to its transient decay rate, reads

$$\mathrm{Im}(h) \simeq -i\frac{\pi}{16}J_\perp^2\left(|h+V| + |h-V| + 2|h|\right) - i\frac{\pi}{8}J_z^2\left(|\delta h+V| + |\delta h-V|\right) . \tag{6.152}$$

We see that for $V \to 0$ the imaginary part of h is essentially given by the terms proportional to $J_\perp^2$. For $V = 0$ we thus find a power law decrease of the decay rate with $U^{-\alpha}$ and $\alpha \geq 8$. For finite bias voltage and $U \to \infty$ the terms proportional to J_z^2 become dominant and we observe a power law decrease of the decay rate with $U^{-\beta}$ and $\beta = 6$. In figure 6.12 we plot our numerical results for the decay rates $\mathrm{Im}(\lambda_\pm^*)$ with $\lambda_\pm^* = \pm h$. We find that for $V = 0$ the decay rates obey a power law, $\mathrm{Im}(\lambda_\pm^*)(U) \propto U^{-8}$, the same as the spin-flip interaction $J_\perp^2(U)$. For finite bias voltage we observe a different power law, $\mathrm{Im}(\lambda_\pm^*)(U) \propto U^{-6}$, a behavior shared by $J_z^2(U)$. Our numerical findings support our perturbative result for the decay rates (6.152). The perturbation theory for the effective model finds that $\Gamma \to 0$ for $U \to \infty$ and supports our findings from DMRG calculations and perturbation theory in the limit of small coupling which see very long life times $\tau \gg \Gamma_0^{-1}$ of the ring current oscillations.

6.5 Estimates for the experimental observation of the current oscillation

In the presence of a periodically oscillating current density $\mathbf{j}(\mathbf{x}, t) = \mathbf{j}(\mathbf{x})e^{i\varepsilon t}$ one finds an associated periodic electromagnetic potential

$$\mathbf{A}(\mathbf{x}, \omega = \varepsilon) = \frac{\mu_0}{4\pi}\int \mathbf{j}(\mathbf{x}')\frac{e^{ik|\mathbf{x}-\mathbf{x}'|}}{|\mathbf{x}-\mathbf{x}'|}d^3x' , \tag{6.153}$$
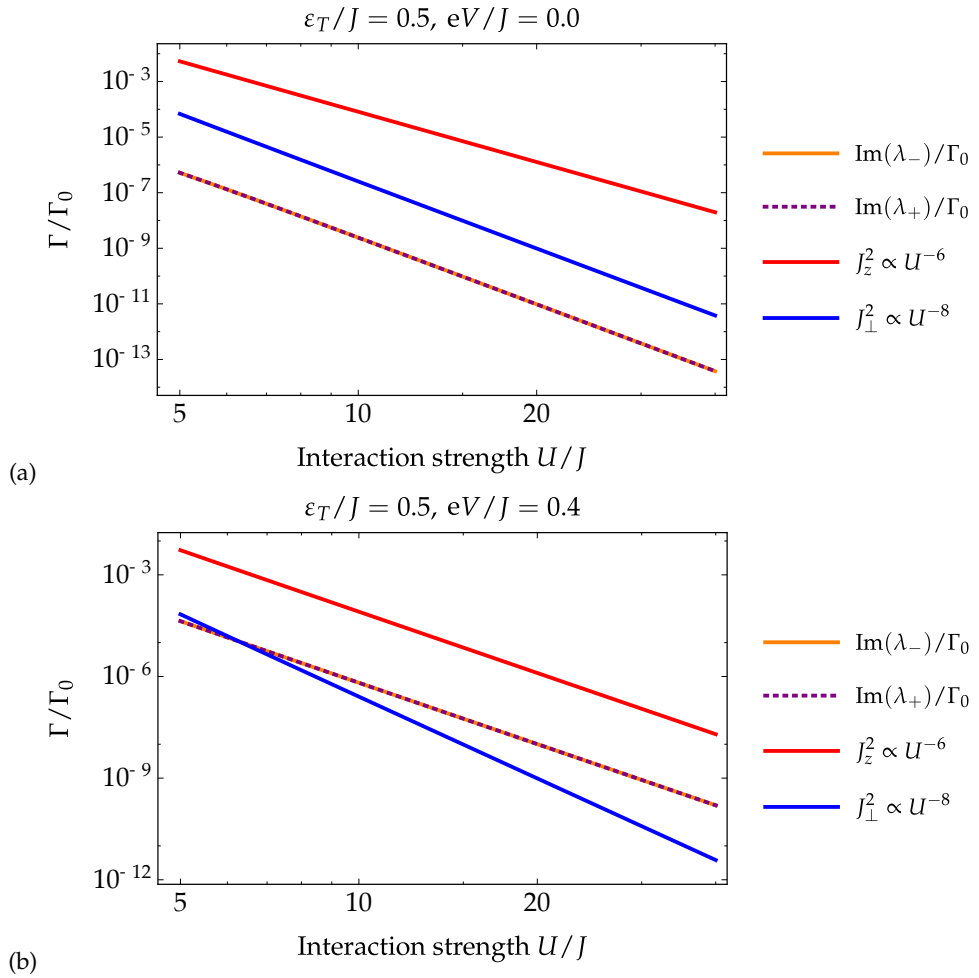
Figure 6.12: *Decay rate Γ/Γ_0 of the roots λ_+ and λ_- for (a): $\varepsilon_T/J = 0.5$, $J_c/J = 0.5$, $eV/J = 0$ and (b): $\varepsilon_T/J = 0.5$, $J_c/J = 0.5$, $eV/J = 0.4$.*

where the wavenumber $k = \varepsilon/\hbar c$ is directly proportional to the oscillation frequency and μ_0 denotes the magnetic vacuum permeability. Next, we perform a multipole expansion in the radiation zone $d \ll 2\pi/k \ll r$, where d denotes the radius of the nano-ring, and r is the distance from the nanostructure. The first term in the multipole expansion is proportional to the electric dipole moment. The electric dipole moment reads

$$\mathbf{p} = \int \mathbf{x}\rho(\mathbf{x})\,d^3x = q\int \mathbf{x}\delta(|\mathbf{x}| - d)\,d^3x \equiv 0, \tag{6.154}$$

which is zero, due to an equally distributed charge density at radius d.

Magnetic dipole moment   The first non-vanishing contribution to the multipole expansion derives from the magnetic dipole moment, which is given by

$$|\mathbf{m}| = \frac{1}{2}\int \mathbf{x} \times \mathbf{j}(\mathbf{x})\,d^3x = \frac{I\pi d^2}{2}, \tag{6.155}$$

where I is the amplitude of the oscillating ring current. In the following we choose $I \leq 10^{-2} \times Je/h$, which is approximately the amplitude of the oscillating ring current for system parameters $U/J = 4.0$, $\varepsilon_T/J = 0.5$, $J_c/J = 0.5$ and $eV/J = 0.4$, as can be seen in figure 5.2. The magnetic dipole contribution to the electromagnetic potential at distance r reads

$$|A(r)| = \frac{ik\mu_0}{4\pi}|\mathbf{m}|\frac{e^{ikr}}{r}\left(1 - \frac{1}{ikr}\right), \tag{6.156}$$

and the resulting magnetic and electric fields are given by

$$|H(r)| = \frac{k^2|\mathbf{m}|}{4\pi}\frac{e^{ikr}}{r}, \tag{6.157}$$

$$|E(r)| = \frac{Z_0 k^2|\mathbf{m}|}{4\pi}\frac{e^{ikr}}{r}, \tag{6.158}$$

where $Z_0 = 1/(\varepsilon_0 c) \approx 377\,\Omega$ denotes the impedance of the vacuum. The total power radiated by the electric and magnetic fields, that derive from the magnetic dipole moment, is consequently given by

$$P = 2\pi r^2|E(r)||H(r)| \tag{6.159}$$

$$= \frac{Z_0 k^4|\mathbf{m}|^2}{12\pi}.$$

For an experimental observation, one would require that the power P, radiated by the fields, integrated over the duration of the oscillation lifetime Γ^{-1} exceeds the energy necessary to emit a photon with the energy $E = \varepsilon$, indicative of the ring current oscillation. This requirement can be expressed as

$$\frac{\hbar P}{\Gamma} \overset{!}{>} \varepsilon. \tag{6.160}$$

In the following, we will express parameters in dimensionless multiples of the Rydberg energy in the case of energies, ie $\varepsilon \to \varepsilon \times \text{Ry}$ and multiples of the Bohr radius a_0 in the case of length scales. In the chosen units, the requirement reads

$$1 \overset{!}{<} \frac{P}{\Gamma\varepsilon} \frac{\hbar}{\text{Ry}^2} \tag{6.161}$$

$$= \frac{\pi}{48} \frac{1}{\Gamma\varepsilon} \frac{\hbar}{\text{Ry}^2} \frac{8\pi\text{Ry}a_0}{e^2 c} \varepsilon^4 \left(\frac{\text{Ry}}{c\hbar}\right)^4 (10^{-2}J)^2 \left(\frac{\text{Rye}}{2\pi\hbar}\right)^2 d^4 a_0^4$$

$$= \frac{(10^{-2})^2 J^2 d^4 \varepsilon^3}{24\Gamma} \frac{\text{Ry}^5 a_0^5}{\hbar^5 c^5} .$$

The requirement for the parameters of an experimental realization of our model system then reads

$$\frac{J^2 d^4 \varepsilon^3}{\Gamma} \overset{!}{>} 2.4 \times 10^{18} . \tag{6.162}$$

Our calculations have been performed with J and ε_T chosen to be of the same order of magnitude, such that $\varepsilon_T \leq D \simeq 2J$. In graphene the corresponding parameters are known to be $J = 0.22\,\text{Ry}$ and $d = 2.84\,a_0$. An optimistic guess for a set of parameters, which could collectively be achieved in an experiment, is $d \approx 10\,a_0$, $J \approx \text{Ry}$ and $\Gamma/J \approx 10^{-10}$ for a chosen coupling $J_c \ll J$. Using these parameters, we find

$$\frac{(J \approx 1)^2 (d \approx 10)^4 (\varepsilon \approx 1)^3}{(\Gamma \approx 10^{-10})} = 10^{14} \ll 2.4 \times 10^{18} , \tag{6.163}$$

which leads us to believe that it is unlikely to find a system, in which the oscillation can be experimentally observed through the energy radiated by the dipole field alone. Increases in radius d will most likely result in decreased energy scales J and ε.

Electric quadrupole moment The sub-leading contribution to the multipole expansion of the electromagnetic potential is given by the terms proportional to the electric quadrupole moment. The quadrupole moment tensor is defined as

$$Q_{\alpha,\beta} = \int d^3 x \left(3x_\alpha x_\beta - r^2 \delta_{\alpha,\beta}\right) \rho(\mathbf{x}) = q \int d^3 x \left(3x_\alpha x_\beta - r^2 \delta_{\alpha,\beta}\right) \delta(r - d) . \tag{6.164}$$

The power radiated by the electric and magnetic fields, which originate from the electric quadrupole moment, reads

$$P = \frac{c^2 Z_0 k^6}{1440\pi} \sum_{\alpha,\beta} |Q_{\alpha,\beta}|^2 , \tag{6.165}$$

where the absolute value square of the quadrupole tensor yields

$$\sum_{\alpha,\beta} |Q_{\alpha\beta}|^2 = \frac{3}{2} q^2 d^4 . \tag{6.166}$$

Our requirement for the parameters of the experimental setup thus becomes

$$\frac{\hbar P}{\Gamma \varepsilon} = \frac{1}{120} \frac{\varepsilon^5 q^2 d^4}{\Gamma} \left(\frac{\mathrm{Ry}^5 a_0^5}{c^5 \hbar^5} \right) \overset{!}{>} 1 \, . \tag{6.167}$$

When we use the same estimates for the system parameters as in the case of the dipole fields, we find

$$\frac{(\varepsilon \approx 1)^5 (q \approx 2)^2 (d \approx 10)^4}{(\Gamma \approx 10^{-10})} = 4 \times 10^{14} \leq 1.2 \times 10^{15} \, , \tag{6.168}$$

which is of comparable order of magnitude, meaning that it is realistic to have a photon of energy $E = \varepsilon$ emitted by the quadrupole fields in a significant fraction of the measurements. The energy radiated by the dipole and quadrupole fields combined thus appears sufficient for a possible detection in an experiment.

Chapter 7

7 Summary and Outlook

In this dissertation, we have looked into various aspects - mainly the non-equilibrium dynamics - of different model systems, all of which belong to the category of strongly correlated, low-dimensional, many-body quantum systems. In the following, we would like to summarize our research and address open questions that arise from it.

Summary

In chapter 3, we have studied the effect of an open boundary on the spectral properties of microscopic models, which realize one-dimensional Mott insulators, in order to complement previous field theoretical work [108]. Specifically, we have calculated the local density of states (LDOS) and its Fourier transform for the one-dimensional Fermi-Hubbard chain and an extension featuring next-nearest neighbor interaction. The low-energy properties of both these models are described by the massive Thirring theory and because the regular Hubbard model is exactly solvable by Bethe ansatz [31], we have been able to compare our numerical findings to the field theory ones, both qualitatively and quantitatively. We also studied the effect of a chemical potential at the boundary on the LDOS of the Hubbard chain. To obtain these local densities of states, we applied a density matrix renormalization group algorithm, within which we calculated the local retarded Green function in frequency space using an expansion of the occuring resolvent in terms of Chebyshev polynomials. This approach allowed us to reduce the artificial broadening necessary for the numerical study of finite systems. Our numerical results for the LDOS reproduce the Mott gap and its width is found to be in excellent agreement with the Bethe ansatz result for the Hubbard model. In the Fourier transform of the LDOS, we detect several gapped and gapless dispersing modes with distinct velocities matching the analytical results for the distinctive spinon and holon velocities that cause spin-charge separation. Our observations are in excellent agreement with the results from field theory at low energies. On top of that, we find additional dispersing modes at higher energies. For sufficiently large boundary chemical potentials, we also recognize boundary bound states, which manifest themselves as non-dispersing features

in the LDOS. We conclude that spin-charge separation can be observed in the Fourier transform of the LDOS and thus directly measured using scanning tunneling spectroscopy.

In the work presented in chapter 4, we have examined the extent to which the non-equilibrium dynamics of a strongly correlated one-dimensional system differ, if the non-equilibrium situation is brought about by a quench of finite duration instead of a sudden quench. In such a setup, the inverse quench duration τ^{-1} appears as an additional characteristic energy scale of the system. As model system we we have chosen the critical XXZ Heisenberg chain. In equilibrium, the low-energy description of the XXZ chain is given by the Tomonaga-Luttinger model. We have performed the time evolution of the XXZ chain for short and intermediate times after the quench using time-dependent DMRG and have computed the equal-time spin-spin correlation functions. For sudden quenches, our results support the observation by Collura et al. [170] that the dynamics of the correlation functions are captured by the Tomonaga Luttinger model to a relatively good degree even in non-equilibrium. For finite duration quenches, our results show that the light cone picture for correlation functions after a quantum quench, which was proposed by Calabrese and Cardy [173], remains applicable. The light-cone front after finite duration quenches exhibits a non-zero delay when compared to sudden quenches, This delay derives from a continous excitation of quasi-particles at the respective instanteous velocities during the quench. The extent of the light-cone front delay, that we observe in our numerical results, agrees well with previous analytical calculations for the Galilean invariant Tomonaga-Luttinger model[169].

Chapter 5 contains our work on the non-equilibrium dynamics in interacting, asymmetric, ring-shaped nanostructures containing spinless fermions and coupled to metallic leads. These models have been previously proposed to study the quantum-interference effects in functionalized graphene ribbons [177]. Here, we have studied the transient currents flowing in the nanostructure after a bias voltage quench. Our calculations have shown that the source-to-drain current relaxes to its steady state with a decay rate Γ_0 equal to energy level broadening induced by the leads. The local currents circulating in the impurity, on the other hand, continue to oscillate with a distinct frequency ω well beyond the time scale Γ_0^{-1}, rather exhibiting a decay rate Γ that quickly decreases with increasing interaction strength. Exact diagonalization calculations of the impurity Hamiltonian have revealed that the oscillation frequency ω corresponds to the energy gap between two charge density wave (CDW) states inside the impurity. In the limit of small impurity-lead hybridization Γ_0, we have found that the decay rate Γ becomes small due to an increased suppression of decay channels with growing interaction strength. As a result of a mirror symmetry of the impurity, the effective low-energy theory for the two CDW states exhibits an anisotropic Kondo-like coupling between the impurity and the leads, which is also strongly diminished for increasing interaction strength. Our calculations for this effective model have identified that the decay rate Γ of the oscillating currents falls off as a power law of the interaction strength, which is consistent with the numerical

results. On the basis of these calculations, we have concluded that the two observable currents in the system approach their equilibrium values on time scales that are parametrically separated with rates differing by orders of magnitude. Finite interactions can thus produce a situation, in which the transport currrent appears to have relaxed to the steady states, while the local currents still remain in the transient regime.

Outlook

In chapter 4, we have demonstrated that the transverse correlation functions of the XXZ Heisenberg chain continue to be adequately described by a Tomonaga-Luttinger model, even after a quantum quench. This is surprising, given the extensive amount of energy deposited in the system by the quench and the fact that even in equilibrium, the Tomonaga-Luttinger model describes only the low-energy behavior of the microscopic model.

In our setup, both the initial microscopic system and the microscopic system after the quench have been quantum critical and would thus be individually described by a Tomonaga-Luttinger model in equilibrium. In the discussed case, the only qualitative difference between the response of the system to either a sudden quench or a finite duration quench, for $t \gg \tau$, appears to be the non-zero delay of the light-cone front.

It remains an unexplored question, whether the two types of quenches lead to fundamentally different situations, if the quench takes the system across a quantum phase transition. In such a case, a finite duration quench would excite both massless and massive quasi-particles, whereas excitations due to a sudden quench should be limited to a single type.

More fundamentally, the extent to which Luttinger liquid theory is applicable, if either the initial system or the final system features an excitation gap, remains an issue to be studied.

Lastly, we note that the non-equilibrium benchmarks of Luttinger liquid theory have so far been limited to the XXZ Heisenberg chain. Yet, it cannot be ruled out that for other microscopic models in the Luttinger Liquid universality class, certain processes, which are known to be irrelevant in equilibrium, can become marginal or even relevant in non-equilibrium.

Our analysis of the local currents inside interacting ring-shaped nanostructures, presented in chapter 5, was originally motivated by Density Functional Theory studies of transport currents in impurity doped graphene nanoribbons. Now that the peculiar transient behavior of the local currents in a single nanoring with impurity is sufficiently understood, the logical next step would be to examine the properties of lattices of such nanostructures.

To make direct contact with graphene nanoribbons though, one first needs to acquire an understanding of the impurity doped hexagonal nanostructure, for which the important mirror symmetry left $\leftrightarrow$ right is broken. Early computations of the

time-dependent currents in such a system reveal similar transient features as seen for the quadratic ring, but also display significant differences, particularly in the time-dependent transport current. Given the richness of the physics of the quadratic ring system, we expect a multitude of surprising results from a detailed study of the hexagonal ring.

8 Chapter 8
Nederlandse samenvatting

De dimensionaliteit van kwantummechanische veeldeeltjessystemen is van cruciaal belang voor het bepalen van hun eigenschappen. In drie dimensies zijn gemiddelde veldentheorieën of semiklassieke methoden vaak voldoende om dit soort systemen te bestuderen en leiden kwantumfluctuaties alleen tot kleine correcties. In lagere dimensies zijn de effecten van kwantumfluctuaties groter, zodat deze fluctuaties leiden tot nieuwe exotische fenomenen en gemiddelde veldentheorieën ontoereikend worden. In één dimensie, bijvoorbeeld, werkt het Fermivloeistofbeeld van excitaties van quasideeltjes die zich gedragen als vrije elektronen met een gecorrigeerde massa niet meer. Het Fermivloeistofbeeld wordt in dit geval vervangen door het Luttinger-vloeistofbeeld, waarin excitaties van quasideeltjes lijken op dichtheidsgolven.

Naast interessante nieuwe natuurkunde maakt de beperking tot lagere dimensies ook een breed scala aan krachtige analytische en numerieke methoden mogelijk. Met deze methoden is het mogelijk om deze systemen te bestuderen met een hoge nauwkeurigheid en in het geval van integreerbare system zelfs op exacte wijze [8]. In dit proefschrift hebben we gekeken naar verschillende aspecten - vooral de niet-evenwichtsdynamica - van verschillende modelsystemen, welke allemaal behoren tot de categorie sterk interagerende, één- of nuldimensionale, kwantummechanische veeldeeltjessystemen. We zullen nu het onderzoek in dit proefschrift samenvatten.

In Hoofdstuk 3 hebben we de effecten bestudeerd van een open rand op de spectrale eigenschappen van microscopische modellen die ééndimensionale Mott-isolatoren verwezenlijken. Het doel van dit onderzoek was om recent veldtheoretisch werk aan te vullen [108]. Om specifieker te zijn, hebben we de lokale toestandsdichtheid (LDOS) berekend, alsmede haar Fouriertransformatie, voor de ééndimensionale Fermi-Hubbardketting en een uitbreiding met interacties tussen buren alsmede tussen buren van buren. De laag-energetische eigenschappen van deze beide modellen worden beschreven door de massieve Thirringtheorie. Doordat het reguliere Hubbardmodel exact oplosbaar is met behulp van de Bethe ansatz [31], hebben we onze numerieke resultaten zowel op kwantitatieve als op kwalitatieve wijze kunnen

vergelijken met de veldtheoretische resultaten. Daarnaast hebben we het effect van een chemische potentiaal op de rand op de LDOS van de Hubbardketting bestudeerd. Om de lokale dichtheidstoestanden te verkrijgen, hebben we een zogenaamd dichtheidsmatrix renormalizatiegroep (DMRG) algoritme gebruikt. Hiermee hebben we de lokale geretardeerde Greense functie in de frequentieruimte berekend, gebruik makend van een expansie van de bijbehorende resolvente in termen van Chebyshev polynomen. Deze aanpak heeft ons in staat gesteld om de kunstmatige verbreding te verminderen, hetgeen noodzakelijk is voor een numerieke studie van eindige systemen. Onze numerieke resultaten voor de LDOS reproduceren de Mott bandkloof. Daarnaast is de gevonden breedte van de bandkloof in uitstekende overeenstemming met het resultaat van de Bethe ansatz toegepast op het Hubbardmodel. In de Fouriertransformatie van de LDOS hebben we verschillende gekloofde en ongekloofde toestanden gevonden. De dispersies van deze toestanden hebben verschillende snelheden, die overeenkomen met de analytische resultaten voor de zogenaamde spinon- en holonsnelheden die voor spin-ladingscheiding zorgen, wanneer ze niet gelijk zijn. Onze waarnemingen komen uitstekend overeen met de resultaten van veldtheoretische berekeningen op lage energieën. We vinden bovendien extra toestanden met een dispersie op hogere energieën. Voor voldoende grote chemische potentialen op de rand herkennen we ook gebonden randtoestanden die zichzelf manifesteren als dispersieloze kenmerken in de LDOS. We concluderen dat spin-ladingscheiding geobserveerd kan worden in de Fouriertransformatie van de LDOS en dus gemeten kan worden door gebruik te maken van zogenaamde scannende tunnelspectroscopie.

In het werk dat we presenteren in Hoofdstuk 4 hebben we gekeken naar de niet-evenwichtsdynamica van een sterk-interagerend ééndimensionaal syteem. In het bijzonder hebben we gekeken naar het verschil tussen het totstand komen van een niet-evenwichtssituatie door een zogenaamde plotselinge 'quench' met een oneindig korte duur en een quench met een eindige duur. In een dergelijke situatie speelt de inverse quench-duur τ^{-1} de rol van een nieuwe energieschaal in het systeem. Als modelsysteem hebben we de kritische XXZ-Heisenbergketen gekozen. In evenwicht wordt de laag-energetische beschrijving van de XXZ-ketting gegeven door het Tomonaga-Luttingermodel, welke het meest fundamentele model van de Luttinger-vloeistof is. We hebben de tijdsevolutie van de XXZ-keten uitgerekend voor korte en tussenliggende tijden na de quench. Hiervoor hebben we gebruik gemaakt van tijds-afhankelijke DMRG en hebben we ook de gelijktijdige spin-spin correlatiefuncties berekend. Voor plotselinge quenches bevestigen onze resulaten de waarnemingen van Collura et al. [170]. De dynamica van de correlatiefuncties blijkt relatief goed te worden beschreven door het Tomonoga-Luttingermodel, zelfs als er nog geen evenwicht tot stand gekomen is. Voor quenches met een eindige duur laten onze resulaten zien dat het lichtkegelbeeld voor correlatiefuncties na een quench, voorgesteld door Calabrese and Cardy [173], toepasbaar blijft. Het front van de lichtkegel na een quench van eindige duur laat een eindige vertraging zien vergeleken met de plotselinge quenches. Deze vertraging is het resultaat van het continu exciteren van quasideeltjes op de bijbehorende instantane snelheden gedurende de quench.

De omvang van de vertraging van het front van de lichtkegel die we observeren in onze numerieke simulaties komt goed overeen met analytische berekeningen aan een Tomonaga-Luttingermodel met Galileaanse invariantie [169].

Hoofdstuk 5 bevat ons werk aan de niet-evenwichtsdynamica van interagerende, asymmetrische, ringvormige nanostructuren, die spinloze fermionen bevatten en gekoppeld zijn aan metaalachtige contacten. Dit soort modellen is recentelijk voorgesteld om de kwantuminterferentie-effecten in gefunctionaliseerde grafeenlinten te bestuderen [177]. Hier hebben we de kortstondige stromen bestudeerd die in de nanostructuur lopen na een quench in het biasvoltage. Onze berekeningen laten zien dat de stroom die van de bron naar de afvoer loopt, relaxeert naar een evenwichtstoestand met een vervalsnelheid Γ_0 die gelijk is aan de verbreding van de energieniveaus door de contacten. Aan de andere kant circuleert de stroom in de onzuiverheid met een frequentie ω, op tijdsschalen lang na Γ_0^{-1}. De corresponderende vervalsnelheid Γ blijkt snel af te nemen als de interactiesterkte toeneemt. Exacte diagonalisatie van de Hamiltoniaan van de onzuiverheid heeft onthuld dat de oscillatiefrequentie ω correspondeert met de energiekloof tussen twee toestanden van ladingsdichtheidsgolven (CDW) in de onzuiverheid. In de limiet van een kleine hybridisatie Γ_0 tussen de onzuiverheid en de contacten vinden we dat de vervalsnelheid Γ klein wordt door een toenemende onderdrukking van de vervalkanalen als de interactiesterkte groeit. Ten gevolge van de spiegelsymmetrie van de onzuiverheid bevat de laag-energetische theorie voor de twee CDW-toestanden een anisotrope Kondo-achtige koppeling tussen de onzuiverheid en de contacten, welke ook sterk afneemt voor toenemende interactiesterktes. Onze berekeningen aan dit effectieve model hebben laten zien dat de vervalsnelheid Γ van de oscillerende stromen afneemt als een macht van de interactiesterkte, hetgeen consistent is met de numerieke resultaten. Gebaseerd op deze berekeningen hebben we geconcludeerd dat de twee observeerbare stromen in het systeem hun evenwichtswaardes bereiken op tijdsschalen die parametrisch gescheiden zijn met vervalsnelheden die ordes van grootte verschillen. Eindige interacties kunnen dus een situatie teweegbrengen waarin het lijkt alsof de transportstroom al naar de evenwichtstoestand is gerelaxeerd, terwijl de lokale stromen zich nog in het overgangsgebied bevinden.

Bibliography

[1] A. Yacoby, H. L. Stormer, Ned S. Wingreen, L. N. Pfeiffer, K. W. Baldwin, and K. W. West. *Nonuniversal Conductance Quantization in Quantum Wires.* Phys. Rev. Lett. **77**, 4612, (1996).

[2] A. Yacoby, H.L. Stormer, K.W. Baldwin, L.N. Pfeiffer, and K.W. West. *Magneto-transport spectroscopy on a quantum wire.* Solid State Communications, **101**, 77, (1997).

[3] Yaroslav Tserkovnyak, Bertrand I. Halperin, Ophir M. Auslaender, and Amir Yacoby. *Interference and zero-bias anomaly in tunneling between Luttinger-liquid wires*. Phys. Rev. B, **68**, 125312, (2003).

[4] Xiao-Gang Wen. *Theory of the edge states in fractional quantum hall effects*. Int. J. Mod. Phys. B, **06**, 1711, (1992).

[5] D. Jérome. *Organic superconductors.* Solid State Communications, **92**, 89, (1994).

[6] Sumio Iijima. *Helical microtubules of graphitic carbon.* Nature, **354**, 6348, (1991).

[7] Rufan Zhang, Yingying Zhang, Qiang Zhang, Huanhuan Xie, Weizhong Qian, and Fei Wei. *Growth of Half-Meter Long Carbon Nanotubes Based on Schulz–Flory Distribution.* ACS Nano, **7**, 6156, (2013).

[8] Thierry Giamarchi. *Quantum Physics in One Dimension*. Clarendon Press,(2003).

[9] M. H. Anderson, J. R. Ensher, M. R. Matthews, C. E. Wieman, and E. A. Cornell. *Observation of Bose-Einstein Condensation in a Dilute Atomic Vapor.* Science, **269**, 5221, (1995).

[10] Richard P. Feynman. *Simulating physics with computers.* Int J Theor Phys, **21**, 467, (1982).

[11] D. Jaksch, C. Bruder, J. I. Cirac, C. W. Gardiner, and P. Zoller. *Cold Bosonic Atoms in Optical Lattices.* Phys. Rev. Lett., **81**, 3108, (1998).

[12] Immanuel Bloch. *Quantum simulations come of age.* Nature Physics, **14**, 1159, (2018).

[13] Markus Greiner, Olaf Mandel, Tilman Esslinger, Theodor W. Hänsch, and Immanuel Bloch. *Quantum phase transition from a superfluid to a Mott insulator in a gas of ultracold atoms.* Nature, **415**, 6867, (2002).

[14] E. Tiesinga, B. J. Verhaar, and H. T. C. Stoof. *Threshold and resonance phenomena in ultracold ground-state collisions.* Phys. Rev. A, **47**, 4114, (1993).

[15] R. A. Duine and H. T. C. Stoof. *Atom–molecule coherence in Bose gases.* Physics Reports, **396**, 115, (2004).

[16] Philip W. Anderson and Robert Schrieffer. *A Dialogue on the Theory of High Tc.* Physics Today, **44**, 54, (2008).

[17] A. Recati, P. O. Fedichev, W. Zwerger, and P. Zoller. *Spin-Charge Separation in Ultracold Quantum Gases.* Phys. Rev. Lett., **90**, 020401, (2003).

[18] Maciej Lewenstein, Anna Sanpera, Veronica Ahufinger, Bogdan Damski, Aditi Sen De, and Ujjwal Sen. *Ultracold atomic gases in optical lattices: mimicking condensed matter physics and beyond.* Advances in Physics, **56**, 243, (2007).

[19] Robert Jördens, Niels Strohmaier, Kenneth Günter, Henning Moritz, and Tilman Esslinger. *A Mott insulator of fermionic atoms in an optical lattice.* Nature, **455**, 204, (2008).

[20] Tilman Esslinger. *Fermi-Hubbard Physics with Atoms in an Optical Lattice.* Annu. Rev. Condens. Matter Phys., **1**, 129, (2010).

[21] Anton Mazurenko, Christie S. Chiu, Geoffrey Ji, Maxwell F. Parsons, Márton Kanász-Nagy, Richard Schmidt, Fabian Grusdt, Eugene Demler, Daniel Greif, and Markus Greiner. *A cold-atom Fermi–Hubbard antiferromagnet.* Nature, **545**, 7655, (2017).

[22] Immanuel Bloch, Jean Dalibard, and Sylvain Nascimbène. *Quantum simulations with ultracold quantum gases.* Nature Physics, **8**, 4, (2012).

[23] Christian Gross and Immanuel Bloch. *Quantum simulations with ultracold atoms in optical lattices.* Science, **357**, 6355, (2017).

[24] Toshiya Kinoshita, Trevor Wenger, and David S. Weiss. *A quantum Newton's cradle.* Nature, **440**, 7086, (2006).

[25] Marcos Rigol, Vanja Dunjko, Vladimir Yurovsky, and Maxim Olshanii. *Relaxation in a Completely Integrable Many-Body Quantum System: An Ab-Initio Study of the Dynamics of the Highly Excited States of 1d Lattice Hard-Core Bosons.* Phys. Rev. Lett., **98**, 5, (2007).

[26] R. van den Berg, B. Wouters, S. Eliëns, J. De Nardis, R. M. Konik, and J.-S. Caux. *Separation of Timescales in a Quantum Newton's Cradle.* Physical Review Letters, **116**, 225302, (2016).

[27] H. Bethe. *Zur Theorie der Metalle.* Z. Physik, **71**, 205, (1931).

[28] Andreas Klümper. *Integrability of quantum chains: theory and applications to the spin-1/2 XXZ chain.* arXiv:cond-mat/0502431, (2004).

[29] Rodney J. Baxter. *Exactly Solved Models in Statistical Mechanics*. Courier Corporation, (2007).

[30] V. E. Korepin, N. M. Bogoliubov, and A. G. Izergin. *Quantum Inverse Scattering Method and Correlation Functions*. Cambridge University Press, (1997).

[31] Fabian H. L. Essler. *The one-dimensional Hubbard model / F. H. L. Essler et al.* (2005).

[32] Sin-itiro Tomonaga. *Remarks on Bloch's Method of Sound Waves applied to Many-Fermion Problems.* Prog Theor Phys, **5**, 544, (1950).

[33] J. M. Luttinger. *An Exactly Soluble Model of a Many-Fermion System.* Journal of Mathematical Physics, **4**, 1154, (1963).

[34] F. D. M. Haldane. *Coupling between charge and spin degrees of freedom in the one-dimensional Fermi gas with backscattering.* J. Phys. C. Solid State Phys., **12**, 4791, (1979).

[35] F. D. M. Haldane. *General Relation of Correlation Exponents and Spectral Properties of One-Dimensional Fermi Systems: Application to the Anisotropic S-1/2 Heisenberg Chain.* Phys. Rev. Lett., **45**, 1358, (1980).

[36] F D M Haldane. *Effective Harmonic-Fluid Approach to Low-Energy Properties of One-Dimensional Quantum Fluids.* Phys. Rev. Lett., **47**, 4, (1981).

[37] Giuseppe Mussardo. *Statistical Field Theory: An Introduction to Exactly Solved Models in Statistical Physics*. OUP Oxford, (2009).

[38] Philippe Francesco, Pierre Mathieu, and David Senechal. *Conformal Field Theory*. Springer Science & Business Media, (2012).

[39] Kenneth G. Wilson. *The renormalization group: Critical phenomena and the Kondo problem.* Reviews of Modern Physics, **47**, 773, (1975).

[40] Steven R. White. *Density matrix formulation for quantum renormalization groups.* Phys. Rev. Lett., **69**, 2863, (1992).

[41] Jean-Sébastien Caux and Fabian H. L. Essler. *Time Evolution of Local Observables After Quenching to an Integrable Model.* Phys. Rev. Lett., **110**, 257203, (2013).

[42] Jean-Sébastien Caux. *The Quench Action.* arXiv:1603.04689 [cond-mat], (2016).

[43] M. B. Hastings. *Solving gapped Hamiltonians locally.* Phys. Rev. B, **73**, 085115, (2006).

[44] Michael M. Wolf, Frank Verstraete, Matthew B. Hastings, and J. Ignacio Cirac. *Area Laws in Quantum Systems: Mutual Information and Correlations.* Phys. Rev. Lett., **100**, 070502, (2008).

[45] Roman Orus. *Advances on Tensor Network Theory: Symmetries, Fermions, Entanglement, and Holography.* The European Physical Journal B, **87**, (2014).

[46] Philippe Corboz, Román Orús, Bela Bauer, and Guifré Vidal. *Simulation of strongly correlated fermions in two spatial dimensions with fermionic projected entangled-pair states.* Phys. Rev. B, **81**, 165104, (2010).

[47] U. Schollwöck. *The density-matrix renormalization group.* Rev. Mod. Phys., **77**, 259, (2005).

[48] J. Dukelsky, M. A. Martín-Delgado, T. Nishino, and G. Sierra. *Equivalence of the variational matrix product method and the density matrix renormalization group applied to spin chains.* EPL, **43**, 457, (1998).

[49] Henrik Bruus and Karsten Flensburg. *Many-body quantum theory in condensed matter physics*, Oxford University Press Oxford, 2004.

[50] W. Heisenberg. *Zur Theorie des Ferromagnetismus.* In Walter Blum, Helmut Rechenberg, and Hans-Peter Dürr, editors, Original Scientific Papers Wissenschaftliche Originalarbeiten, Werner Heisenberg Gesammelte Werke Collected Works, pages 580–597. Springer Berlin Heidelberg, Berlin, Heidelberg, (1985).

[51] F. Bloch. *Zur Theorie des Ferromagnetismus.* Z. Physik, **61**, 206, (1930).

[52] F. Bloch. *Zur Theorie des Austauschproblems und der Remanenzerscheinung der Ferromagnetika.* Z. Physik, **74**, 295, (1932).

[53] C. N. Yang and C. P. Yang. *One-Dimensional Chain of Anisotropic Spin-Spin Interactions. II. Properties of the Ground-State Energy Per Lattice Site for an Infinite System.* Phys. Rev., **150**, 327, (1966).

[54] N. N. Bogoljubov. *On a new method in the theory of superconductivity.* Nuovo Cim, **7**, 794, (1958).

[55] C. Kim, A. Y. Matsuura, Z.-X. Shen, N. Motoyama, H. Eisaki, S. Uchida, T. Tohyama, and S. Maekawa. *Observation of Spin-Charge Separation in One-Dimensional SrCuO2.* Phys. Rev. Lett., **77**, 4054, (1996).

[56] Anatoli Polkovnikov, Krishnendu Sengupta, Alessandro Silva, and Mukund Vengalattore. *Colloquium: Nonequilibrium dynamics of closed interacting quantum systems.* Rev. Mod. Phys., **83**, 863, (2011).

[57] Fabian H. L. Essler, Stefano Evangelisti, and Maurizio Fagotti. *Dynamical Correlations After a Quantum Quench.* Phys. Rev. Lett., **109**, 247206, (2012).

[58] Dirk Schuricht and Fabian H. L. Essler. *Dynamics in the Ising field theory after a quantum quench.* J. Stat. Mech., **2012**, 04017, (2012).

[59] Takeshi Fukuhara, Peter Schauss, Manuel Endres, Sebastian Hild, Marc Cheneau, Immanuel Bloch, and Christian Gross. *Microscopic observation of magnon bound states and their dynamics.* Nature, **502**, 7469, (2013).

[60] T. L. Nguyen, J. M. Raimond, C. Sayrin, R. Cortiñas, T. Cantat-Moltrecht, F. Assemat, I. Dotsenko, S. Gleyzes, S. Haroche, G. Roux, Th. Jolicoeur, and M. Brune. *Towards Quantum Simulation with Circular Rydberg Atoms.* Phys. Rev. X, **8**, 011032, (2018).

[61] Maurizio Fagotti and Fabian H. L. Essler. *Stationary behaviour of observables after a quantum quench in the spin-1/2 Heisenberg XXZ chain.* J. Stat. Mech., **2013**, 07012, (2013).

[62] B. Wouters, J. De Nardis, M. Brockmann, D. Fioretto, M. Rigol, and J.-S. Caux. *Quenching the Anisotropic Heisenberg Chain: Exact Solution and Generalized Gibbs Ensemble Predictions.* Phys. Rev. Lett., **113**, 117202, (2014).

[63] M. A. Cazalilla, A. F. Ho, and T. Giamarchi. *Interacting Bose gases in quasi-one-dimensional optical lattices.* New J. Phys., **8**, 158, (2006).

[64] Andreas M. Läuchli and Corinna Kollath. *Spreading of correlations and entanglement after a quench in the one-dimensional Bose-Hubbard model.* J. Stat. Mech., **2008**, 05018, (2008).

[65] Marc Cheneau, Peter Barmettler, Dario Poletti, Manuel Endres, Peter Schauss, Takeshi Fukuhara, Christian Gross, Immanuel Bloch, Corinna Kollath, and Stefan Kuhr. *Light-cone-like spreading of correlations in a quantum many-body system.* Nature, **481**, 484, (2012).

[66] Guifré Vidal. *Efficient Simulation of One-Dimensional Quantum Many-Body Systems.* Phys. Rev. Lett., **93**, 040502, (2004).

[67] Gene H. Golub and Charles F. Van Loan. *Matrix computations / Gene H. Golub ; Charles F. Van Loan.* (2013).

[68] C. Lanzcos. *An iteration method for the solution of the eigenvalue problem of linear differential and integral operators.* Journal of Research of the National Bureau of Standards, **45**, (1950).

[69] A. Björck. *Numerical Methods in Matrix Computations.* Springer International Publishing, (2015).

[70] H. Fehske, R. Schneider, and A. Weisse, editors. *Computational many-particle physics.* Number 739 in Lecture notes in physics. Springer, Berlin ; New York, (2008).

[71] Denis Serre. *Matrices*, volume 216 of *Graduate Texts in Mathematics*. Springer New York, New York, NY, (2010).

[72] G. W. Stewart. *Matrix Algorithms: Volume 1: Basic Decompositions.* SIAM, (1998).

[73] Carl Eckart and Gale Young. *The approximation of one matrix by another of lower rank.*

[74] Reinhard M. Noack and Salvatore R. Manmana. *Diagonalization- and Numerical Renormalization-Group-Based Methods for Interacting Quantum Systems.* arXiv:cond-mat/0510321, 789, (2005).

[75] Roman Orus and Guifre Vidal. *The iTEBD algorithm beyond unitary evolution.* Physical Review B, **78**, (2008).

[76] Ulrich Schollwöck. *Simulating Strongly Correlated Quantum Systems: Adaptive Time-Dependent Density-Matrix Renormalization Group.* CFN Lectures on Functional Nanostructures - Volume 2, volume 820, (2010).

[77] G. Vidal. *Classical Simulation of Infinite-Size Quantum Lattice Systems in One Spatial Dimension.* Phys. Rev. Lett., **98**, 070201, (2007).

[78] Jan von Delft and Herbert Schoeller. *Bosonization for Beginners — Refermionization for Experts.* Annalen der Physik, **7**, 225, (1998).

[79] V. Meden and K. Schönhammer. *Spectral functions for the Tomonaga-Luttinger model.* Physical review B, **46**, 15753, (1992).

[80] B. J. Kim et al., Nature Phys. **2**, 397, (2006).

[81] M. Grioni, S. Pons, and E. Frantzeskakis, J. Phys.: Condens. Matter **21**, 023201, (2009).

[82] M. Bockrath, D. H. Cobden, J. Lu, A. G. Rinzler, R. E. Smalley, L. Balents, and P. L. McRuen, Nature **397**, 598, (1999).

[83] O. M. Auslaender, H. Steinberg, A. Yacoby, Y. Tserkovnyak, B. I. Halperin, K. W. Baldwin, L. N. Pfeiffer, and K. W. West, Science **308**, 88, (2005).

[84] Y. Jompol, C. J. B. Ford, J. P. Griffiths, I. Farrer, G. A. C. Jones, D. Anderson, D. A. Ritchie, T. W. Silk, and A. J. Schofield, Science **325**, 597, (2009).

[85] J. Lee, S. Eggert, H. Kim, S.-J. Kahng, H. Shinohara, and Y. Kuk, Phys. Rev. Lett. **93**, 166403, (2004).

[86] J. Schlappa et al., Nature **485**, 82, (2012).

[87] P. A. Bares and G. Blatter, Phys. Rev. Lett. **64**, 2567, (1990).

[88] M. Ogata and H. Shiba, Phys. Rev. B **41**, 2326, (1990).

[89] K. Penc, F. Mila, and H. Shiba, Phys. Rev. Lett. **75**, 894, (1995).

[90] M. Arikawa, Y. Saiga, and Y. Kuramoto, Phys. Rev. Lett. **86**, 3096, (2001).

[91] E. A. Jagla, K. Hallberg, and C. A. Balseiro, Phys. Rev. B **47**, 5849, (1993).

[92] M. G. Zacher, E. Arrigoni, W. Hanke, and J. R. Schrieffer, Phys. Rev. B **57**, 6370, (1998).

[93] D. Senechal, D. Perez, and M. Pioro-Ladriere, Phys. Rev. Lett. **84**, 522, (2000).

[94] C. Kollath, U. Schollwöck, and W. Zwerger, Phys. Rev. Lett. **95**, 176401, (2005).

[95] C. Kollath and U. Schollwöck, New J. Phys. **8**, 220, (2006).

[96] H. Benthien and E. Jeckelmann, Phys. Rev. B **75**, 205128, (2007).

[97] P. Schmitteckert, in *High Performance computing in Science and Engineering 07*, edited by W. E. Nagel, W. Jäger, and M. Resch (Springer, Berlin, 2007).

[98] T. Ulbricht and P. Schmitteckert, EPL (Europhysics Letters) **86**, 57006, (2009); *ibid.* **89**, 47001, (2010).

[99] A. Moreno, A. Muramatsu, and J. M. P. Carmelo, Phys. Rev. B **87**, 075101, (2013).

[100] K. A. Al-Hassanieh, J. Rincón, E. Dagotto, and G. Alvarez, Phys. Rev. B **88**, 045107, (2013).

[101] K. Schönhammer and V. Meden, Phys. Rev. B **47**, 16205, (1993).

[102] J. Voit, Phys. Rev. B **47**, 6740, (1993).

[103] H. Benthien, F. Gebhard, and E. Jeckelmann, Phys. Rev. Lett. **92**, 256401, (2004).

[104] A. Abendschein and F. F. Assaad, Phys. Rev. B **73**, 165119, (2006).

[105] S. A. Söffing, I. Schneider, and S. Eggert, EPL (Europhysics Letters) **101**, 56006, (2013).

[106] R. Preuss, A. Muramatsu, W. von der Linden, P. Dieterich, F. F. Assaad, and W. Hanke, Phys. Rev. Lett. **73**, 732, (1994).

[107] J. Voit, J. Phys. Condens. Matter **8**, 779, (1996).

[108] F. H. L. Essler and A. M. Tsvelik, Phys. Rev. Lett. **88**, 096403 (2002); *ibid.* **90**, 126401, (2003).

[109] M. Fabrizio and A. O. Gogolin, Phys. Rev. B **51**, 17827, (1995);

[110] S. Eggert, H. Johannesson, and A. Mattsson, Phys. Rev. Lett. **76**, 1505, (1996).

[111] A. E. Mattsson, S. Eggert, and H. Johannesson, Phys. Rev. B **56**, 15615, (1997).

[112] V. Meden, W. Metzner, U. Schollwöck, O. Schneider, T. Stauber, and K. Schönhammer, Eur. Phys. J. B **16**, 631, (2000).

[113] S. Eggert, Phys. Rev. Lett. **84**, 4413, (2000).

[114] S. Andergassen, T. Enss, V. Meden, W. Metzner, U. Schollwöck, and K. Schönhammer, Phys. Rev. B **70**, 075102, (2004).

[115] P. Kakashvili, H. Johannesson, and S. Eggert, Phys. Rev. B **74**, 085114, (2006).

[116] I. Schneider, A. Struck, M. Bortz, and S. Eggert, Phys. Rev. Lett. **101**, 206401, (2008).

[117] W. Metzner, M. Salmhofer, C. Honerkamp, V. Meden, and K. Schönhammer, Rev. Mod. Phys. **84**, 299, (2012).

[118] A. Imambekov and L. I. Glazman, Science **323**, 228, (2009).

[119] A. Imambekov, T. L. Schmidt, and L. I. Glazman, Rev. Mod. Phys. **84**, 1253, (2012).

[120] L. Markhof and V. Meden, Phys. Rev. B **93**, 085108, (2016).

[121] J. Voit and H. J. Schulz, Phys. Rev. B **37**, 10068, (1988).

[122] V. Meden, K. Schönhammer, and O. Gunnarsson, Phys. Rev. B **50**, 11179, (1994).

[123] H. Matsueda, T. Tohyama, and S. Maekawa, Phys. Rev. B **74**, 241103, (2006).

[124] M. Hohenadler and F. F. Assaad, Phys. Rev. B **87**, 075149, (2013).

[125] M. Weber, F. F. Assaad, and M. Hohenadler, Phys. Rev. B **91**, 235150, (2015).

[126] D. Gruss, C.-C. Chien, M. Di Ventra, and M. Zwolak, arXiv:1610.01903.

[127] G. Bedürftig and H. Frahm, *Spectrum of boundary states in the open Hubbard chain*, Journal of Physics A: Mathematical and General, **30**, 12, (1997).

[128] D. Schuricht, F. H. L. Essler, A. Jaefari, and E. Fradkin, Phys. Rev. Lett. **101**, 086403, (2008).

[129] D. Schuricht, F. H. L. Essler, A. Jaefari, and E. Fradkin, Phys. Rev. B **83**, 035111, (2011).

[130] S. A. Kivelson, I. P. Bindloss, E. Fradkin, V. Oganesyan, J. M. Tranquada, A. Kapitulnik, and C. Howald, Rev. Mod. Phys. **75**, 1201, (2003).

[131] P. Schmitteckert, Phys. Rev. B **70**, 121302(R), (2004).

[132] F. H. L. Essler and R. M. Konik, in *From Fields to Strings: Circumnavigating Theoretical Physics (Ian Kogan Memorial Collection)*, edited by M. Shifman, A. Vainshtein, and J. Wheater (World Scientific, Singapore, 2005), Vol. I.

[133] J. Voit, Phys. Rev. B **45**, 4027, (1992).

[134] R. T. Clay, A. W. Sandvik, and D. K. Campbell, Phys. Rev. B **59**, 4665, (1999);

[135] E. Jeckelmann, Phys. Rev. Lett. **89**, 236401, (2002).

[136] A. W. Sandvik, P. Sengupta, and D. K. Campbell, Phys. Rev. Lett. **91**, 089701, (2003).

[137] A. W. Sandvik, L. Balents, and D. K. Campbell, Phys. Rev. Lett. **92**, 236401, (2004).

[138] S. Ejima and S. Nishimoto, Phys. Rev. Lett. **99**, 216403, (2007).

[139] A. Weiße, G. Wellein, A. Alvermann, and H. Fehske, Rev. Mod. Phys. **78**, 275, (2006).

[140] A. Holzner, A. Weichselbaum, I. P. McCulloch, U. Schollwöck, and J. von Delft, Phys. Rev. B **83**, 195115, (2011).

[141] J. Hackmann and F. B. Anders, Phys. Rev. B **89**, 045317, (2014).

[142] F. A. Wolf, I. P. McCulloch, O. Parcollet, and U. Schollwöck, Phys. Rev. B **90**, 115124, (2014).

[143] P. Schmitteckert, J. Phys.: Conf. Ser. **220**, 012022, (2010).

[144] A. Braun, P. Schmitteckert, *Numerical evaluation of Green's functions based on the Chebyshev expansion.* Phys. Rev. B., **90**, 165112, (2014).

[145] S. Ramasesha, J. Comp. Chem. **11**, 545, (1990).

[146] T. D. Kühner and S. R. White, Phys. Rev. B **60**, 335, (1999).

[147] D. Bohr, P. Schmitteckert, and P. Wölfle, EPL (Europhysics Letters) **73**, 246, (2006).

[148] S. Nishimoto and E. Jeckelmann, J.Phys.: Condens. Matter **16**, 613, (2004).

[149] D. Bohr and P. Schmitteckert, Phys. Rev. B **75**, 241103(R), (2007).

[150] S. Andergassen, T. Enss, V. Meden, W. Metzner, U. Schollwöck, and K. Schönhammer, Phys. Rev. B **73**, 045125, (2006).

[151] S. Ghoshal and A. B. Zamolodchikov, Int. J. Mod. Phys. A **9**, 3841, (1994); *ibid.* **9**, 4353(E), (1994).

[152] S. Skorik and H. Saleur, J. Phys. A: Math. Gen. **28**, 6605, (1995).

[153] P. Mattsson and P. Dorey, J. Phys. A: Math. Gen. **33**, 9065, (2000).

[154] R. Preuss, A. Muramatsu, W. Von der Linden, P. Dieterich, F. F. Assaad, and W. Hanke. *Spectral properties of the one-dimensional hubbard model.* Physical review letters, **73**, 732, (1994).

[155] L. Markhof and V. Meden. *Spectral function of the Tomonaga-Luttinger model revisited: Power laws and universality.* Physical Review B, **93**, 085108, (2016).

[156] Dirk Schuricht, Fabian H. L. Essler, Akbar Jaefari, and Eduardo Fradkin. *Local Density of States of One-Dimensional Mott Insulators and Charge-Density Wave States with a Boundary.* Physical Review Letters, **101**, 086403, (2008).

[157] S. A. Kivelson, I. P. Bindloss, E. Fradkin, V. Oganesyan, J. M. Tranquada, A. Ka-
pitulnik, and C. Howald. *How to detect fluctuating stripes in the high-temperature
superconductors.* Reviews of Modern Physics, **75**, 1201, (2003).

[158] Steven R. White and Adrian E. Feiguin. *Real-Time Evolution Using the Density
Matrix Renormalization Group.* Phys. Rev. Lett., **93**, 076401, (2004).

[159] Pasquale Calabrese and John Cardy. *Entanglement entropy and quantum field the-
ory.* J. Stat. Mech., **2004**, 06002, (2004).

[160] J. Eisert, M. Friesdorf, and C. Gogolin. *Quantum many-body systems out of equi-
librium.* Nat Phys, **11**, 124, (2015).

[161] Peter Barmettler, Matthias Punk, Vladimir Gritsev, Eugene Demler, and Ehud
Altman. *Quantum quenches in the anisotropic spin-1/2 Heisenberg chain: different
approaches to many-body dynamics far from equilibrium.* New J. Phys., **12**, 055017,
(2010).

[162] Corinna Kollath, Andreas M. Läuchli, and Ehud Altman. *Quench Dynamics
and Nonequilibrium Phase Diagram of the Bose-Hubbard Model.* Phys. Rev. Lett., **98**,
180601, (2007).

[163] Michael Moeckel and Stefan Kehrein. *Interaction Quench in the Hubbard Model.*
Phys. Rev. Lett., **100**, 175702, (2008).

[164] Lars Bonnes, Fabian H. L. Essler, and Andreas M. Läuchli. *"Light-cone" dynam-
ics after quantum quenches in spin chains.* Physical Review Letters, **113**, (2014).

[165] Maurizio Fagotti, Mario Collura, Fabian H. L. Essler, and Pasquale Calabrese.
Relaxation after quantum quenches in the spin- 1/2 Heisenberg XXZ chain. Physical
Review B, **89**, 125101, (2014).

[166] B. Pozsgay, M. Mestyán, M. A. Werner, M. Kormos, G. Zaránd, and G. Takács.
*Correlations after quantum quenches in the XXZ spin chain: Failure of the Generalized
Gibbs Ensemble.* Physical Review Letters, **113**, 117203, (2014).

[167] M. Mestyan, B. Pozsgay, G. Takacs, and M. A. Werner. *Quenching the XXZ spin
chain: quench action approach versus generalized Gibbs ensemble.* Journal of Statisti-
cal Mechanics: Theory and Experiment, P04001, (2015).

[168] Frank Pollmann, Masudul Haque, and Balázs Dóra. *Linear quantum quench in
the Heisenberg XXZ chain: Time-dependent Luttinger-model description of a lattice
system.* Phys. Rev. B, **87**, 041109, (2013).

[169] Piotr Chudzinski and Dirk Schuricht. *Time evolution during and after finite-time
quantum quenches in Luttinger liquids.* Phys. Rev. B, **94**, 075129, (2016).

[170] Mario Collura, Pasquale Calabrese, and Fabian H. L. Essler. *Quantum quench
within the gapless phase of the spin − 1 2 Heisenberg XXZ spin chain.* Phys. Rev. B,
92, 125131, (2015).

[171] S. Blanes, F. Casas, J. A. Oteo, and J. Ros. *The Magnus expansion and some of its applications.* Physics Reports, **470**, 151, (2009).

[172] Sergei Lukyanov. *Correlation amplitude for the XXZ spin chain in the disordered regime.* Phys. Rev. B, **59**, 11163, (1999).

[173] Pasquale Calabrese and John Cardy. *Time Dependence of Correlation Functions Following a Quantum Quench.* Phys. Rev. Lett., **96**, 136801, (2006).

[174] A. C. Hewson, *The Kondo Problem to Heavy Fermions* (Cambridge University Press, Cambridge, 1993).

[175] D. Bohr and P. Schmitteckert, *The dark side of benzene: Interference vs. interaction*, Ann. Phys. **524**, 199, (2012).

[176] P. Schmitteckert, *The dark side of DFT based transport calculations*, Phys. Chem. Chem. Phys. **15**, 15845, (2013).

[177] M. Walz, J. Wilhelm, and F. Evers, *Current patterns and orbital magnetism in mesoscopic dc transport*, Phys. Rev. Lett. **113**, 136602, (2014).

[178] A. J. Daley, C. Kollath, U. Schollwöck, and G. Vidal, *Time-dependent density-matrix renormalization-group using adaptive effective Hilbert spaces*, J. Stat. Mech., P04005, (2004).

[179] Peter Schmitteckert. *Nonequilibrium electron transport using the density matrix renormalization group method.* Phys. Rev. B, **70**, 121302, (2004).

[180] H. Schoeller, *A perturbative nonequilibrium renormalization group method for dissipative quantum mechanics*, Eur. Phys. J. Special Topics **168**, 179, (2009).

[181] R. B. Saptsov and M. R. Wegewijs, *Fermionic superoperators for zero-temperature nonlinear transport: Real-time perturbation theory and renormalization group for Anderson quantum dots*, Phys. Rev. B **86**, 235432, (2012).

[182] S. Bravyi, D. P. DiVincenzo, and D. Loss, *Schrieffer–Wolff transformation for quantum many-body systems*, Ann. Phys. **326**, 2793, (2011).

[183] D. Bohr and P. Schmitteckert, *Strong enhancement of transport by interaction on contact links*, Phys. Rev. B **75**, 241103, (2007).

[184] E. Boulat, H. Saleur, and P. Schmitteckert, *Twofold advance in the theoretical understanding of far-from-equilibrium properties of interacting nanostructures*, Phys. Rev. Lett. **101**, 140601, (2008).

[185] S. Kirino, T. Fujii, J. Zhao, and K. Ueda, *Time-dependent DMRG study on quantum dot under a finite bias voltage*, J. Phys. Soc. Jpn. **77**, 084704, (2008).

[186] L. G. G. V. Dias da Silva, F. Heidrich-Meisner, A. E. Feiguin, C. A. Büsser, G. B. Martins, E. V. Anda, and E. Dagotto, *Transport properties and Kondo correlations in nanostructures: Time-dependent DMRG method applied to quantum dots coupled to Wilson chains*, Phys. Rev. B **78**, 195317, (2008).

[187] F. Heidrich-Meisner, A. E. Feiguin, and E. Dagotto, *Real-time simulations of nonequilibrium transport in the single-impurity Anderson model*, Phys. Rev. B **79**, 235336, (2009).

[188] F. Schwarz, I. Weymann, J. von Delft, and A. Weichselbaum, *Nonequilibrium steady-state transport in quantum impurity models: A thermofield and quantum quench approach using matrix product states*, Phys. Rev. Lett. **121**, 137702, (2018).

[189] A. Branschädel, G. Schneider, and P. Schmitteckert, *Conductance of inhomogeneous systems: Real-time dynamics*, Ann. Phys. **522**, 657, (2010).

[190] See Appendix.

[191] A.-P. Jauho, N. S. Wingreen, and Y. Meir, *Time-dependent transport in mesoscopic systems: general formalism and applications*, Semicond. Sci. Technol. **9**, 926, (1994).

[192] R. Tuovinen, R. van Leeuwen, E. Perfetto, and G. Stefanucci, *Time-dependent Landauer–Büttiker formula for transient dynamics*, J. Phys. Conf. Ser. **427**, 012014, (2013).

[193] A. Rosch, J. Paaske, J. Kroha, and P. Wölfle, *Nonequilibrium transport through a Kondo dot in a magnetic field: Perturbation theory and poor man's scaling*, Phys. Rev. Lett. **90**, 076804, (2003).

[194] H. Schoeller and F. Reininghaus, *Real-time renormalization group in frequency space: A 2-loop analysis of the nonequilibrium Kondo model at finite magnetic field*, Phys. Rev. B **80**, 045117 (2009); *ibid.* **80**, 209901(E), (2009).

[195] G. Sedghi, V. M. García-Suárez, L. J. Esdaile, H. L. Anderson, C. J. Lambert, S. Martín, D. Bethell, S. J. Higgins, M. Elliott, N. Bennett, J. E. Macdonald, and R. J. Nichols, *Long-range electron tunnelling in oligo-porphyrin molecular wires*, Nat. Nanotechnol. **6**, 517, (2011).

[196] S. Schmaus, A. Bagrets, Y. Nahas, T. K. Yamada, A. Bork, M. Bowen, E. Beaurepaire, F. Evers, and W. Wulfhekel, *Giant magnetoresistance through a single molecule*, Nat. Nanotechnol. **6**, 185, (2011).

[197] A. Bagrets, S. Schmaus, A. Jaafar, D. Kramczynski, T. K. Yamada, M. Alouani, W. Wulfhekel, and F. Evers, *Single molecule magnetoresistance with combined antiferromagnetic and ferromagnetic electrodes*, Nano Lett. **12**, 5131, (2012).

[198] C. W. Marquardt, S. Grunder, A. Błaszczyk, S. Dehm, F. Hennrich, H. von Löhneysen, M. Mayor, and R. Krupke, *Electroluminescence from a single nanotube–molecule–nanotube junction*, Nat. Nanotechnol. **5**, 863, (2010).

[199] G. Reecht, F. Scheurer, V. Speisser, Y. J. Dappe, F. Mathevet, and G. Schull, *Electroluminescence of a polythiophene molecular wire suspended between a metallic surface and the tip of a scanning tunneling microscope*, Phys. Rev. Lett. **112**, 047403, (2014).

[200] U. Mukhopadhyay, J. P. Dehollain, C. Reichl, W. Wegscheider, and L. M. K. Vandersypen, *A* 2×2 *quantum dot array with controllable inter-dot tunnel couplings*, Appl. Phys. Lett. **112**, 183505, (2018).

Acknowledgments

There is a long list of people to whom I would like to express my gratitude for the success of this thesis project before concluding the actual thesis.

Thank you Dirk, for bringing me to this wonderful city and institute and for allowing me to continue the research of my master's project, such that over the past four years we could hatch it into a publication. Thank you for your confidence in me and for always being available to discuss both professional and private matters. I consider you not only a supervisor but also a friend.

I am furthermore very grateful to Henk, for agreeing to be my official promotor.

To Peter Schmitteckert I owe thanks for the extensive insights into computational physics that he shared with me and without which this PhD project would not have been possible.

Ferdinand, I would like to thank you for your infectious enthusiasm, that always motivated me to put in the extra hours to finish our project.

I am deeply grateful to my two long-term office mates Erik and Stefano, for their patience with both my idiosyncracies as well as my computers noise levels and for their companionship and extensive counsel. Thank you Erik also for doing the heavy lifting for the Dutch summary of this thesis.

Thank you Camilo, for distracting me with a round of squash, when I needed it.

A special thanks goes to the other members of our group Niklas, Tatjana, Tom, Axel, Jurriaan and Floris. It was a pleasure to work with you.

Rembert, Guido, Sander and Nick, I appreciate the entertaining conversations and sick comments during lunch.

I am also grateful to Sonja. You have provided that particular Ländle atmosphere away from home.

Thanks to Lars and Kilian, for the football discussions in the hallway as well as Raffaele, for the occasional card game.

I'd like to thank all my other colleagues for making the institute a really pleasant place to work at.

My free time in Utrecht was greatly enriched by the "Italian" community of Jorgos, Paolo, Alessia and Daniele through plenty of excessive dinners and movie nights of varying sophistication.

I am very grateful to all of my friends from back home, who have made the long trip to Utrecht to support me at my defense.

I would like to thank all of you, who came to visit me in the past four years, particularly Magnus and Mathias.

Thank you Pavel and Svenja, that I was always welcome in your home.

Thanks to all the "Greater nerds", especially Bram, Mathijs, Scott and Watse for including me into their group. I cherish all those memorable holiday dinners and look forward to many more of them.

I am intensely grateful to my paranimfs Pavel and Stefano for helping me through what has been the darkest hours of my life.

Finally, I want to thank my mother, father and brother. I am so deeply grateful for the endless love and support that you have given me.

About the Author

Benedikt Matthias Schönauer was born September 12th 1988 in Karlsruhe, Germany, to Ulrich and Andrea Schönauer. He grew up in the village of Eggenstein-Leopolds-hafen, which is also the site of the research campus of the Karlsruhe Institute of Technology (KIT). From 2000 to 2008, he attended Humboldt Gymnasium in Karlsruhe. After nine months of civil service and a semester in chemistry, he started studying physics at KIT in 2009. From there he received his B.Sc. and M.Sc. degrees in physics. Parallel to his studies, he did two extended student interships at the Institute for Synchrotron Radiation and the Institute for Nanotechnology on the research campus of KIT.

In 2015, he took up a position as a PhD researcher under the supervision of Dirk Schuricht at Utrecht University, studying the non-equilibrium dynamics of low-dimensional quantum systems. The thesis at hand is an account of this research.

In his spare time, Benedikt is passionate about dinghy sailing and has used his time in the Netherlands to finish his CWO3 sailing diploma.